

Coherent Population Trapping in Real and Artificial Atoms

by

Vincent Kwok Huei Wong

Submitted in Partial Fulfillment

of the

Requirements for the Degree

Doctor of Philosophy

Supervised by

Professor Robert W. Boyd

The Institute of Optics

The College

School of Engineering and Applied Sciences

University of Rochester

Rochester, New York

2004

To mom and dad, who always believe in me,
and to my wife Angel.

Curriculum Vitae

The author was born in Singapore in 1972. In 1989, he pursued a Diploma in Electronics Engineering at Ngee Ann Polytechnic, Singapore and graduated in 1992 specializing in robotics and artificial intelligence. After which he served his national service for two and a half years as a Platoon Commander in the Army of the Singapore Armed Forces. Upon completion of his service in 1995, he obtained a direct entry to the third year of the four-year Bachelor degree program at the University of Glasgow, United Kingdom. He then graduated with a First Class Honors B.Eng in Electronics Engineering with Optoelectronics degree in 1997 with several awards. After which he began his graduate studies at the Institute of Optics, United States of America. He has carried out his doctoral research in nonlinear and quantum optics, atomic and semiconductor physics, and spectroscopy under the supervision of Professor Robert W. Boyd.

Publications

- Ryan S. Bennink, Robert W. Boyd, C. R. Stroud, Jr., and Vincent Wong, “Enhanced self-action effects by electromagnetically induced transparency in the two-level atom,” *Phys. Rev. A*, **63**, 033804 (2001).
- Vincent Wong, Robert W. Boyd, C. R. Stroud, Jr., Ryan S. Bennink, David L. Aronstein, and Q-Han Park, “Absorptionless self-phase-modulation via dark-state electromagnetically induced transparency,” *Phys. Rev. A*, **65**, 013810 (2001).
- Ryan S. Bennink, Vincent Wong, Alberto M. Marino, David L. Aronstein, Robert W. Boyd, C.R. Stroud, Jr., Svetlana Lukishova, and Daniel J. Gauthier, “Honeycomb pattern formation by laser-beam filamentation in atomic sodium vapor,” *Phys. Rev. Letts.*, **88**, 11, 113901 (2002).
- Ryan S. Bennink, Vincent Wong, Alberto M. Marino, David L. Aronstein, Robert W. Boyd, C. R. Stroud, Jr., Svetlana Lukishova and Daniel J. Gauthier, “Honeycomb pattern formation by laser-beam filamentation in atomic sodium vapor,” *Optics & Photonics News*, 26 (2002).
- Vincent Wong, Robert W. Boyd, C. R. Stroud, Jr., Ryan S. Bennink, and A. Marino, “Thirteen pump-probe resonances of the sodium *D1* Line,” *Phys. Rev. A*, **68**, 012502 (2003).
- John E. Heebner, Vincent Wong, Aaron Schweinsberg, Robert W. Boyd, and Deborah J. Jackson, “Optical transmission characteristics of fiber ring resonators,” *IEEE J. Q. Elect.* **40**, 6, 726 (2004)
- Vincent Wong, Ryan S. Bennink, Alberto M. Marino, Robert W. Boyd, and C. R. Stroud, Jr., “Influence of coherent Raman scattering on coherent population trapping in atomic sodium vapor,” *Phys. Rev. A*, **70**, 053811 (2004).
- Vincent Wong, Aaron Schweinsberg, Robert W. Boyd, and G. W. Wicks, “Coherent population trapping in an Island well,” to be published (2004).
- Ryan S. Bennink, Vincent Wong, Alberto M. Marino, Robert W. Boyd, C. R. Stroud, Jr., “Frequency conversion of optical signals using coherently prepared media,” to be published (2004).

- F. A. Narducci, Robert W. Boyd, C. R. Stroud, Jr., Ryan S. Bennink, Vincent Wong, and Alberto M. Marino, "Measurement of ground state recovery times," to be published (2004).

Conference Presentations

- Vincent Wong, Robert W. Boyd, C. R. Stroud, Jr., Ryan S. Bennink, David L. Aronstein, and Q-Han Park, "Absorptionless Self-Phase-Modulation in a Dark-State Electromagnetically Induced Transparency," QELS Tech. Digest, 30 (2001).
- Vincent Wong, Robert W. Boyd, C. R. Stroud, Jr., Ryan S. Bennink, David L. Aronstein, and Q-Han Park, "Absorptionless Self-Phase-Modulation in a Dark-State Electromagnetically Induced Transparency (DS-EIT) System," 3rd Annual Cross Border Workshop on Laser Science (2001).
- Vincent Wong, Robert W. Boyd, C. R. Stroud, Jr., Ryan S. Bennink, and Alberto M. Marino, "Saturation Induced Extra Resonances (SIER) in Pump-Probe Spectroscopy," NLO Tech. Digest, 340 (2002).
- Vincent Wong, Robert W. Boyd, C. R. Stroud, Jr., Ryan S. Bennink, and Alberto M. Marino, "13 resonances of the Sodium *D1* Line," LS-XVIII Tech. Digest, 128 (2002).
- Vincent Wong, Aaron Schweinsberg, and Robert W. Boyd, "Coherent population trapping in an island quantum well," LS-XIX Tech. Digest, 99 (2003).

Acknowledgments

I would like to start right from the beginning when I first applied to the Institute. It was Prof. Carlos Stroud, Jr. who was the graduate admissions chair that gave me the opportunity to pursue my doctorate here. I would also like to thank Dr. Scott Walck who patiently taught me about quantum mechanics which I finally found a use for.

Conducting my research work with Prof. Robert Boyd is a very interesting experience. His optimistic attitude is always a good morale booster when the experiments are not going too well. Even with our huge research group and his other commitments, Prof. Boyd still managed to find time for each of us. His broad knowledge always amazes me and taught me to “think outside the box”.

On the other hand, Prof. Stroud who has been like a second advisor to me, has immense knowledge of his field and beyond. I would like to thank him again for helping me verify even the slightest details of my work.

I also had a great deal of assistance from my colleagues Dr. Ryan Bennink and Alberto Marino who are themselves very intelligent and resourceful. The experiments would not have progressed as quickly without the help and guidance from Dr. Frank Narducci and Dr. Dan Gauthier whom I have learnt a great deal from. When I made the transition from atomic physics to solid state physics, Prof. Gary Wicks has been a great source of knowledge and I would not have done it without him. I would also like to acknowledge the administrative assistance provide by Joan Christian, Noelene Votens, Gayle Thompson, Betsy Benedict and Gina Kern.

I cannot say enough of my “trusty” dye laser which kept me here for an extra year or two but yet managed to squeeze out a few experiments for my thesis.

I would also like to mention my Tae Kwon Do instructor, Master Raymond Mondschein, who has been like a father-figure to me and has provide much needed support throughout my years here. Last but not least, I would also like to thank my parents, aunt Fong, and my wife Angel for all of their encouragements, patience, and for bearing with me all these years.

Abstract

In this thesis, coherent population trapping (CPT) is studied in two real-world systems: atomic sodium vapor and a quantum well structure. A series of spectroscopic studies were carried out in the atomic system to understand how CPT behaves in a non-idealized environment. In addition, a feasibility study is carried out to seek a solid state environment to facilitate the design of practical devices based on the process of CPT.

The first system used to study CPT is sodium vapor (the “real atom”). Even though sodium is a multi-level system, the spectral features and the parameters that govern them are found to be similar to those of the idealized three-level Λ system. For example, in both the idealized model and the actual atomic system, the ground state decoherence rate determines the width of the resonance as is demonstrated experimentally. The inclusion of Doppler broadening and propagation effects, and the impurities in the vapor, are found to weaken the strength of the CPT resonance. The presence of additional levels, which can either be virtual or real, permits additional concurrent processes to occur that enrich the spectrum. These concurrent processes are coherent Raman scattering, other wave mixing processes, crossover resonances, and optical pumping. Coherent Raman scattering can even invert the induced transparency feature of CPT into an induced absorption feature.

In spite of these complications, CPT has great potential for technologically advanced applications, with the example of frequency conversion being demonstrated here. As a medium for these applications, semiconductor systems are more practical than atomic sodium.

The second system studied is a quantum well structure (the “artificial atom”), designed to mimic a Λ configuration suited for observing CPT. Novel use of various aspects of band engineering and structure design is utilized to achieve such a configuration. An AlAsSb/InGaAs/AlGaAsSb ternary-quaternary alloy system is used to create an *Island* well structure. By employing intersubband

transitions only within the conduction band, a single carrier-type system is achieved. It is predicted that CPT can still be observed even with the added complexity of this semiconductor system.

Table of Contents

Curriculum Vitae	iii
Acknowledgments	vi
Abstract	viii
List of Tables	xiv
List of Figures	xv
List of Symbols and Acronyms	xx
1 Introduction	xxii
2 Quantum Interference Effects	5
2.1 Introduction	5
2.2 Autler Townes Splitting	5
2.3 Electromagnetically Induced Transparency	7
2.4 Coherent Population Trapping	8
2.5 A Comparison	9
2.6 Summary	15

3	The Atomic System	16
3.1	Introduction	17
3.2	Atomic Energy Level Structure	17
3.3	Atomic Sodium	21
3.4	Inhomogeneous Broadening	24
3.5	Summary	26
4	Laser Spectroscopy and Optical Coherence Effects	27
4.1	Introduction	27
4.2	Optical Pumping	27
4.3	Wave Mixing	32
4.4	Other Multi-Photon Effects	36
4.5	Summary	46
5	CPT in a Real Atom	47
5.1	Introduction	47
5.2	Experimental Layout	47
5.3	Thirteen Resonances of the Sodium <i>D1</i> Line	54
5.4	Influence of Coherent Raman Scattering on CPT	65
5.5	Transfer of Modulation via CPT	74
5.6	Measurement of the Ground State Decoherence Rate	77
5.7	Summary	80
6	The Semiconductor Band Structure	82
6.1	Introduction	83
6.2	Crystal Structure	83
6.3	Heterostructure	92

6.4	1D Quantum Well	93
6.5	Intersubband Transition	94
6.6	System Dynamics	96
6.7	Summary	102
7	CPT in an Artificial Atom	103
7.1	Introduction	103
7.2	Quantum Well Structures	104
7.3	Multi-Element Alloys	106
7.4	Numerical Results of CPT in a Quantum Well System	112
7.5	Summary	115
8	Conclusion	117
	Bibliography	121
A	General Density Matrix Equations of Motion	132
B	Floquet Expansion	135
C	Continued Fraction	139
D	Explicit Form of the Density Matrix EOM's	141
D.1	Dark State - Electromagnetically Induced Transparency	141
D.2	Thirteen Resonances of the Sodium <i>D1</i> Line / Modulation Transfer using CPT	142
D.3	Influence of Coherent Raman Scattering on CPT	143
D.4	CPT in a Quantum Well System	144
E	Matlab Code for the Numerical Simulations	145

F FEMLAB Code for the Quantum Well Simulation

150

G Physical Constants

154

List of Tables

3.1	Clebsch-Gordon coefficients for the <i>D1</i> line of sodium.	24
7.1	Band parameters at 300 K for the binary compounds.	108
7.2	Band parameters at 300 K for the ternary alloys.	109
7.3	Parameters used in the simulation of the <i>Island</i> well.	115
G.1	Table of physical constants.	155
G.2	Table of constants for the <i>D1</i> line of atomic sodium.	155

List of Figures

2.1	Autler Townes splitting.	6
2.2	Comparison of the absorption within the EIT window (solid line) and the absorption due to the sum of two lorentzian tails (dashed line).	7
2.3	Destructive interference of the transition probability amplitudes that leads to EIT.	8
2.4	Energy level diagrams of the three standard configurations of a three-level atomic system: (a) Ξ system, (b) V system, and (c) Λ system.	9
2.5	Real and imaginary parts of the density matrix element (for the probe field), of the three-level systems, for various normalized pump Rabi frequencies $\Omega_p T_1$	14
3.1	Atomic structure of sodium showing a single valence electron.	21
3.2	Energy level structure of the two D lines of atomic sodium.	23
3.3	Energy shifts of the Zeeman levels in the presence of a weak magnetic field.	24
4.1	(a) Probe absorption spectrum showing a spectral hole. (b) Pump absorption spectrum with and without saturation.	28
4.2	(a) Optical pumping in a Λ system depicting depletion of population in the lower ground level. (b) Absorption of the probe field in the presence of a weakly and strongly saturating pump field.	30
4.3	Difference-frequency crossing resonance in a V system. (a) Energy level diagram showing the V system. (b) Resulting absorption dip for a red-detuned probe field.	30

4.4	Cross-transition resonance in a double- Λ system. (a) Energy level diagram showing optical pumping from ground level $ a\rangle$ to ground level $ b\rangle$ through spontaneous emission. (b) Enhanced absorption for a red-detuned probe field.	31
4.5	(a) Vectorial representation of phase matching in wave mixing processes. (b) Phase mismatch due to difference in the refractive indices.	32
4.6	Two possible four-wave-mixing configurations.	33
4.7	Forward degenerate four-wave-mixing in an open two-level system.	34
4.8	Non-degenerate four-wave-mixing in the V system.	34
4.9	The two coherent Raman scattering processes: (a) Coherent anti-Stokes Raman scattering, and (b) coherent Stokes Raman scattering.	35
4.10	Diffraction, soliton formation and self focusing.	36
4.11	(a) Filamentation and (b) structured breakup of the beam due to SPM.	37
4.12	(a) Coherent, (b) amplitude squeezed, and (c) phase squeezed light. The phase-space representations are shown in the lower half.	37
4.13	The pulse envelope travels at the group velocity.	38
4.14	(a) Linear $\chi^{(1)}$ and nonlinear $\chi^{(3)}$ responses of a radiatively-broadened, bichromatic two-level system as a function of the normalized pump-probe detuning ζT_1 . (b) Expanded view around the detuning where there is no absorption of the probe field and the SPM coefficient is large.	39
4.15	Energy level structure of the DS-EIT system.	40
4.16	Degenerate atom-field states of the Λ system, with absorption of the ω_1 photon and emission of the ω_2 photon. The location of the sphere denotes which atomic energy level the electron is occupying.	42
4.17	Linear and nonlinear susceptibilities of the homogeneously broadened DS-EIT system.	45
4.18	Large SPM in the absence of linear and nonlinear absorption of the Doppler-broadened DS-EIT system.	45
5.1	Absorption spectrum of Rhodamine 590 dye.	48

5.2	Technical drawing of the experimental layout. The components are color-coded to avoid cluttering with extra labels.	49
5.3	(a) Central flange and (b) cold finger of the vapor cell.	50
5.4	Sodium vapor cell used in the experiment. (i) Schematic drawing of the cell. * - Thermocouple wires are placed at these locations to measure the temperature. (ii) Fluorescence inside the cell.	50
5.5	Conversion chart for Type E thermocouple wires at ice-point.	51
5.6	Vapor pressure versus temperature.	52
5.7	The vacuum pumping station.	53
5.8	Schematic layout of the thirteen resonances experiment.	54
5.9	Probe transmission versus pump-probe detuning for various pump intensities. The types of resonances are labelled on the top and the subsystems where the resonances occur in are shown on the right.	55
5.10	Probe transmission versus pump/probe detuning for various pump detunings with a (a) weakly saturating and (b) strongly saturating pump field. The arrow designates the pump frequency in each case.	57
5.11	Energy level diagram of the four-level model.	58
5.12	Resonances associated with the two-level and three-level V subsystems for the case of comparable pump and probe intensities.	59
5.13	Resonances associated with the Λ and double- Λ subsystems for the case of comparable pump and probe intensities.	62
5.14	Energy level diagrams of the four cross-transition resonances.	63
5.15	(a) Λ system between Zeeman sublevels. (b) Optical pumping to extreme Zeeman sublevels.	63
5.16	(a) On- and (b) off-Raman resonance coupling of the pump and probe fields.	64
5.17	Schematic layout of the experiment to study the effect of coherent Raman scattering on CPT.	65

5.18	(a) Dual-scan experimental transmission spectrum of each polarization component. Inset: Timing diagram of the detuning scans. (b) Energy level diagram depicting CARS (Region I). (c) Energy level diagrams showing CARS on the left and CSRS on the right which occur simultaneously (Region II). (d) The beat signals are of the horizontally polarized fields (Region I) when the two pump fields are on ($\delta = 0$) and off ($\delta \neq 0$) the Raman resonance. (e) The beat signal of the horizontally (vertically)-polarized fields shows the presence of the CARS (CSRS) idler field (Region II).	67
5.19	Energy level diagram of the six-wave three-level Λ system.	70
5.20	Theoretical spectra of the intensities of the two polarization components as a function of the Raman detuning δ for the three different regions of pump field detuning.	72
5.21	Theoretical spectra of the magnitude of the ground state coherence $ \sigma_{ba} $, after propagation, for the 3 regions studied. The dash curve is with only CPT present while the solid curve includes both CARS and CSRS processes as well.	73
5.22	Beat signal spectrum of pump 2 and the idler with the local oscillator. The local oscillator is tuned near the frequency of pump 1. The triangular wave AM signal (sinc^2 envelop spectrum) imposed on pump 2 is transferred to the idler signal.	75
5.23	The modulated-pump scheme with modulation imposed only on ω_2	76
5.24	Energy level diagram depicting the method to measure the ground states relaxation rates.	78
5.25	Experimental layout to measure the ground state relaxation rate of sodium.	78
5.26	Intensity transmission trace of relaxation measurement.	79
5.27	Ground states population (γ) and coherence (Γ) relaxation rates as a function of helium buffer gas pressure using two sets of pressure gauges.	80
6.1	(a) Discrete energy levels forming bands in a semiconductor system. (b) A planar view of covalent bonds of semiconductors.	84
6.2	A donor atom with a free electron in the crystal lattice.	84
6.3	Energy-wavevector diagram showing interband and intersubband transitions.	91
6.4	Energy level diagram of a heterojunction.	92

6.5	Subbands within the conduction band of a 1D quantum well.	93
6.6	Two approaches to increase the interaction length of a quantum well medium: (a) Multiple quantum well structure, (b) single/multiple well(s) in a cavity.	95
6.7	Intrasubband electron-phonon scattering.	100
7.1	(a) The single well, (b) the staggered well, (c) resonantly, and (d) non-resonantly tunnelled coupled-double well.	105
7.2	<i>Island</i> well structure to create a Λ system.	106
7.3	Lattice constant versus composition for the three ternaries that are lattice matched to InP.	111
7.4	Lattice constant versus composition, calculated from the various methods.	111
7.5	Direct and indirect bandgap energies of the quaternary calculated using Method 3.	112
7.6	Probe absorption versus pump-probe detuning for various pump field intensities.	115
E.1	Screenshot of the LP version of the Matlab code.	145
E.2	Flow chart of the Matlab code for the CRS-CPT experiment.	147
E.3	Screenshot of the MS version of the Matlab code.	149
F.1	Flow chart of the FEMLAB code for the CPT in quantum well simulation.	153

List of Symbols and Acronyms

AM	Amplitude modulation, page 48.
AOM	Acousto-optic modulator, page 48.
Ξ	Cascade system: Two absorptive transitions, page 7.
CARS	Coherent anti-Stokes Raman scattering, page 35.
CBM	Conduction band minimum, page 88.
CBO	Conduction band offset, page 92.
CPT	Coherent population trapping, page 1.
CRS	Coherent Raman scattering, page 33.
CSRS	Coherent Stokes Raman scattering, page 35.
CW	Continuous-wave, page 11.
Δ	Field detuning , see equation (2.3), page 6.
δ	Two photon detuning , see equation (2.9), page 10.
DFC	Difference frequency crossing, page 29.
E_F	Fermi energy, page 88.
EIT	Electromagnetically induced transparency, page 1.
FDFWM	Forward degenerate four-wave-mixing, page 33.

FWHM	Full width at half maximum, page 56.
Γ	Dephasing rate, page 5.
γ	Population decay rate, page 10.
IBT	Interband transition, page 90.
ISBT	Intersubband transition, page 3.
k_F	Fermi wavevector, page 88.
Λ	Lambda system: One absorptive and one emissive transition with a common upper level, page 8.
LO	Longitudinal-optical (phonon), page 99.
μ_{ij}	Dipole matrix element, page 6.
NDFWM	Nondegenerate four-wave-mixing, page 34.
Ω	Rabi frequency , see equation (2.2), page 6.
SPM	Self phase modulation, page 36.
T_1	Radiative lifetime, page 13.
T	Temperature in degree Kelvin, page 25.
V	V system: One emissive and one absorptive transition with a common lower level, page 8.
VBM	Valence band minimum, page 88.
VBO	Valence band offset, page 92.
ω	Angular frequency, page 5.
w.r.t.	With respect to, page 10.
ζ	Pump-probe detuning , see equation (2.8), page 10.

1 Introduction

Quantum mechanics has brought scientist to a new level of knowledge about the environment around us. The contributors to quantum mechanics includes Max Planck [1], Neils Bohr [2], Albert Einstein [3], and Paul Dirac [4], among others. Many unexplained observations in the early twentieth century were described by quantum mechanics. As scientists got a better grasp of their environment, many more quantum mechanical phenomena were observed and studied. Quantum interference is one class of such diverse phenomena.

Quantum interference encompasses many processes in a variety of environments. In particular, there are two related processes that will be studied in detail. These are electromagnetically induced transparency (EIT) and coherent population trapping (CPT) . These interference effects are related to the Fano interference [5] which requires coupling to a continuum. EIT and CPT are quantum interference techniques used to eliminate absorption in an otherwise opaque medium. Alzetta et. al. [6] observed them in a Lambda (Λ) system in 1976 first and Stroud's group [7] in 1978 with the latter introducing the term coherent population trapping. Although these quantum interference effects were also proposed and observed in various configurations, it is only in 1990 that the term EIT was introduced by Harris [8]. Arimondo [9] and Marangos [10] have each written an excellent review article on the subject. Another related process is lasing without inversion [11–15]. It utilizes the quantum coherence and interference effect to eliminate absorption, thus lowering the threshold for lasing. Atomic systems were naturally used for studies of these processes since they have the ability to provide a discrete level structure.

These interference effects create a very narrow (subnatural linewidth) transparency window.

According to the Kramer-Kronig relation, the (real part of the) refractive index rapidly changes with a positive slope. This results in the material system having a larger than normal group index (of refraction) n_g . For EIT, the destructive interference of the linear absorption is accompanied by a constructive interference of the nonlinear susceptibility. On the other hand, CPT will eliminate all nonlinear response (of the two applied fields). Both these processes can still be used to enhance other nonlinear processes.

The lack of absorption is useful for enhancing a variety of wave-mixing processes [8, 16, 17], and refractive index [18] or self phase modulation enhancement processes [19, 20]. The large group velocity is used to slow a pulse of light down to 19 m/s [21]. The narrow resonance can be used as a frequency reference for lasers [22] and in atomic clocks [23–26].

In the later part of the twentieth century, as technology advanced and components shrunk in size to that of an atom, quantum mechanics was used to predict the behaviors of such devices. An example is a quantum well where the energy band becomes quantized into subbands. Technological advances also permit researchers to built quantum dots where the wavefunction of the electron is confined in all three spatial dimensions and the energy band is completely quantized into discrete levels.

The study of semiconductor materials dates back to the early twentieth century. Since the 1960s, germanium was replaced by silicon as the semiconductor material and semiconductor technologies have been improving since, e.g. from two-terminal devices, to transistors, to semiconductor lasers and advanced computer chips. One sub-category of semiconductor physics, the quantum well, evolved naturally from early simple devices, by first utilizing interband and then using intersubband transitions. Intraband optical transitions were first observed by Kamgar [27] in 1974 in a 2D electron gas formed in Si inversion layers. The first direct observation of infrared intersubband transitions in the conduction band was performed by West [28]. Quantum well structures have been used as optical sensors such as the QWIP [29], and as light emitters such as the quantum well laser [30, 31], and quantum light sources [32].

To achieve transitions at optical frequencies, band engineering is required. This is achieved through the use of various III-V and II-VI compounds, and even exotic quaternary alloys (in place of the Group IV silicon). On the patterning side, the use of band engineering, which is one of the greatest strength of semiconductor physics, has been limited to tuning the transition wavelength by

varying the width of the quantum well. Multi-structured or multiple well systems provide even more flexibilities, but at the cost of increased complexity. As the dimensions of quantum well systems approaches those of an atom, the energy level structure of the quantum well begin to resemble that of an atomic system. Intersubband transitions (ISBT) in the conduction band of a quantum well system can be used to mimic optical transitions in an atomic system. Coupled with the ability to pattern almost any physical structure, a “designer” atom can be made.

In the past decade, various quantum interference effects have been observed in semiconductor structures. Fröhlich and coworkers have observed coherent effects such as the optical Stark effect [33] in bulk semiconductor system. EIT and CPT have been observed in interband systems [34–37]. Some of these experiments involve exciton-photon interactions. Faist et. al. [38] have observed Fano interference utilizing intersubband transitions in the conduction band. LWI [39], and EIT in a cascade system [40, 41] utilizing intersubband transitions have also been observed.

EIT and CPT have been well studied in various atomic systems. However, most researches concentrate only on the transparency feature, and not much focus has been given to the effects that concurrent processes (which occur) have on the quantum interference. Although CPT has been observed in a single-carrier system, the structure used [42] is far from ideal for obtaining a large and narrow resonance. The goal of this thesis is to better understand CPT in a “real” atomic system and explore the potential of exporting the effect to a solid state environment to enable the construction of practical devices based on CPT. The manuscript is structured as follows:

- Chapter 2 describes the two related quantum interference effects of CPT and EIT, with a brief comparison.
- Chapter 3 outlines the basics of an atomic system from the energy level structure to the macroscopic properties in the context of atomic sodium (which was used for all the experiments).
- Chapter 4 gives a brief introduction to various optical pumping, wave mixing and multi-photon effects that were observed and studied.
- Chapter 5 details the spectroscopic studies of sodium and CPT.
- Chapter 6 follows from Chapter 3 into semiconductor systems and describes the concept of a quantum well.

- Chapter 7 describes the feasibility study of observing CPT in a quantum well system, from the design of the quaternary alloy to the *Island* well structure.
- The last chapter summarizes the research work and discusses some future work that can be done.
- The large sets of density matrix equations of motion are given in the appendices. Flow charts that outline the numerical code (but not the code) are also given in the appendices.

2 Quantum Interference Effects

2.1 Introduction

The Autler Townes splitting [43], a coherence effect, was first observed in 1955. This is the alternating current (AC) version of the DC (direct current) Stark shift. Electromagnetically induced transparency or EIT shares the same quantum mechanical properties of the Autler Townes splitting, in addition to including quantum interference. EIT is a pump-probe effect that eliminates the absorption of a medium by using quantum interference. This creates a narrow transparency window while preserving the large nonlinearity associated with a near- resonance effect. In a Λ system, a related process called coherent population trapping or CPT can completely eliminate all atomic responses. Comparisons between CPT and EIT, and between EIT in the various three-level systems are presented in this chapter.

2.2 Autler Townes Splitting

The Autler Townes splitting is an interesting coherence effect. When a strong, saturating electromagnetic field (of frequency ω) is applied to a transition, the initial and final levels are each split into doublets as shown in Fig. 2.1. The threshold for the splitting (saturation) is equal to the dephasing rate (Γ) of the transition. The splitting is proportional to the field strength and detuning of the field from the transition:

$$\Omega_{\text{eff}} = \sqrt{\Omega^2 + \Delta^2}, \quad (2.1)$$

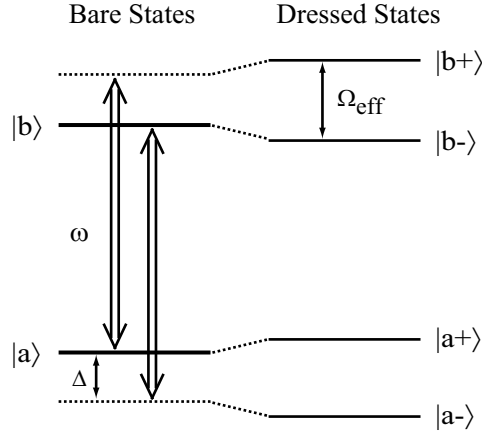


Figure 2.1: Autler Townes splitting.

where the Rabi frequency (interaction energy in frequency units) of the applied field is

$$\Omega = 2\mu_{ba}E/\hbar, \quad (2.2)$$

and the detuning of the applied field from the atomic resonance is given by

$$\Delta = \omega - \omega_{ba}. \quad (2.3)$$

Ω_{eff} is called the effective Rabi frequency and represents the amount of splitting in angular frequency. $\mu_{ba} = -er_{ba}$ is the dipole matrix element of the transition from level $|a\rangle$ to level $|b\rangle$, e is the electron charge (see Appendix G for values of physical constants), r_{ba} is the position matrix element, E is the electric field amplitude, \hbar is the reduced Planck's constant ($\hbar = h/2\pi$), ω is the angular frequency of the applied field, and ω_{ba} is the angular frequency of the transition. Such doublets are often called dressed states, which gives a more intuitive understanding with the following change of basis states:

$$|b+\rangle = |b\rangle + \Delta/2 + \Omega_{\text{eff}}/2, \quad (2.4)$$

$$|b-\rangle = |b\rangle + \Delta/2 - \Omega_{\text{eff}}/2, \quad (2.5)$$

where $|b\rangle$ is the bare state and $|b\pm\rangle$ are the dressed states. This splitting is also often called the AC Stark shift c.f. to the DC Stark shift that occurs when a DC field is applied.

This splitting is observed by probing with a weaker field. If the probe field is applied to the same transition, the absorption of the probe field shows interesting features. The Mollow absorption

spectrum [44] given by the $\text{Im } \chi^{(1)}$ curve in Fig. 4.14(a) has an absorption peak on the red side of resonance (lower frequency than the bare states' transition frequency) at $-\Omega_{\text{eff}}$, a dispersive profile on resonance, and a gain feature on the blue side of resonance at Ω_{eff} , for a blue detuned pump field. When the pump field is off resonance as shown, the absorption and gain features will have asymmetric heights due to the unbalanced population in each of the dressed states. When the probe field is applied from a third level to one of the doublets (either the upper or lower doublets), two lorentzian absorption peaks, separated by the effective Rabi frequency, are observed.

2.3 Electromagnetically Induced Transparency

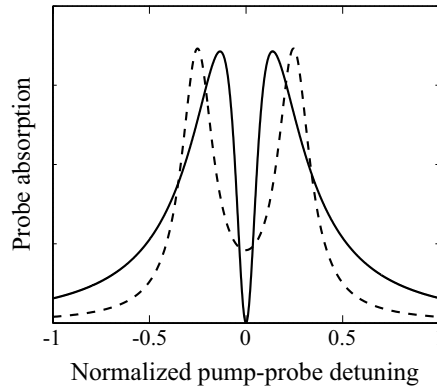


Figure 2.2: Comparison of the absorption within the EIT window (solid line) and the absorption due to the sum of two lorentzian tails (dashed line).

To illustrate the difference between the Autler Townes splitting and EIT, a weakly saturating pump field is used, i.e. $\Omega_{\text{eff}} \lesssim \Gamma$. In this example, the doublet states are not well separated. When the weaker probe field is applied from a third level to one of the doublet states, two lorentzian absorption peaks will be observed. When the probe field is tuned to the mid-point of the doublet (two-photon resonance condition), naively, the absorption of the probe field should be the sum of the two lorentzian tails (see Fig. 2.2). It is however observed experimentally that the absorption is less and can potentially be zero. This is due to quantum interference and the process is called electromagnetically induced transparency (EIT) [8, 10, 45].

The quantum interference effect of EIT is best illustrated by taking the case of the probe field coupling only the lower doublets, of the example given before, to a ground level, i.e. a cascade Ξ

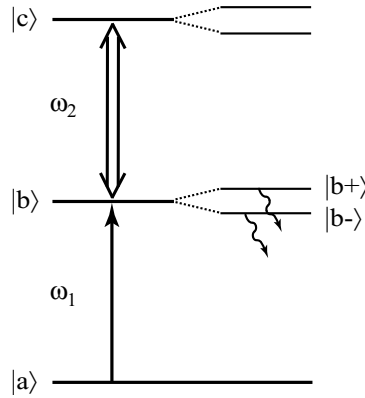


Figure 2.3: Destructive interference of the transition probability amplitudes that leads to EIT.

system as shown in Fig. 2.4(a). The transition probability amplitude from each level of that doublet $|b_{\pm}\rangle$ to the common third level $|a\rangle$ can interfere destructively as shown in Fig. 2.3. This leads to a cancellation of the absorption of the probe field. Since the $|b\rangle$ states are not populated, there is also no absorption of the pump field. The nonlinear susceptibility experiences a constructive interference instead. This opposite interference effect for the linear and nonlinear susceptibility enables EIT to be used to enhance the various nonlinear effects mentioned in Chapter 1. EIT can also be observed in a V system [Fig. 2.4(b)] where the lower doublet is the ground level. More common use of this configuration is for a related process called lasing without inversion (LWI).

2.4 Coherent Population Trapping

A unique feature of a three-level Λ system [Fig. 2.4(c)] is that a dark state [9] can be created through coherent population trapping (CPT). Once the system is “pumped” into the dark state, there is no absorption for either the pump or the probe field. The two applied fields create two coherent superpositions states from the lower atomic basis states which can be defined as

$$|DS\rangle = \frac{\Omega_1}{\Omega'}|a\rangle - \frac{\Omega_2}{\Omega'}|b\rangle, \quad (2.6)$$

$$|BS\rangle = \frac{\Omega_1}{\Omega'}|a\rangle + \frac{\Omega_2}{\Omega'}|b\rangle, \quad (2.7)$$

where $\Omega' = \sqrt{\Omega_1^2 + \Omega_2^2}$ is the generalized Rabi frequency, and Ω_1 (Ω_2) is the Rabi frequency of the probe (pump) field. Both the dark state (DS) and the corresponding bright state (BS) are state

amplitudes with their corresponding dressed states in the dressed system [46]. At exact two-photon (Raman) resonance, all susceptibilities vanish and the system is decoupled from the optical fields. A perfect dark state is created if there is no dephasing between the initial and final states of the two-photon transition. The linewidth of the CPT transparency feature is dependent on the dephasing rate between the two ground states, and not of that of the radiative transitions (as in the other two three-level systems) which can be much larger.

The transparency can also be explained with destructive interference as is done with EIT. In the Λ system, the interference occurs between the two pathways to the common excited level. However, unlike the EIT case, destructive interference is also present for the nonlinear susceptibility.

2.5 A Comparison

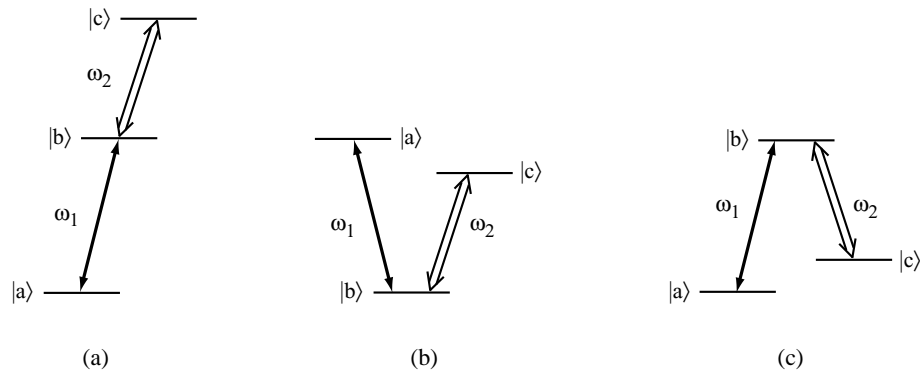


Figure 2.4: Energy level diagrams of the three standard configurations of a three-level atomic system: (a) Ξ system, (b) V system, and (c) Λ system.

CPT is closely related to EIT. Although these two processes produce similar effects, they have important distinctions. CPT can be considered as a specific case of EIT, where the dark state associated with CPT is only stable in a Λ system, and it has the consequence of eliminating all the responses of the medium at a specific frequency for the preparation fields¹. EIT involves a strong pump and a weaker probe field while CPT is usually performed with comparable field strengths. If the system is not initially prepared, in the transient regime, EIT can be partially switched on in less

¹The two applied fields that created the dark state.

then a radiative lifetime. CPT requires a few radiative lifetimes for the atom to be optically pumped into a dark state [47].

To observe the difference, the three closed three-level systems with two applied fields as shown in Fig. 2.4 are studied in the homogeneously broadened limit. The pump field is applied to the $|b\rangle \rightarrow |c\rangle$ transition and the much weaker probe field to the $|a\rangle \rightarrow |b\rangle$ transition. The derivations of the susceptibilities are identical for the Λ and the Ξ system with the appropriate change of decay and detuning terms. The V system is a little more complicated as some of the approximations are not applicable.

For the Λ system, the detunings of the probe and pump fields w.r.t. their respective transition frequencies are $\Delta_1 = \omega_1 - \omega_{ba}$ and $\Delta_2 = \omega_2 - \omega_{bc}$ respectively. The pump-probe detuning is defined as

$$\zeta = \omega_1 - \omega_2. \quad (2.8)$$

and the two-photon detuning as

$$\delta = \Delta_1 - \Delta_2. \quad (2.9)$$

The Raman (two-photon) resonance in a Λ system is defined as $\zeta = \omega_{ca}$ ($\delta = 0$).

The Rabi frequency is as defined in Eq. 2.2. γ_{ab} and γ_{cb} are the radiative population decay rates from level $|b\rangle$ to the lower levels $|a\rangle$ and $|c\rangle$ respectively. γ_{ac} and γ_{ca} are the decay rates from levels $|c\rangle$ to $|a\rangle$ and $|a\rangle$ to $|c\rangle$ due to transit-time effects, which are much smaller than the radiative decay rates. The coherence dephasing rates (off-diagonal density matrix elements) as defined by Eq. A.3 are

$$\Gamma_{ac} = \frac{1}{2} (\gamma_{ca} + \gamma_{ac}), \quad (2.10a)$$

$$\Gamma_{ab} = \frac{1}{2} (\gamma_{ab} + \gamma_{cb} + \gamma_{ca}), \quad (2.10b)$$

$$\Gamma_{cb} = \frac{1}{2} (\gamma_{ab} + \gamma_{cb} + \gamma_{ac}). \quad (2.10c)$$

The general density matrix equations of motion are written in Appendix A. A rotating frame transformation as described in the appendix is performed where

$$\rho_{ba} = \sigma_{ba} e^{-i\omega_1 t}, \quad (2.11a)$$

$$\rho_{bc} = \sigma_{bc} e^{-i\omega_2 t}, \quad (2.11b)$$

$$\rho_{ca} = \sigma_{ca} e^{-i(\omega_1 - \omega_2)t}. \quad (2.11c)$$

The rotating-wave approximation and the population conservation rule for closed atomic systems are then applied. To simplify the problem, it is assumed that initially all the population are in the lowest state $|a\rangle$ such that

$$\sigma_{aa}(t=0) = 1, \quad \sigma_{bb}(t=0) = \sigma_{cc}(t=0) = 0, \quad (2.12)$$

$$\sigma_{cb}(t=0) = 0. \quad (2.13)$$

The off-diagonal equations of motion then become a pair of coupled equations

$$\dot{\sigma}_{ba} = (i\Delta_1 - \Gamma_{ba}) \sigma_{ba} + \frac{i}{2}\Omega_2\sigma_{ca} + \frac{i}{2}\Omega_1, \quad (2.14)$$

$$\dot{\sigma}_{ca} = (i\delta - \Gamma_{ca}) \sigma_{ca} + \frac{i}{2}\Omega_2^*\sigma_{ba}. \quad (2.15)$$

Since the dipole matrix elements of the Rabi frequencies are real, the conjugate notation is dropped from here on. These equations can be written compactly in matrix form (Eq. A.7) with

$$R = \begin{bmatrix} \sigma_{ba} \\ \sigma_{ca} \end{bmatrix}, \quad M = \begin{bmatrix} i\Delta_1 - \Gamma_{ba} & \frac{i}{2}\Omega_2 \\ \frac{i}{2}\Omega_2 & i\delta - \Gamma_{ca} \end{bmatrix}, \quad S = \begin{bmatrix} -\frac{i}{2}\Omega_1 \\ 0 \end{bmatrix}. \quad (2.16)$$

With continuous wave (CW) fields, the density matrix equations of motion can be solved with an integration or a matrix inversion in the steady-state,

$$R(t) = e^{-M(t-t')} S dt' \quad (2.17)$$

$$= M^{-1} S. \quad (2.18)$$

This yields the density matrix element

$$\sigma_{ba} = \frac{-i\Omega_1 (i\delta - \Gamma_{ca}) / 2}{(i\Delta_1 - \Gamma_{ba}) (i\delta - \Gamma_{ca}) + (\Omega_2/2)^2}. \quad (2.19)$$

Using the definition of the atomic polarization:

$$\tilde{P} = 2N\mu\sigma e^{-i\omega_1 t} \quad (2.20)$$

$$= \varepsilon_0 \chi E, \quad (2.21)$$

the susceptibility $\chi = \chi' + i\chi''$ can be obtained from the density matrix element and written as

$$\chi' = \frac{2N |\mu_{ba}|^2 \Gamma_{ca} (\delta\Gamma_{ba} + \Delta_1 \Gamma_{ca}) - \delta \left[\delta\Delta_1 - \Gamma_{ba}\Gamma_{ca} - (\Omega_2/2)^2 \right]}{\varepsilon_0 \hbar \left[\delta\Delta_1 - \Gamma_{ba}\Gamma_{ca} - (\Omega_2/2)^2 \right]^2 - (\delta\Gamma_{ba} + \Delta_1 \Gamma_{ca})^2} \quad (2.22)$$

$$\chi'' = \frac{2N |\mu_{ba}|^2 \delta (\delta\Gamma_{ba} + \Delta_1 \Gamma_{ca}) - \Gamma_{ca} \left[\delta\Delta_1 - \Gamma_{ba}\Gamma_{ca} - (\Omega_2/2)^2 \right]}{\varepsilon_0 \hbar \left[\delta\Delta_1 - \Gamma_{ba}\Gamma_{ca} - (\Omega_2/2)^2 \right]^2 - (\delta\Gamma_{ba} + \Delta_1 \Gamma_{ca})^2}, \quad (2.23)$$

where N is the number density and ε_0 is the permittivity in free space. The response of the system on the probe field (atomic polarization) is related to this susceptibility.

For the Ξ system, the same pair of coupled equations (Eqs. 2.14 and 2.15) is obtained with the same assumptions as Eqs. 2.12 and 2.13. The differing elements are the rotating frame, the definitions of the detuning, and the dephasing rates as shown below. For completeness, the Ω_2 terms in the coupled equations have their conjugations flipped.

$$\rho_{ba} = \sigma_{ba} e^{-i\omega_1 t}, \quad (2.24a)$$

$$\rho_{bc} = \sigma_{bc} e^{-i\omega_2 t}, \quad (2.24b)$$

$$\rho_{ca} = \sigma_{ca} e^{-i(\omega_1 + \omega_2)t}, \quad (2.24c)$$

with $\delta = \Delta_1 + \Delta_2$, where $\Delta_2 = \omega_2 - \omega_{cb}$, and

$$\Gamma_{ac} = \frac{1}{2} (\gamma_{bc} + \gamma_{ac}), \quad (2.25a)$$

$$\Gamma_{ab} = \frac{1}{2} \gamma_{ab}, \quad (2.25b)$$

$$\Gamma_{bc} = \frac{1}{2} (\gamma_{ab} + \gamma_{ac} + \gamma_{bc}). \quad (2.25c)$$

In the V system, since there is a strong field coupling the lowest ground state, only the following assumption is made:

$$\sigma_{bb}(t=0) = \sigma_{cc}(t=0) = \frac{1}{2}, \quad (2.26)$$

and this rotating frame is used

$$\rho_{ab} = \sigma_{ab} e^{-i\omega_1 t}, \quad (2.27a)$$

$$\rho_{bc} = \sigma_{bc} e^{i\omega_2 t}, \quad (2.27b)$$

$$\rho_{ac} = \sigma_{ca} e^{-i(\omega_1 - \omega_2)t}. \quad (2.27c)$$

The equations of motion are

$$\dot{\sigma}_{ab} = (i\Delta_1 - \Gamma_{ba}) \sigma_{ba} - \frac{i}{2}\Omega_2 \sigma_{ac} + \frac{i}{4}\Omega_1, \quad (2.28)$$

$$\dot{\sigma}_{ac} = (i\delta - \Gamma_{ac}) \sigma_{ac} - \frac{i}{2}\Omega_2^* \sigma_{ab} + \frac{i}{2}\Omega_1 \sigma_{bc}, \quad (2.29)$$

$$\dot{\sigma}_{bc} = -(i\Delta_2 + \Gamma_{bc}) \sigma_{bc} + \frac{i}{2}\Omega_1^* \sigma_{ac}, \quad (2.30)$$

where the decoherence rates are

$$\Gamma_{ac} = \frac{1}{2}(\gamma_{bc} + \gamma_{ba} + \gamma_{ca} + \gamma_{ac}), \quad (2.31a)$$

$$\Gamma_{ab} = \frac{1}{2}(\gamma_{bc} + \gamma_{ac}), \quad (2.31b)$$

$$\Gamma_{cb} = \frac{1}{2}(\gamma_{ba} + \gamma_{ca}). \quad (2.31c)$$

The matrix components of the equations of motion are

$$R = \begin{bmatrix} \sigma_{ab} \\ \sigma_{ac} \\ \sigma_{bc} \end{bmatrix}, \quad M = \begin{bmatrix} i\Delta_1 - \Gamma_{ba} & -\frac{i}{2}\Omega_2 & 0 \\ -\frac{i}{2}\Omega_2 & i\delta - \Gamma_{ac} & \frac{i}{2}\Omega_1 \\ 0 & \frac{i}{2}\Omega_1 & -i\Delta_2 - \Gamma_{bc} \end{bmatrix}, \quad A = \begin{bmatrix} -\frac{i}{4}\Omega_1 \\ 0 \\ 0 \end{bmatrix}. \quad (2.32)$$

This set of equations of motion can be evaluated in the same manner as before using the matrix inversion method to yield

$$\sigma_{ab} = \frac{-\frac{i}{4}\Omega_1 \left[(i\delta - \Gamma_{ca})(-i\Delta_2 - \Gamma_{bc}) + |\Omega_1/2|^2 \right]}{(i\Delta_1 - \Gamma_{ba}) \left[(i\delta - \Gamma_{ca})(-i\Delta_2 - \Gamma_{bc}) + |\Omega_1/2|^2 \right] - |\Omega_2/2|^2 (i\Delta_2 + \Gamma_{bc})}, \quad (2.33)$$

and the susceptibility

$$\chi = -i \frac{N |\mu_{ba}|^2}{\varepsilon_0 \hbar} \times \frac{(i\delta - \Gamma_{ca})(-i\Delta_2 - \Gamma_{bc}) + |\Omega_1/2|^2}{(i\Delta_1 - \Gamma_{ba}) \left[(i\delta - \Gamma_{ca})(-i\Delta_2 - \Gamma_{bc}) + |\Omega_1/2|^2 \right] - |\Omega_2/2|^2 (i\Delta_2 + \Gamma_{bc})}. \quad (2.34)$$

The real and imaginary parts of the density matrix element (which is related to the response of the probe field) of the three systems for various pump Rabi frequencies, normalized to the radiative lifetime T_1 ($= 1 /$ decay rate of the excited level), are plotted in Fig. 2.5 from Eqs. 2.19 and 2.33. The threshold condition for transparency in the Ξ system is that the pump field be saturating the

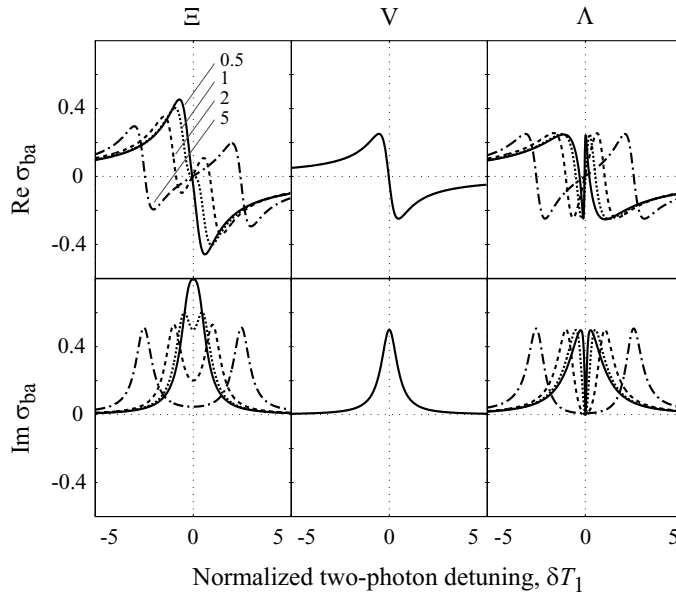


Figure 2.5: Real and imaginary parts of the density matrix element (for the probe field), of the three-level systems, for various normalized pump Rabi frequencies $\Omega_p T_1$.

transition. In that case, the transparency window will be power-broadened instead of being limited by the dephasing rate of the transition between the initial $|a\rangle$ and final state $|c\rangle$. There is no transparency in the V system as the dark state in the V system (which is a superposition of the two excited bare states) “decays” radiatively and therefore is not stable due to the assumption of a weak probe field. In the weakly saturating (pump field) condition, the Λ system has the narrowest transparency feature. This is because the decay rate of the dark state in the Λ system is the dephasing rate between the ground states which is relatively very small. Note that the maximum transparency of the Ξ system is lower than that of the Λ system even in the presence of a strongly saturating pump field ($\Omega_p T_1 = 5$). The condition for transparency can be generalized as follows:

- The transparency starts to appear when the fields saturate the two-photon transition,
- Maximum transparency begins when the pump field saturates the optical transition.

The upper half of Fig. 2.5 is proportional to the real part of the refractive index ($n_0 = \sqrt{1 + 4\pi\chi^{(1)}}$). In the presence of transparency the refractive index changes rapidly, which is the driving force behind slow light experiments.

2.6 Summary

Two related quantum interference effects have been introduced. Although the AC Stark shift in itself is not considered a quantum interference effect, it can be thought of as EIT and CPT residing in the AC Stark shift feature. EIT can be achieved in a variety of systems [48]: two-level, three-level, and four-level systems. In the literature, there is no distinction between EIT and CPT. In this thesis, CPT is classified as the version of EIT in a Λ system and the process is best described using dark and bright states. From the comparison, CPT in the Λ system is “superior” to EIT in the other three-level systems for achieving a narrow transparency feature.

3 The Atomic System

3.1 Introduction

In the previous chapter, quantum interference effects were described for the case of closed, elementary systems. In experiments to observe these effects, such ideal systems are rarely found. Degenerate or extraneous levels are often present in the vicinity of the elementary systems. Nonetheless, an atomic system is usually the most ideal medium for experiments. In particular, sodium is chosen for this work despite some of its complications.

3.2 Atomic Energy Level Structure

The energy level structure of any atom is defined by quantum numbers representing the various momentum due to the motion of both the electron and the nucleus. The shells or electron orbits are defined by the quantum number n . The angular momentum of shell n is quantized, and

$$p = mvr = n \frac{h}{2\pi} \tag{3.1}$$

$$\begin{aligned} 2\pi r &= n \frac{h}{mv} \\ &= n\lambda, \end{aligned} \tag{3.2}$$

where λ is the de Broglie wavelength¹, m is the mass, v is the velocity of the electron, and r is the radius of the orbit. If the angular momentum is not an integer multiple of $\frac{h}{2\pi}$ (\hbar), then there is destructive interference and the wavefunction of the electron will collapse.

According to Sommerfeld, n measures the long axis of the elliptical electron orbit and a new quantum number k defines the ellipticity, where $k = 1, 2, \dots, n$. The case of $k = n$ represents a circular orbit and $k = 0$ is rejected since it meant the electron would move through the nucleus. With wave mechanics and Heisenberg's uncertainty principle, where the electron is "smeared" out over space, the $k \neq 0$ restriction does not hold and a new quantum number is used where $l = k - 1$. For a given n , there are n different values of l (0, 1, ..., $n-1$). The different values of l defines the electron type. The electrons are named as followed:

$$\begin{aligned}
 l = 0 & \quad \text{s electron,} \\
 l = 1 & \quad \text{p electron,} \\
 l = 2 & \quad \text{d electron,} \\
 l = 3 & \quad \text{f electron,}
 \end{aligned}
 \tag{3.3}$$

and for emissive transitions, they are designated as:

$$\begin{aligned}
 k = 1 \rightarrow k = 2 & \quad \text{sharp series (e.g. 4s} \rightarrow \text{3p),} \\
 k = 2 \rightarrow k = 1 & \quad \text{principle series (e.g. 3p} \rightarrow \text{3s, D lines of Na),} \\
 k = 3 \rightarrow k = 2 & \quad \text{diffuse series (e.g. 3d} \rightarrow \text{3p),} \\
 k = 4 \rightarrow k = 3 & \quad \text{fundamental series (e.g. 4f} \rightarrow \text{3d).}
 \end{aligned}
 \tag{3.4}$$

Since the electron spins around its axis, it acts like a tiny magnet and interact with the orbital motion of the electron. The different respective orientation of the momenta results in different energies and a new quantum number j , where $j = l \pm s$ is required, and s is the quantum number representing the spin momentum of the electron. For $s \leq l$, there are $(2s + 1)$ possible j values and this value is called the "multiplicity" of the energy level described by the quantum number l . For a multiple electron system, uppercase is used for the quantum numbers, e.g. L for the case of the total electron orbital angular momentum where $L_{max} = \sum_i |l_i|$.

¹The de Broglie wavelength is the wavelength of the standing wave of the electron wavefunction. Although it is not entirely correct to say that it is the wavelength of the standing wave of the electron (particle) orbit as in the old quantum theory, the model of a corpuscle orbiting the nucleus (Bohr atom) is used to provide a conceptual picture.

The electron orbital angular momentum \mathbf{L} , its \hat{z} -component L_z , the electron spin angular momentum \mathbf{S} , its \hat{z} -component S_z , the total electron angular momentum \mathbf{J} , and its \hat{z} -component J_z are thus characterized by the quantum numbers l , m_l , s , m_s , j , and m_j respectively. \mathbf{J} is the vectorial sum of \mathbf{L} and \mathbf{S} . The magnitude of the total electron angular momentum and its \hat{z} -component are

$$\mathbf{J} = \hbar\sqrt{j(j+1)} \quad (3.5)$$

$$J_z = \hbar m_j. \quad (3.6)$$

The same relation holds for the electron orbital and spin momenta.

For s electrons ($l = 0$), there are no magnetic moment so the energy of the system is independent on spin orientation (no doublets for $s = \frac{1}{2}$). The inner shells also have $\mathbf{L} = 0$ or $\mathbf{S} = 0$ since they are closed shells. Only the valence electrons define the values of \mathbf{L} and \mathbf{S} , and therefore the physical and chemical properties of the atom (a noble atom has a full outer shell). The revolution of the nucleus also produces a nuclear angular momentum \mathbf{I} . An energy level characterized by the quantum numbers l , s , and j is split into $(2j + 1)$ different energy levels when it interacts with the spin magnetic dipole moment of the nucleus, defined by the quantum number F , where the total atomic angular momentum is

$$\mathbf{F} = \mathbf{J} + \mathbf{I}. \quad (3.7)$$

The atom with $\mathbf{J} \neq 0$ acts like a magnet and will try to orient itself to an external magnetic field. In the presence of a weak external magnetic field, each level defined by F is split into $(2F + 1)$ number of levels characterized by the quantum number m_F . The atom having angular momentum $\hbar\sqrt{j(j+1)}$ has $(2j + 1)$ possible orientations in a strong external magnetic field because the component P_H of the total angular momentum vector \mathbf{P} in the direction of the magnetic field \mathbf{H} can have the values

$$P_H = \hbar m_F \quad (m_F = -j, = j + 1, \dots, j - 1, j). \quad (3.8)$$

The component μ_H of the total magnetic moment μ_m in the direction of the magnetic field \mathbf{H} is

$$\mu_H = -\mu_B g m_F, \quad (3.9)$$

where g is the Landé g -factor

$$g = 1 + \frac{j(j+1) + s(s+1) - l(l+1)}{2j(j+1)}, \quad (3.10)$$

and the Bohr magneton is

$$\mu_B = \left(\frac{\mu_0 e \hbar}{2m} \right). \quad (3.11)$$

The above mentioned interaction between the electron's spin magnetic dipole moment and the internal magnetic field due to the electron orbital motion, called the *spin-orbit interaction* ($\mathbf{L} \cdot \mathbf{S}$), creates the fine structure. The spin-orbit interaction has the value

$$\mathbf{L} \cdot \mathbf{S} = \frac{\hbar^2}{2} [j(j+1) - l(l+1) - s(s+1)]. \quad (3.12)$$

The interaction between the internal magnetic field produced by the motion of the electron with angular momentum \mathbf{J} and the spin magnetic dipole moment of the nucleus with angular momentum \mathbf{I} creates the hyperfine structure labelled by \mathbf{F} . The magnetic moment μ_m , created by the revolution of a negative point charge, couples with an external applied magnetic field to produce the Zeeman sublevels.

The nomenclature for defining a level in the fine structure is, for example:

$$3^2 S_{1/2} \quad (3.13)$$

where the 3 is the quantum number n , the superscript 2 is the j multiplicity ($2s+1$), S denotes a s electron ($l=0$), and the subscript $\frac{1}{2}$ is the j value ($l+s$). The number of electrons are defined by a superscript outside a parenthesis, e.g. $(2p)^3$ denotes 3 $2p$ -electrons.

m_l can have $(2l+1)$ values: $-l, (-l+1), \dots, (l-1), l$. For $s = \frac{1}{2}$, m_s can have two values, $-\frac{1}{2}$ and $+\frac{1}{2}$. The total number of different m_l and m_s combinations for a given l is $2(2l+1)$. A subshell (n and l given) is filled if it contains $2(2l+1)$ electrons. An s -subshell can thus have 2 electrons, a p -subshell 6 electrons, a d -subshell 10 electrons and an f -subshell 14 electrons. Therefore, the $n=2$ shell has 8 electrons: 2 in the $l=0$ subshell and 6 in the $l=1$ subshell. This is due to Pauli's exclusion principle which states that:

No two electrons can have an identical set of quantum numbers n, l, m_l , and m_s .

Therefore, an electron is characterized by these four quantum numbers. The transition selection

rules for an optical transition are [49].

$$\begin{aligned}
 \Delta L &= \pm 1, \\
 \Delta S &= 0, \\
 \Delta J &= 0, \pm 1, \\
 J = 0 &\rightarrow J = 0 \text{ is forbidden, e.g. } s \text{ to } s \text{ state,} \\
 \Delta M &= \pm 1.
 \end{aligned}
 \tag{3.14}$$

In an atomic system, transitions between hyperfine ground levels and between hyperfine excited levels are electric dipole forbidden. Therefore, the hyperfine ground levels intrinsically have very long lifetimes.

3.3 Atomic Sodium

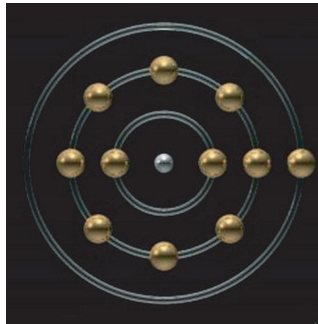


Figure 3.1: Atomic structure of sodium showing a single valence electron.

Atomic sodium Na^{23} is a metallic alkali [50] and has an atomic number of 11. It is a hydrogenoid atom, i.e. a single valence-electron orbiting the quasi-nucleus which consist of the protons and the other 10 inner shell electrons (each circle in Fig. 3.1 represents an n shell). Without the complication of multiple valence electrons, it is therefore well suited to be used in research. Sodium is also highly nonlinear with a principle absorption line in the optical frequencies, facilitating the alignment of experiments. The versatility of sodium also contributes to its popularity in research laboratories. Spectroscopic studies can be carried out in the homogeneously-broadened limit with an atomic beam or a magneto-optic trap (MOT), and Doppler features can be observed in a vapor cell or a heatpipe. However, sodium is highly corrosive and reacts strongly with oxygen. At room temperature it is a

silvery white solid. During the chemical reaction with water, white powder-like sodium peroxide Na_2O_2 and sodium oxide Na_2O are formed and hydrogen is released.

The highest occupied state (ground level) where the single valence electron resides in is the 3s orbital. This electron has a doublet structure due to the spin-orbit interaction: the 3s level is a singlet while the 3p level is a doublet (the fine structure). The ground level, however, has zero electronic magnetic moment; therefore the ground level energy of the system is independent of the orbital spin orientation. Excitations from the 3s to the 3p orbital are the famous *D* lines at 5896 Å and 5890 Å [51]. The nuclear spin of $I = \frac{3}{2}$ of sodium combines with each value of the total electronic angular momentum \mathbf{J} to produce the hyperfine structure. The hyperfine structure of the *D1* line ($3^2S_{1/2} - 3^2P_{1/2}$) at 5896 Å consist of two hyperfine ground levels 1772 MHz apart, and two hyperfine excited levels 189 MHz apart as shown in Fig. 3.2². The hyperfine levels are labelled by F , and each hyperfine level itself is $(2F + 1)$ -degenerate. By applying a magnetic field in the direction of propagation of the laser beam (quantization axis, \hat{z}), this degeneracy can be lifted and we have the Zeeman (magnetic) sublevels as shown in Fig. 3.3 [52]. In the weak field regime, the amount of energy shift due to the *anomalous Zeeman effect* [53] is

$$\Delta E_{|F m_F\rangle} = \mu_B g_F m_F B_z, \quad (3.15)$$

where g_F is the hyperfine Landé g -factor, m_F is the quantum number of the z -component of the total angular momentum, and B_z is the z -component (quantization axis) of the applied magnetic field. In the strong magnetic field regime, the energy shift is called the *Paschen-Back effect* [54].

For the purpose of studying optical transitions, it is often convenient to take the quantization axis to be parallel to the electric field vector of the laser beam (x -axis). In this case, for a linearly polarized field, the field is called π -polarized that couples levels with $\Delta m_F = 0$. A right (left)-hand-circularly polarized field σ_+ (σ_-) couples levels with $\Delta m = +1$ ($\Delta m = -1$). A linearly polarized field that is orthogonal to the quantization axis can be decomposed into right and left-hand-circular polarization. The Clebsch-Gordon coefficients used to calculate the dipole matrix element of each transition in the *D1* line of sodium are given in Table 3.1 (see Appendix B of [55] and Complement B_X of [56]).

²Redrawn from [51]

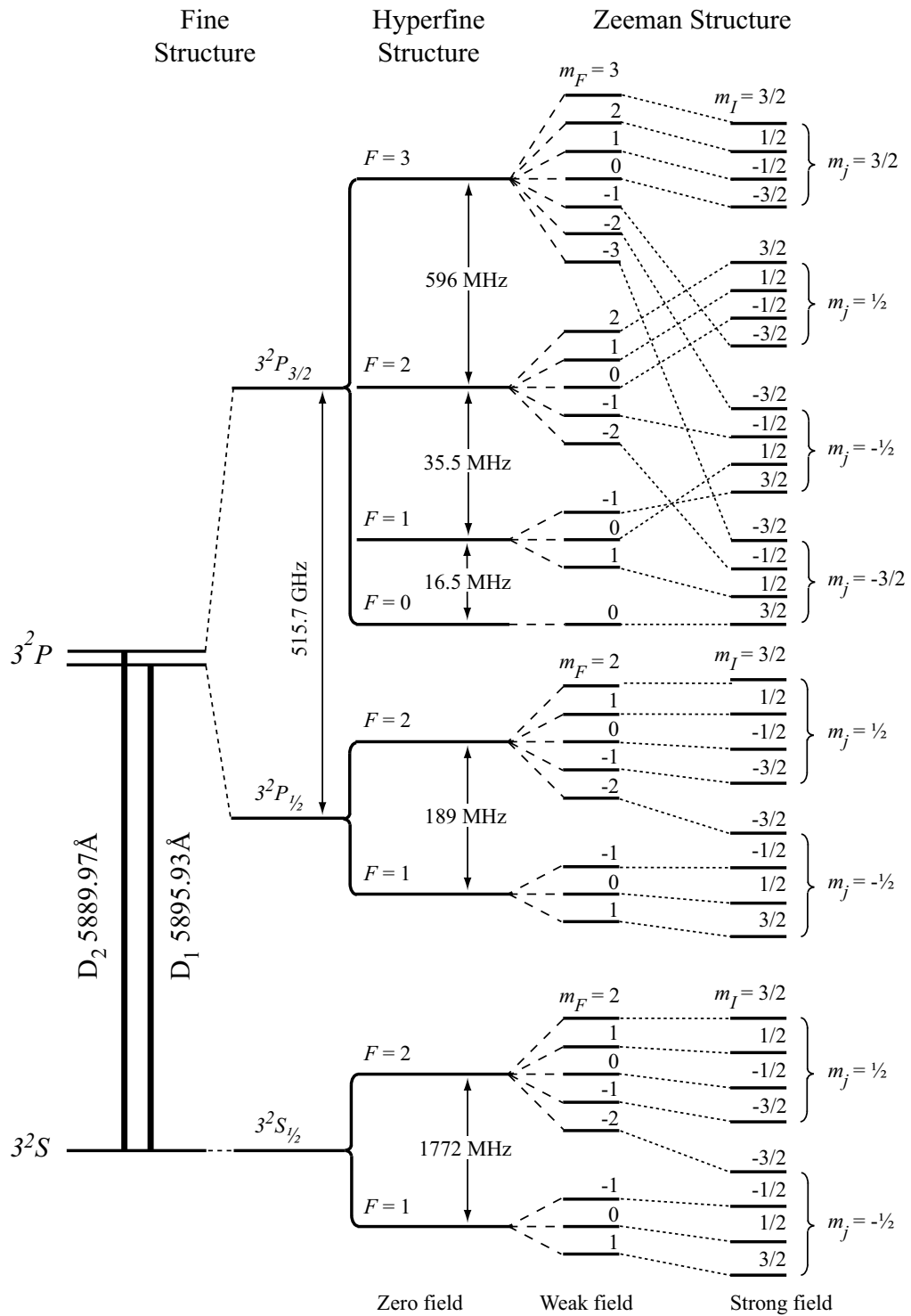


Figure 3.2: Energy level structure of the two D lines of atomic sodium.

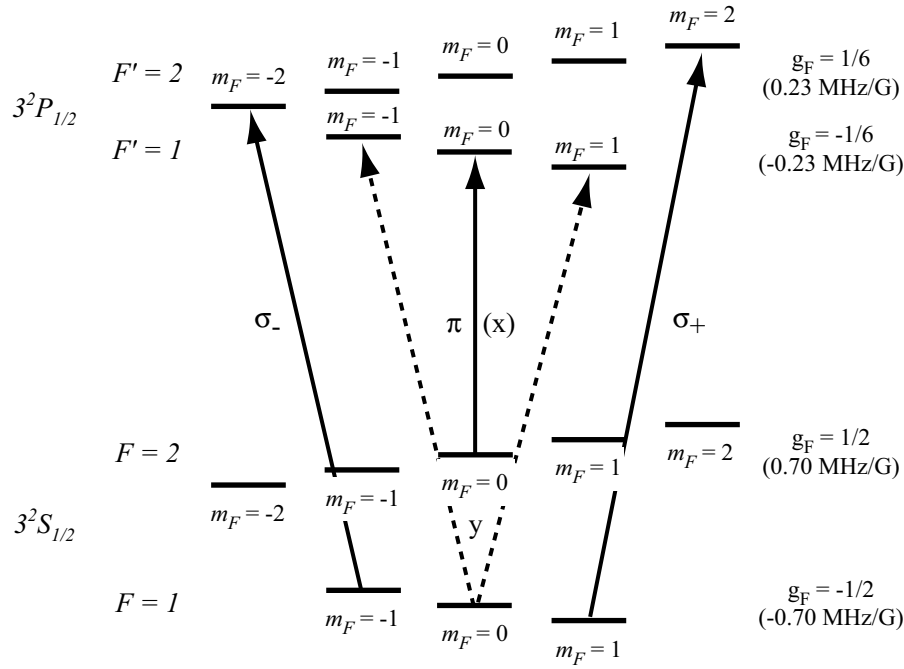


Figure 3.3: Energy shifts of the Zeeman levels in the presence of a weak magnetic field.

	$ 1, -1\rangle$	$ 1, 0\rangle$	$ 1, 1\rangle$	$ 2, -2\rangle$	$ 2, -1\rangle$	$ 2, 0\rangle$	$ 2, 1\rangle$	$ 2, 2\rangle$
$\langle 1, -1 $	$\sqrt{\frac{1}{36}} \hat{z}$	$-\sqrt{\frac{1}{36}} \hat{\sigma}_+$		$\sqrt{\frac{1}{6}} \hat{\sigma}_-$	$\sqrt{\frac{1}{12}} \hat{z}$	$\sqrt{\frac{1}{36}} \hat{\sigma}_+$		
$\langle 1, 0 $	$-\sqrt{\frac{1}{36}} \hat{\sigma}_-$		$-\sqrt{\frac{1}{36}} \hat{\sigma}_+$		$\sqrt{\frac{1}{12}} \hat{\sigma}_-$	$\sqrt{\frac{1}{9}} \hat{z}$	$-\sqrt{\frac{1}{12}} \hat{\sigma}_+$	
$\langle 1, 1 $		$-\sqrt{\frac{1}{36}} \hat{\sigma}_-$	$-\sqrt{\frac{1}{36}} \hat{z}$			$\sqrt{\frac{1}{36}} \hat{\sigma}_-$	$\sqrt{\frac{1}{12}} \hat{z}$	$-\sqrt{\frac{1}{6}} \hat{\sigma}_+$
$\langle 2, -2 $				$\sqrt{\frac{1}{6}} \hat{\sigma}_+$	$\sqrt{\frac{1}{18}} \hat{\sigma}_+$			
$\langle 2, -1 $		$-\sqrt{\frac{1}{12}} \hat{\sigma}_+$		$-\sqrt{\frac{1}{9}} \hat{z}$	$-\sqrt{\frac{1}{36}} \hat{z}$	$\sqrt{\frac{1}{12}} \hat{\sigma}_+$		
$\langle 2, 0 $	$-\sqrt{\frac{1}{36}} \hat{\sigma}_-$	$\sqrt{\frac{1}{9}} \hat{z}$	$\sqrt{\frac{1}{36}} \hat{\sigma}_+$		$\sqrt{\frac{1}{12}} \hat{\sigma}_-$		$\sqrt{\frac{1}{12}} \hat{\sigma}_+$	
$\langle 2, 1 $		$-\sqrt{\frac{1}{12}} \hat{\sigma}_-$	$\sqrt{\frac{1}{12}} \hat{z}$			$\sqrt{\frac{1}{12}} \hat{\sigma}_-$	$\sqrt{\frac{1}{36}} \hat{z}$	$\sqrt{\frac{1}{18}} \hat{\sigma}_+$
$\langle 2, 2 $			$-\sqrt{\frac{1}{6}} \hat{\sigma}_-$				$\sqrt{\frac{1}{18}} \hat{\sigma}_-$	$\sqrt{\frac{1}{9}} \hat{z}$

Table 3.1: Clebsch-Gordan coefficients for the $D1$ line of sodium.

3.4 Inhomogeneous Broadening

With an ensemble of atoms, like in a vapor cell, inhomogeneous broadening is present. In this case, the broadening is Doppler [57]. This is due to the motion of the sodium atoms in the cell having different velocities. The frequency of the light that the atom “sees” is shifted and this effect is only present if the atom is moving in the same axis as the optical beam. If the optical beam is propagating

in the positive z direction, then the (angular) frequency of the beam the atom sees is

$$\omega = \omega_0 - kv_z, \quad (3.16)$$

where ω_0 is the actual (angular) frequency of the optical beam, k is the wavevector of the photon and v_z is the z -component of the velocity of the atom. A Maxwell-Boltzmann distribution is often used to represent the spread of velocities of the atoms. In the z axis, the number of atoms at velocity v is

$$n(v) = \frac{N}{\sqrt{2\pi\sigma_D^2}} e^{-v^2/2\sigma_D^2}, dv, \quad (3.17)$$

where N is the total number of atoms, the most probable speed $v_{RMS} = \sigma_D = \sqrt{k_B T/m}$, with k_B the Boltzmann constant, T the temperature in degree Kelvin, and m the atomic mass³. The Doppler halfwidth $\Delta\omega_D$ is

$$\Delta\omega_D = \sqrt{2 \ln 2} k v_{RMS} \quad (3.18)$$

$$= \frac{\omega_0}{c} \sqrt{2 \ln 2} \frac{k_B T}{m}. \quad (3.19)$$

For two-photon effects, Doppler broadening can often be reduced by using the appropriate configuration: counter-propagating fields are used for a Ξ system, and co-propagating fields are used for a V or Λ system. This configuration allows for the two fields to experience the appropriate frequency shifts to maintain the two-photon resonance condition. The detuning from an atomic transition (ω_{ba}) is

$$\Delta_{ba} = \omega - \omega_{ba} \quad (3.20)$$

$$= \omega_0 - \omega_{ba} - kv \quad (3.21)$$

$$= \Delta_{ba,0} - kv. \quad (3.22)$$

The subscript 0 denotes the detunings of an atom at rest. If the two fields are at an angle ($k_1 \neq k_2$), the amount of residual broadening is increased. Even with the two beams being collinear, if they have different frequencies, residual Doppler broadening will still be present. For a Raman transition, i.e. in a Λ system, the fields with frequencies ω_1 and ω_2 are assumed to couple to the transitions

³Sodium has an atomic mass of 23, i.e. $m = 23u$, where u is the atomic mass unit.

$|a\rangle \rightarrow |b\rangle$ and $|c\rangle \rightarrow |b\rangle$ respectively. For an atom with velocity v , the two-photon (Raman) detuning is

$$\delta = \Delta_{ba} - \Delta_{cb} \quad (3.23)$$

$$= \Delta_{ba,0} - \Delta_{bc,0} - k_1 v + k_2 v \quad (3.24)$$

$$= \delta_0 - (\omega_1 - \omega_2)v/c, \quad (3.25)$$

where the second term in Eq. 3.25 is the residual Doppler broadening term.

3.5 Summary

The energy level structure of atomic sodium was explained. As can be seen, sodium is not a two level atom. With this elaborated structure, a rich variety of processes can be observed in this system. The concept of inhomogeneous broadening was also introduced.

4 Laser Spectroscopy and Optical Coherence Effects

4.1 Introduction

Laser spectroscopy has been widely used to study the properties of material systems. These techniques involve various coherent, incoherent, linear and nonlinear effects. Among the more commonly used methods are saturation spectroscopy and coherent Raman scattering.

Since the coherence length of the laser fields are very long, optical coherence effects are often studied using lasers as well. Two particular phenomena that will be discussed here are slow light and self phase modulation.

4.2 Optical Pumping

When a saturating field is applied to the system, saturation effects and optical pumping can occur. Optical pumping [58, 59] is one of the earliest optical processes discovered, even before the invention of the laser. Its manifestation however is very varied and many new phenomena are still attributed to optical pumping. These processes are most prominent in a Doppler-broadened medium having a resonance feature with a width around the natural linewidth, within the much broader Doppler spectrum.

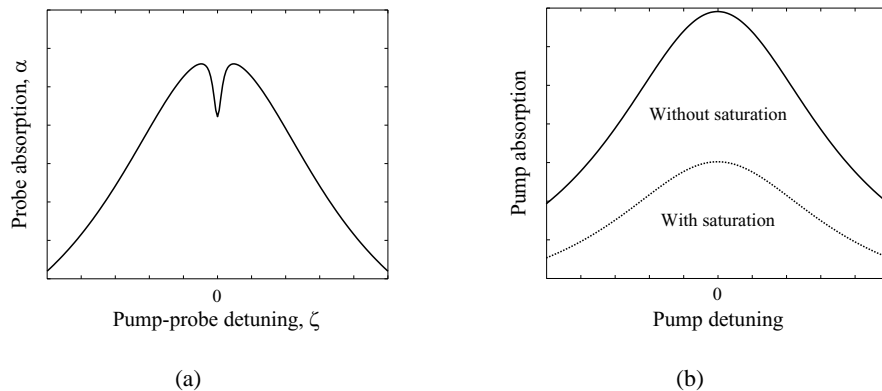


Figure 4.1: (a) Probe absorption spectrum showing a spectral hole. (b) Pump absorption spectrum with and without saturation.

4.2.1 Hole burning in a two-level system

The most famous saturation effect is the Lamb dip [60, 61], which is a particular form (counter-propagating, degenerate laser frequency) of spectral hole burning as shown in Fig. 4.1(a). A spectral hole is usually observed in a Doppler-broadened two-level atomic medium. The weaker probe field can be applied copropagating or counter-propagating to the saturating pump field. For a particular velocity sub-group of atoms, the pump field drives population into the upper level thereby depleting the population of the ground level. The pump field will experience saturation and the absorption of the pump field will also be reduced. Figure 4.1(b) shows the absorption of the pump field as it is scanned across the Doppler profile. A continuous series of spectral holes are “burned” resulting in an overall reduction of the absorption spectrum (dotted line).

The steady-state absorption of the probe field α is given by a product of two factors: the absorption cross-section, and the population inversion ($\rho_{bb} - \rho_{aa}$):

$$\alpha \propto \frac{\rho_{bb} - \rho_{aa}}{(\omega - \omega_{ba}) + i/T_2 + i\Omega}. \quad (4.1)$$

The absorption cross-section (the inverse of the denominator of Eq. 4.1) depends on the probe field’s detuning in the usual way: peaking when the probe field is resonant with the transition. In this counter-propagating configuration, the fields are resonant simultaneously only for one velocity sub-group of atoms, e.g. those that are at rest if the pump field is on resonance. The population amplitude plot versus atom velocity is similar to Fig. 4.1(a). For this sub-group of atoms, the probe absorption is reduced because the population in the ground level is depleted by the pump field.

For other sub-groups, the hole burnt by the pump field is not seen by the probe field as the latter is detuned away from resonance. The spectral width of the hole is generally proportional to the inverse of the homogeneous lifetime ($1/T_2 = 1/2T_1$) and can be power-broadened (the Rabi frequency term Ω in the denominator of Eq. 4.1). If the pump field is much stronger than the saturation intensity of the transition, drastic change in the absorption spectrum such as the Autler Townes splitting can also be observed. However, since the spectrum is Doppler-broadened, much higher pump intensities are required to separate the Autler Townes features.

4.2.2 Optical pumping in a Λ system

Optical pumping is a little different in a Λ system. When a strong field ω_p is applied to the transition coupling the lower ground level, population is transferred from the ground level to the excited level. That population can then either decay back to the original ground level or to the other (upper) ground level. The latter results in the depletion of population in the first ground level as shown by the size of the circles representing population in Fig. 4.2(a), therefore reducing the absorption of the pump field. If a probe field ω_s is applied to the other transition, for a particular velocity subgroup of atoms, the probe field will experience increased absorption due to the increased population in the upper ground level. CPT will occur, when the two fields are on Raman resonance, amid a broader induced absorption background (inside the even broader Doppler spectrum) as shown by the solid curve in Fig. 4.2(b). At very high pump intensities, the induced absorption background broadens (dotted curve).

4.2.3 Difference frequency crossing in a V system

A saturation effect in a V system that creates an absorption dip is the difference frequency crossing (DFC) resonance. The absorption cross-section peaks when the probe field is resonant with the $|a\rangle \rightarrow |c\rangle$ transition, and the pump field saturates the system when it is resonant with the $|a\rangle \rightarrow |d\rangle$ transition. This causes the ground level population to be partially depleted as shown in Fig. 4.3(a). In a Doppler-broadened medium, each factor is resonant for a particular velocity subgroup of atoms. If the pump-probe detuning $\zeta = -\omega_{dc}$, then the resonance in the ground level depletion occurs for the velocity subgroup that has the largest absorption cross-section. This double-resonance makes the

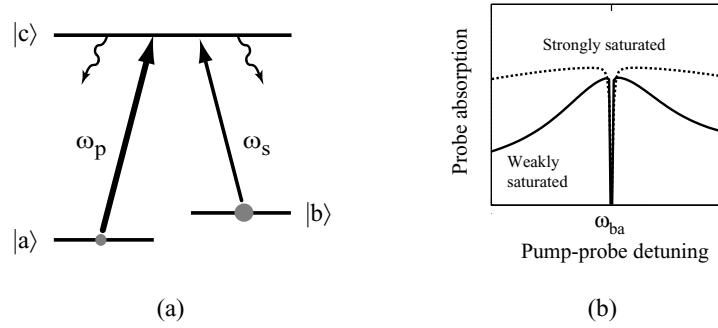


Figure 4.2: (a) Optical pumping in a Λ system depicting depletion of population in the lower ground level. (b) Absorption of the probe field in the presence of a weakly and strongly saturating pump field.

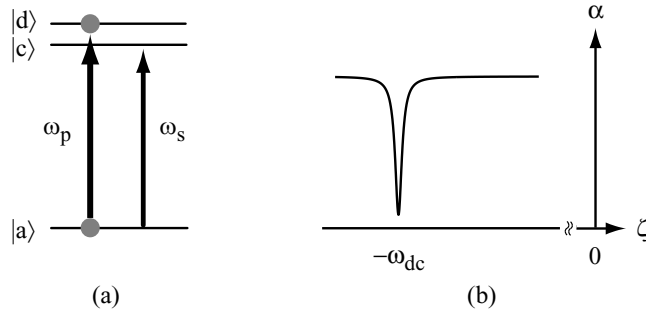


Figure 4.3: Difference-frequency crossing resonance in a V system. (a) Energy level diagram showing the V system. (b) Resulting absorption dip for a red-detuned probe field.

dominant contribution to the probe absorption as seen in Fig. 4.3(b), and the absorption is reduced. But if $\zeta \neq \omega_{dc}$, the resonance of the ground level depletion occurs for a velocity subgroup that has a low absorption cross-section, and the impact of ground level depletion on the absorption is negligible.

This feature can be understood mathematically as

$$\alpha(\omega_s - \omega_p - \omega_{dc}) = \int N \sigma(\omega_s - \omega_{ca} - kv) \rho_{aa}(\omega_p - \omega_{da} - kv) g(kv) d(kv), \quad (4.2)$$

where α is the probe absorption in the presence of the pump field, N is the number of atoms, σ is the absorption cross-section, ρ_{aa} is the population of ground level $|a\rangle$, and g is the Maxwellian Doppler profile. For simplicity the fields are assumed to be tuned close to resonance, so that only small values of kv are relevant, and $g(kv)$ can be ignored. It has been shown in [62] that as long as

$|\zeta - \omega_{dc}| \ll kv$, the fields can be detuned appreciably from their individual single-photon transitions (Doppler half-width) without affecting the size of the nonlinear polarization. Equation 4.2 can then be written as a convolution function

$$\alpha(\Delta') = N \int \sigma(\Delta' + \Delta) \rho_{aa}(\Delta) d\Delta, \quad (4.3)$$

where $\Delta' = \zeta - \omega_{dc}$ and $\Delta = \omega_p - \omega_{da} - kv$. The linewidth of the resonance is the sum of those of the two functions (σ and ρ_{aa}) in the integral. In the limiting case of only radiative broadening, both σ and ρ_{aa} are lorentzians with a width of the homogeneous linewidth. The linewidth of the DFC resonance will therefore be twice the homogeneous width. The lorentzians are replaced with their power-broadened versions for larger field intensities.

This DFC resonance is the nondegenerate (in laser frequency), co-propagating analogue of the crossover resonance studied in [63]. The analysis here is similar to that of Schlossberg and Javan [62] (see Eq. 21 for travelling waves), and Feld and Javan in their section on a V system (see Eq. 54 of [64]).

4.2.4 Cross-transition resonance in a double Λ system

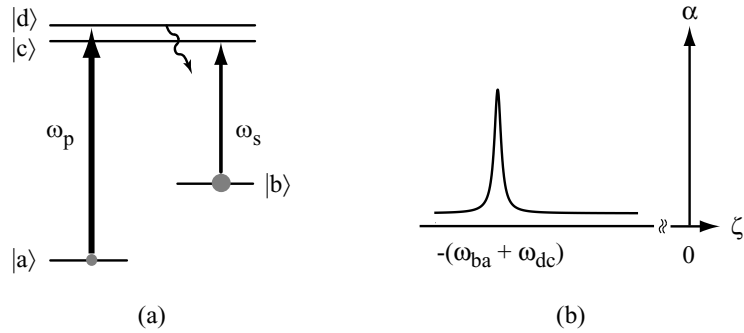


Figure 4.4: Cross-transition resonance in a double- Λ system. (a) Energy level diagram showing optical pumping from ground level $|a\rangle$ to ground level $|b\rangle$ through spontaneous emission. (b) Enhanced absorption for a red-detuned probe field.

Optical pumping in a double Λ system is a little more involved. Figure 4.4(a) shows the pump and probe fields coupling to transitions that do not share any common levels. CPT does not occur because the fields are resonant (for a particular velocity subgroup of atoms) with different excited

levels. For this velocity subgroup, the pump field drives population to the upper excited state $|d\rangle$ which can decay spontaneously to the other ground level $|b\rangle$. Since the probe field is weaker, the population accumulates in level $|b\rangle$, thereby increasing the population difference ($\rho_{cc} - \rho_{bb}$) of the probe transition or equivalently the probe absorption. The absorption peak shown in Fig. 4.4(b) is obtained at the pump-probe detuning of the frequency difference between the two transitions:

$$\omega_{da} - \omega_{cb} = \omega_{ba} + \omega_{dc}.$$

As mentioned before, the attenuation of the probe field is a product of two factors: the absorption cross-section, and the population inversion. The width of the cross-transition resonance is therefore the sum of the widths of the two relevant functions. At higher pump intensities, the resonance becomes broader and flattens [65] just like the optical pumping effect in the (single) Λ system.

4.3 Wave Mixing

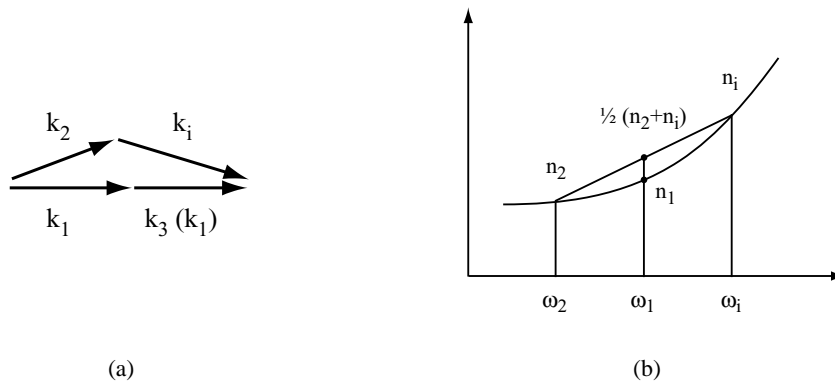


Figure 4.5: (a) Vectorial representation of phase matching in wave mixing processes. (b) Phase mismatch due to difference in the refractive indices.

The process of wave mixing encompasses many varieties from two-beam coupling to phase conjugation to multi-wave mixing processes. The energy conservation rule governs the frequency of each field involved in the process. Phase matching [Fig. 4.5(a)] will determine the efficiency of the mixing. There is a variety of different geometries (collinear, boxcar [66], etc.) for achieving phase matching. For certain collinear wave mixing processes, phase matching is not perfect but the overlap region is longer than in non-collinear ones which might be desirable for certain applications.

For non-degenerate four-wave-mixing in a dispersive two-level atom in the collinear geometries,

perfect phase matching cannot be achieved. This is due to the different refractive indices experienced by the fields at various frequencies. The refractive index at the laser frequency ω_1 and ω_3 is always lower than the average of those experienced by the Stokes ω_2 and anti-Stokes ω_i fields as shown in Fig. 4.5(b). This is not an issue in other systems, e.g. three level systems, since each field is coupling to a different transition and detuned by the same amount from their respective transitions.

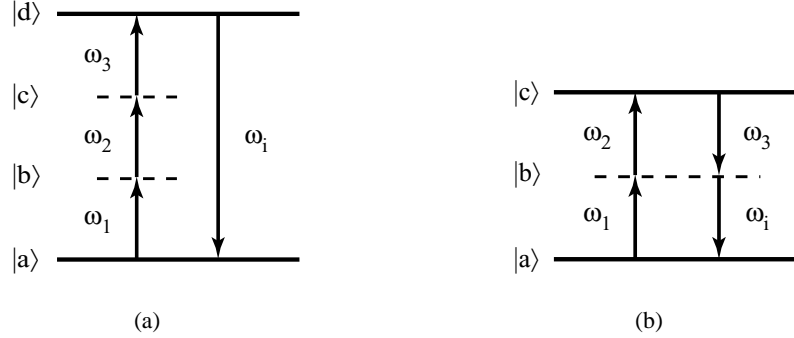


Figure 4.6: Two possible four-wave-mixing configurations.

Four-wave-mixing (FWM) belongs to a group of third order nonlinear processes that generates an idler field whose frequency is a combination of those of the other 3 applied fields. Figure 4.6 shows two possible configurations. ω_1 , ω_2 , and ω_3 are the frequencies of the applied fields and ω_i is the frequency of the generated field. Dashed and solid lines indicate virtual and real levels respectively. A special case of FWM is third-harmonic generation where the idler frequency ω_i is equal to 3ω [Fig. 4.6(a)]. Besides third-harmonic generation and coherent Raman scattering (CRS), all other configurations are generally termed FWM. Within the class of FWM processes, there are degenerate ($\omega_i = \omega_1 = \omega_2 = \omega_3$) and nondegenerate versions. Although the degenerate case looks like self phase modulation, the important difference is that FWM includes more than one applied optical beam, even if they are collinear and copropagating. It also involves the transfer of energy from one beam to another.

4.3.1 Forward degenerate four-wave-mixing in an opened two-level system

In an open two-level system, forward degenerate four-wave-mixing (FDFWM) as depicted in Fig. 4.7 can occur. It is termed “forward” because all the fields, including the generated idler field, are propagating in the same (forward) direction. This process will also occur for 3 separate counterpropa-

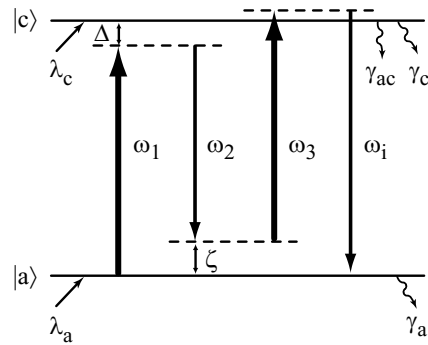


Figure 4.7: Forward degenerate four-wave-mixing in an open two-level system.

gating fields under the name *degenerate four-wave-mixing*.

Each of the two levels has a small decay rate (γ_i) out of the two-level system and a small repopulation rate (λ_i). If ω_1 is designated the pump field and ω_2 the probe field, then Δ is the pump detuning, and ζ is the pump-probe detuning. ω_3 in this case, is equal to ω_1 . In the presence of additional dephasing or decay (for example, to an external reservoir as in an open system) paths out of the two-level system [67], narrowing of the resonance below the natural linewidth occurs only if the additional decay rate for the excited level is larger than the additional decay rate of the ground level. The width of this feature depends on the decay rate of the ground level out of the two-level system (γ_a).

4.3.2 Non-degenerate four-wave-mixing in a V system

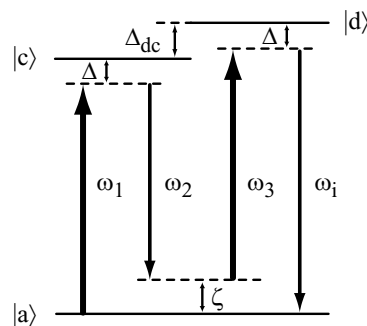


Figure 4.8: Non-degenerate four-wave-mixing in the V system.

Non-degenerate four-wave-mixing (NDFWM) in the V system is shown in Fig. 4.8. If $\omega_1 = \omega_3$,

then the one-photon-detuning of each transition $|a\rangle \rightarrow |c\rangle$ and $|a\rangle \rightarrow |d\rangle$ are the same. The doubly-resonant idler field peaks when ζ matches the frequency separation of the excited levels (ω_{dc}). This process occurs at the same pump-probe detuning as the saturation effect in a V system described earlier, but with the generation of an idler field. Unlike FDFWM described earlier, there is no line narrowing effects, and the width of the resonance is of the order of the homogeneous linewidth that can power-broaden.

4.3.3 Coherent Raman scattering

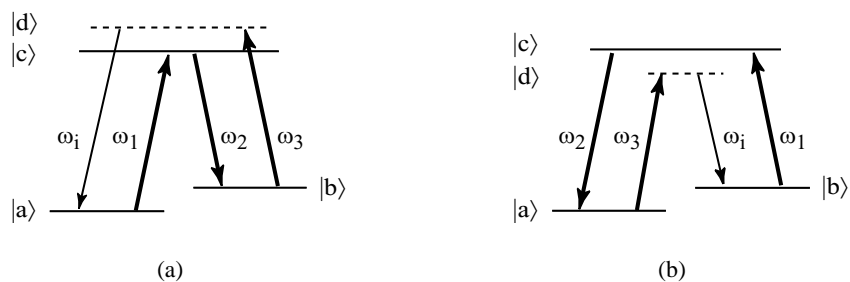


Figure 4.9: The two coherent Raman scattering processes: (a) Coherent anti-Stokes Raman scattering, and (b) coherent Stokes Raman scattering.

A commonly observed FWM process is coherent anti-Stokes Raman scattering (CARS) [68–70] and its counterpart, coherent Stokes Raman (CSRS) scattering. The idler field is labelled an anti-Stokes (Stokes) field if its frequency is higher (lower) than that of the pump field. These coherent Raman scattering processes [65, 71–73] were first observed in molecules and have been widely used as a tool for spectroscopy.

The process of molecular coherent Raman scattering involves two applied fields (ω_1 and ω_2) which are tuned to excite a vibrational or rotational mode. A third applied field (ω_3) can then scatter off this coherently prepared medium and gain (or lose) energy from (to) the vibrational mode to generate the anti-Stokes (Stokes) idler field. When $\omega_1 > \omega_2$ ($\omega_1 < \omega_2$) and $\omega_1 = \omega_3$, this interaction is known as CARS (CSRS). Traditionally, CARS and CSRS operate far away from the single-photon resonance. If the fields are tuned close to the optical transition, the idler can be enhanced and the excited state properties can be studied too, as in resonance Raman scattering [74].

Coherent Raman scattering can also occur in an atomic system, see Fig. 4.9. A ground-state

(spin) coherence or quantum-superposition is created instead of exciting a vibrational mode. As the decoherence rate between the hyperfine ground levels of an atomic system is very low, a very narrow and strong feature can be obtained. Such a process utilizes the same quantum coherence that is responsible for CPT.

4.4 Other Multi-Photon Effects

4.4.1 Self phase modulation

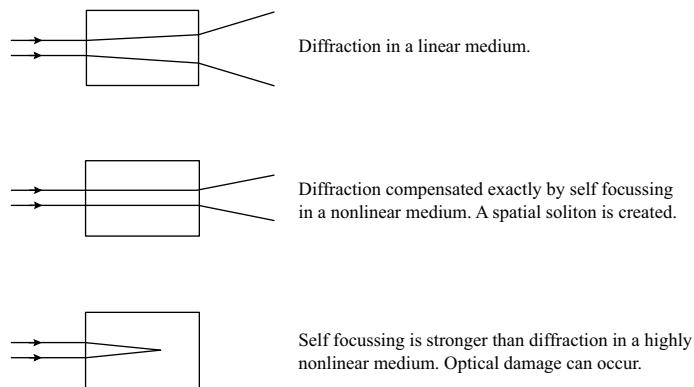


Figure 4.10: Diffraction, soliton formation and self focusing.

An interesting and useful single-field multi-photon process that occurs in a two-level system is self phase modulation (SPM). SPM is a nonlinear process in which the laser beam modifies the optical properties of the medium that acts back on the beam. The most commonly known manifestation of SPM is self-focusing [75]. A beam of light with a gaussian transverse intensity profile propagating through a nonlinear (Kerr) medium causes the refractive index (n) of the medium to change according to the beam's intensity (I), $n = n_0 + n_2 I$, where n_2 is the nonlinear refractive index coefficient, $I = 2n|E|^2/Z_0$ in MKS units, E is the electric field amplitude, and Z_0 is the characteristic impedance of free space. The intensity-dependent refractive index then modifies the beam's trajectory. This cascaded process is equivalent to a virtual lens, that focuses the beam. The self-focusing continues until a point where the intensity is so large (due to the shrinking spot size) that optical damage occurs. If this nonlinear focusing is balanced by the beam's (nominal) diffraction, then a self-guiding beam known as a spatial soliton [76] is created. Such an entity can

propagate through the medium without changing its (transverse) spatial profile. Figure 4.10 shows each of the three cases.

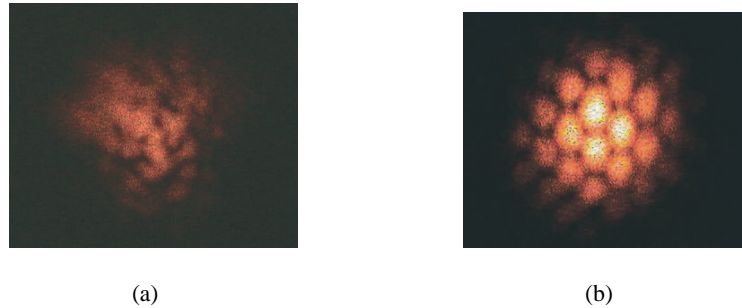


Figure 4.11: (a) Filamentation and (b) structured breakup of the beam due to SPM.

If there are fluctuations on the gaussian profile, these fluctuations can grow and eventually break the beam into multiple filaments as shown in Fig. 4.11(a). This other commonly seen manifestation is called filamentation [77]. Figure 4.11(b) shows that structured patterns [78] can also be formed given the right conditions. Filamentation is usually the effect scientists try to suppress while solitons are being sought. In the time domain, temporal solitons [79] are also due to SPM, which causes spectral broadening or pulse compression, balances group velocity dispersion instead of diffraction to create a pulse whose temporal profile is unchange upon propagation. Temporal solitons have been employed in commercial telecommunication systems to extend the distance between repeaters, thereby reducing the total cost of the network.

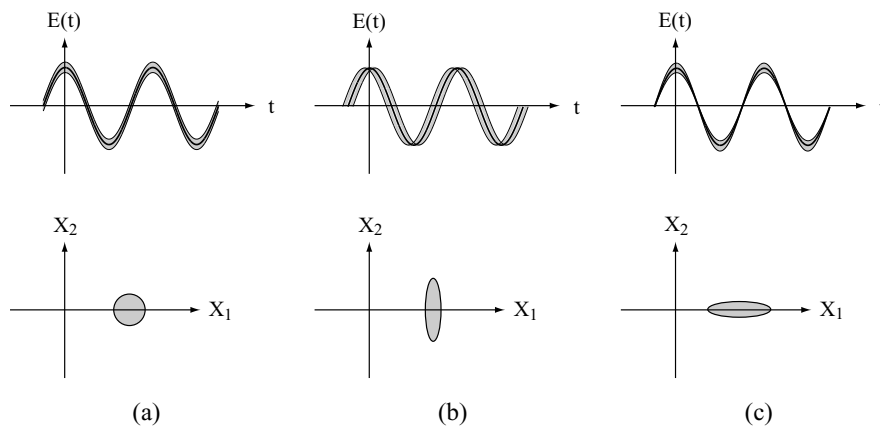


Figure 4.12: (a) Coherent, (b) amplitude squeezed, and (c) phase squeezed light. The phase-space representations are shown in the lower half.

A lesser known application of SPM is in the generation of squeezed light [80]. Squeezed light is a quantum field that has less noise than the fundamental limit (shot noise) in one quadrature at the expense of the other. Figure 4.12 shows the amplitude, phase and the phase-space representation of coherent, amplitude-squeezed, and phase-squeezed light. This property of squeezed light is useful for noise sensitive applications like in the measurement of gravitational waves.

4.4.2 Slow light

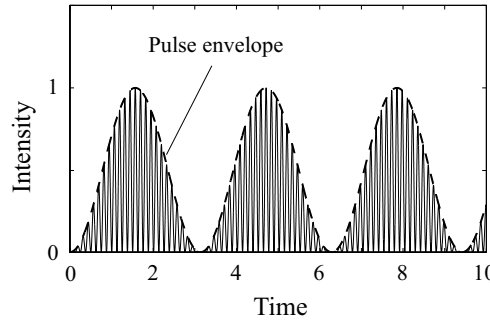


Figure 4.13: The pulse envelope travels at the group velocity.

All materials exhibit chromatic dispersion to some extent. Chromatic dispersion is defined as the index of refractive having a frequency dependence. A pulse of light propagating in the medium can be characterized by the mode-propagation constant, defined as

$$\beta = \frac{\omega}{c}n(\omega). \quad (4.4)$$

Equation 4.4 can be expanded in a Taylor series while the refractive index is approximated with the Sellmeier equation [79]. This gives the relation between β and n where

$$\beta_1 = \frac{1}{c} \left(n + \omega \frac{dn}{d\omega} \right) = \frac{n_g}{c} = \frac{1}{v_g}, \quad (4.5)$$

$$\beta_2 \simeq \frac{\omega}{c} \frac{d^2n}{d\omega^2} \simeq \frac{\lambda^3}{2\pi c^2} \frac{d^2n}{d\lambda^2}, \quad (4.6)$$

where β_1 is the inverse of the group velocity v_g , n_g is the group index, and β_2 is the group velocity dispersion. A pulse of light is composed of a spread of frequencies and the pulse envelope (see Fig. 4.13) travels at the group velocity while each individual wave travels at a different phase velocity ($\frac{c}{n}$).

Since the group velocity depends on the amount of chromatic dispersion of the refractive index, i.e. the slope of n , a rapidly changing n (with respect to frequency) will result in a larger group index and subsequently the generation of slow light¹. This rapidly changing refractive index is accompanied by a narrow gain or transparency feature. Slow light can be generated by either coherent population trapping or electromagnetically induced transparency, or coherent population oscillation [59, 81].

4.4.3 Bichromatic field in a two-level atom

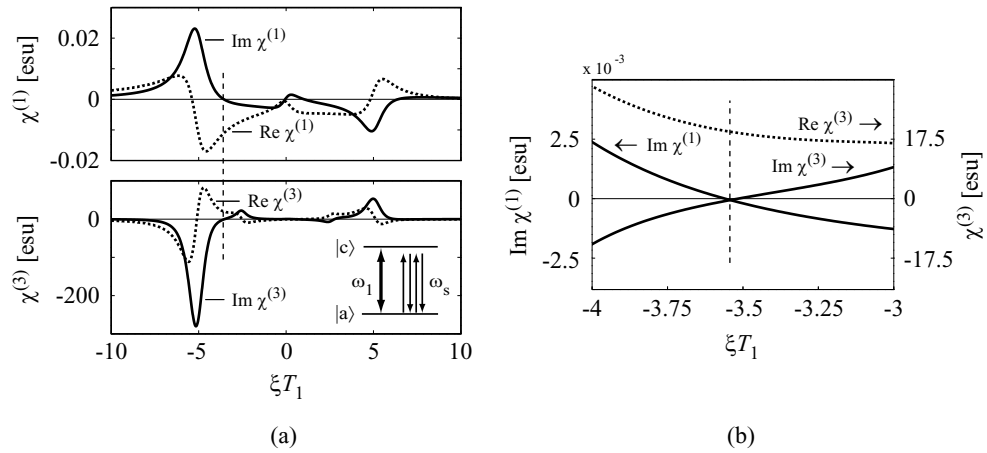


Figure 4.14: (a) Linear $\chi^{(1)}$ and nonlinear $\chi^{(3)}$ responses of a radiatively-broadened, bichromatic two-level system as a function of the normalized pump-probe detuning ζT_1 . (b) Expanded view around the detuning where there is no absorption of the probe field and the SPM coefficient is large.

Although EIT has mainly been studied in three level systems, it can still be realized in the two-level system [82] by applying both fields to the same transition. The first-order (linear) probe absorption spectrum is the Mollow absorption spectrum as described in Section 2.2 and shown in the upper half of Fig. 4.14(a) with $\Delta_1 T_1 = 1$ and $\Omega_1 T_1 = 5$. The difference in the amplitude between the absorption peak and the gain peak is attributed to the pump field's one-photon detuning.

There are conditions where a relatively large SPM, which is proportional to $\text{Re } \chi^{(3)}$, is present while the linear absorption vanishes for the probe field [83], as shown in Fig. 4.14(b). The features

¹Although slow light is not a self-induced multi-photon effect like SPM, the narrow absorption feature do not occur naturally but induced by another field.

of the Mollow absorption spectrum shifts with changing intensities of the pump field. This causes the transparency point to shift as well. An inherent disadvantage of EIT in a two-level system is that there is absorption of the pump field. Therefore, as the Rabi frequency of the pump field is reduced with propagation, the transparency window shifts and the result is a loss of transparency for the probe field. Another consequence is substantial population in the excited state producing spontaneous emission noise. This system is therefore not suitable for noise-sensitive applications such as squeezed light generation through SPM.

4.4.4 Dark state - electromagnetically induced transparency

EIT in a two-level system can produce a large SPM nonlinearity without absorption for the probe field. However, it suffers from an intensity dependent shift of the transparency window and from spontaneous emission noise. CPT in a Λ system has no absorption for all fields and no transparency window shifts but unfortunately, also no nonlinear response for the preparation fields. By combining EIT in the two-level system and the dark state in the Λ system, the benefits of each system can be obtained while eliminating their limitations [20]. Such a system possess a large self phase modulation (SPM) nonlinearity without linear or nonlinear absorption, and spontaneous emission noise. Such a system can also be used for spatial soliton propagation and manipulation.

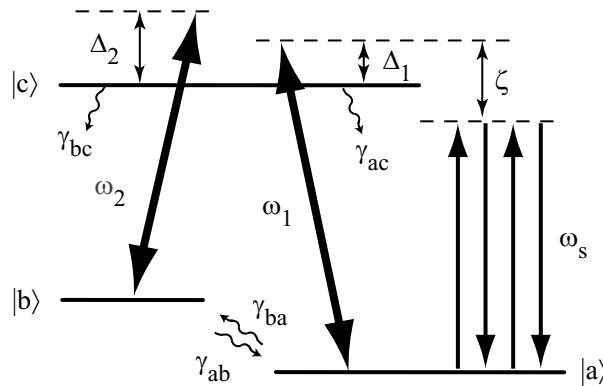


Figure 4.15: Energy level structure of the DS-EIT system.

Fig. 4.15 shows the dark state - electromagnetically induced transparency (DS-EIT) system. The two independent pump fields create the dark state (with the two hyperfine ground levels of the $D1$ line of sodium) and a third probe field interacts with the coherently prepared system.

A closed three-level Λ system with two applied fields is considered. The fields have the form $\tilde{E}(t) = E_t e^{-i\omega_t t} + E_2 e^{-i\omega_2 t} + c.c.$, each coupling to a lower level, with corresponding Rabi frequencies $\Omega_2 = 2\mu_{cb}E_2/\hbar$ and $\Omega_t = 2\mu_{ca}E_t/\hbar$. Detunings of these fields with respect to the upper bare atomic level $|c\rangle$ are $\Delta_2 = \omega_2 - \omega_{cb}$ and $\Delta_t = \omega_t - \omega_{ca}$. The E_t field comprised of a carrier (pump) E_1 and a modulation (probe) E_s field in the form:

$$E_t(t)e^{-i\omega_t t} = E_1 e^{-i\omega_1 t} + E_s e^{-i\omega_s t} \quad (4.7)$$

$$= \left(E_1 + E_s \exp^{-i\zeta t} \right) \exp^{-i\omega_1 t}, \quad (4.8)$$

and Δ_t becomes Δ_1 . The population decay rates γ_{ac} and γ_{bc} are from level $|c\rangle$ to the lower levels $|a\rangle$ and $|b\rangle$ respectively. γ_{ba} and γ_{ab} are the population exchange rates from levels $|a\rangle$ to $|b\rangle$ and $|b\rangle$ to $|a\rangle$ respectively. The coherence dephasing rates (from Eq. A.3) are:

$$\Gamma_{cb} = \frac{\gamma_{bc} + \gamma_{ac} + \gamma_{ab}}{2}, \quad (4.9a)$$

$$\Gamma_{ca} = \frac{\gamma_{ac} + \gamma_{bc} + \gamma_{ba}}{2}, \quad (4.9b)$$

$$\Gamma_{ba} = \frac{\gamma_{ba} + \gamma_{ab}}{2}. \quad (4.9c)$$

The quantity $\rho_{ij} = \sigma_{ij} \mu_{ij} e^{-i\omega_{ij} t}$ is the dipole moment expectation value for $i \neq j$ and the population for $i = j$. The atomic response can be calculated from the density matrix equations of motion as shown in Appendix A. The explicit form of these equations is shown in Appendix D.1. In the matrix formulation,

$$R \equiv \left[\rho_{aa}, \rho_{bb}, \rho_{cb}, \rho_{ca}, \rho_{ba}, \rho_{bc}, \rho_{ac}, \rho_{ab} \right]^T, \quad (4.10)$$

and S in Eq. A.7 is a constant vector. Since there is a bichromatic field on one of the transition, the matrix formulation of these equations are solved with a perturbative (in field strength) Floquet harmonic expansion as outlined in Appendix B. The linear susceptibility of the probe field can be obtained from the fourth element of the R_1 vector ($\rho_{ca}^{(1)}$) and the nonlinear susceptibility (for self-phase modulation) from the fourth element of the H_1 vector ($\rho_{ca}^{(3)}$). The total susceptibilities of the pump fields E_2 and E_1 can be obtained from the third ($\rho_{cb}^{(0)}$) and fourth element ($\rho_{ca}^{(0)}$) of the R_0 vector respectively. The population in the lower levels $|a\rangle$ and $|b\rangle$ are from the first and second elements of the R_0 vector (ρ_{aa} and ρ_{bb}) respectively and using Eq. A.6, the population in the excited level can be calculated. The MS version of the Matlab (computer) code described in Appendix E is used to perform the numerical simulation with the three-level Λ system chosen.

3-level Λ system dressed state picture

An analytical result can be obtained using dressed states. The transition between the lower levels are assumed to be electric dipole forbidden. The Hamiltonian for the Λ system is:

$$\hat{H} = \hat{H}_o + \hat{H}_{int}, \quad (4.11)$$

where

$$\hat{H}_o = \hat{H}_{at} + \hat{H}_{f1} + \hat{H}_{f2}, \quad (4.12)$$

$$\hat{H}_{int} = -\hat{r}[\hat{E}_1(0) + \hat{E}_2(0)], \quad (4.13)$$

\hat{H}_{at} is the atomic Hamiltonian, \hat{H}_{f1} is the Hamiltonian of pump field 1, and \hat{H}_{f2} is the Hamiltonian of pump field 2.

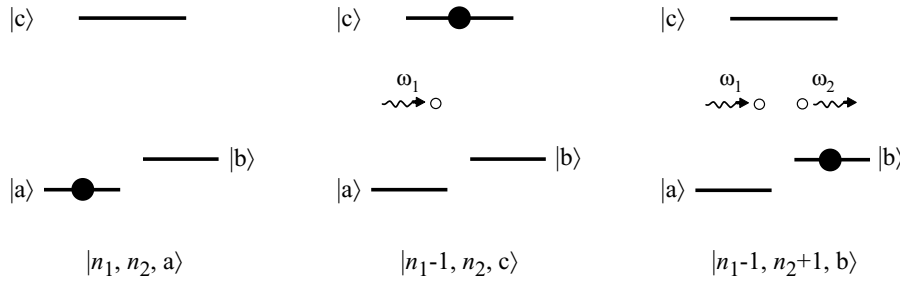


Figure 4.16: Degenerate atom-field states of the Λ system, with absorption of the ω_1 photon and emission of the ω_2 photon. The location of the sphere denotes which atomic energy level the electron is occupying.

The atom-field degenerate states (Fig. 4.16) are: $|n_1, n_2, a\rangle$, $|n_1-1, n_2, c\rangle$, and $|n_1-1, n_2+1, b\rangle$, where n_1 (n_2) is the number of photons in mode ω_1 (ω_2). The Hamiltonian can then be written as

$$\hat{H} = \begin{bmatrix} (n_1 - 1)\hbar\omega_1 + (n_2 + 1)\hbar\omega_2 + E_b & \frac{i}{2}\hbar\Omega_2 & 0 \\ -\frac{i}{2}\hbar\Omega_2 & (n_1 - 1)\hbar\omega_1 + n_2\hbar\omega_2 + E_c & -\frac{i}{2}\hbar\Omega_1 \\ 0 & \frac{i}{2}\hbar\Omega_1 & n_1\hbar\omega_1 + n_2\hbar\omega_2 + E_a \end{bmatrix}$$

$$= (n_1\hbar\omega_1 + n_2\hbar\omega_2 + E_a)\hat{I} + \hbar \begin{bmatrix} \Delta_1 - \Delta_2 & \frac{i}{2}\Omega_2 & 0 \\ -\frac{i}{2}\Omega_2 & \Delta_1 & -\frac{i}{2}\Omega_1 \\ 0 & \frac{i}{2}\Omega_1 & 0 \end{bmatrix}, \quad (4.14)$$

Evaluating the eigenvalues of the simplified matrix,

$$(\Delta_1 - \Delta_2 - \lambda)[(\Delta_1 - \lambda)(-\lambda) - (\frac{i}{2}\Omega_1)(-\frac{i}{2}\Omega_1)] - \frac{i}{2}\Omega_2[-\frac{i}{2}\Omega_2(-\lambda)] = 0, \quad (4.15)$$

$$(\Delta_1 - \Delta_2 - \lambda)[\lambda^2 - \Delta_1\lambda - \frac{|\Omega_1|^2}{4}] + \frac{|\Omega_2|^2}{4}\lambda = 0, \quad (4.16)$$

$$\lambda^3 - (2\Delta_1 - \Delta_2)\lambda^2 - [\frac{|\Omega_1|^2}{4} - (\Delta_1 - \Delta_2)\Delta_1 + \frac{|\Omega_2|^2}{4}]\lambda + (\Delta_1 - \Delta_2)\frac{|\Omega_1|^2}{4} = 0. \quad (4.17)$$

The cubic equation 4.17 can be solved numerically, or analytically by assuming a two-photon-resonance condition $\Delta_1 = \Delta_2$ to obtain

$$\lambda^3 - \Delta_1\lambda^2 - [\frac{|\Omega_1|^2}{4} + \frac{|\Omega_2|^2}{4}]\lambda = 0. \quad (4.18)$$

The first solution is

$$\lambda(1) = 0. \quad (4.19)$$

Let

$$\Delta = \Delta_1, \quad (4.20)$$

$$\Omega^2 = |\Omega_1|^2 + |\Omega_2|^2, \quad (4.21)$$

and the second and third solutions are

$$\lambda^2 - \Delta\lambda - \frac{\Omega^2}{4} = 0, \quad (4.22)$$

$$\lambda(2, 3) = \frac{\Delta \pm \sqrt{\Delta^2 + \Omega^2}}{2}, \quad (4.23)$$

$$= \frac{1}{2}\Delta \pm \frac{1}{2}\sqrt{\Delta^2 + \Omega^2}. \quad (4.24)$$

The triplet levels can then be calculated to obtain

$$E^0 = n_1\hbar\omega_1 + n_2\hbar\omega_2 + E_a, \quad (4.25)$$

$$E^\pm = n_1\hbar\omega_1 + n_2\hbar\omega_2 + E_a + \frac{\hbar}{2}\Delta \pm \frac{\hbar}{2}\sqrt{\Delta^2 + \Omega^2}, \quad (4.26)$$

with the corresponding eigenvectors

$$|n_1, n_2, 0\rangle = \cos \alpha |n_1, n_2, a\rangle + \sin \alpha |n_1 - 1, n_2 + 1, b\rangle, \quad (4.27)$$

$$\begin{aligned} |n_1, n_2, +\rangle &= i \sin \alpha \sin \theta |n_1, n_2, a\rangle - i \cos \alpha \sin \theta |n_1 - 1, n_2 + 1, b\rangle \\ &\quad + \cos \theta |n_1 - 1, n_2, c\rangle, \end{aligned} \quad (4.28)$$

$$\begin{aligned} |n_1, n_2, -\rangle &= -i \sin \alpha \sin \theta |n_1, n_2, a\rangle + i \cos \alpha \cos \theta |n_1 - 1, n_2 + 1, b\rangle \\ &\quad + \sin \theta |n_1 - 1, n_2, c\rangle, \end{aligned} \quad (4.29)$$

where

$$\tan 2\theta = \frac{\sqrt{\Omega_1^2 + \Omega_2^2}}{\Delta_1}, \quad (4.30)$$

$$\tan \alpha = \frac{\Omega_1}{\Omega_2}. \quad (4.31)$$

Since there is no state $|c\rangle$ in $|n_1, n_2, 0\rangle$, the latter is known as a “dark-state”. Together with the initial assumption of no transitions between the lower levels, and in the two-photon-resonance condition, this is a perfect² “dark-state”. The (sideband) resonances as seen by the probe field on the $|a\rangle \rightarrow |c\rangle$ transition with respect to ω_1 (ζ) are:

$$\Delta_{++} = 0, \quad (4.32)$$

$$\Delta_{0+} = -\frac{1}{2}\Delta_1 - \frac{1}{2}\sqrt{\Delta_1^2 + \Omega_1^2 + \Omega_2^2}, \quad (4.33)$$

$$\Delta_{-+} = -\frac{1}{2}\sqrt{\Delta_1^2 + \Omega_1^2 + \Omega_2^2}, \quad (4.34)$$

$$\Delta_{+0} = \frac{1}{2}\Delta_1 + \frac{1}{2}\sqrt{\Delta_1^2 + \Omega_1^2 + \Omega_2^2}, \quad (4.35)$$

$$\Delta_{00} = 0, \quad (4.36)$$

$$\Delta_{-0} = \frac{1}{2}\Delta_1 - \frac{1}{2}\sqrt{\Delta_1^2 + \Omega_1^2 + \Omega_2^2}, \quad (4.37)$$

$$\Delta_{+-} = \frac{1}{2}\sqrt{\Delta_1^2 + \Omega_1^2 + \Omega_2^2}, \quad (4.38)$$

$$\Delta_{0-} = -\frac{1}{2}\Delta_1 + \frac{1}{2}\sqrt{\Delta_1^2 + \Omega_1^2 + \Omega_2^2}, \quad (4.39)$$

$$\Delta_{--} = 0. \quad (4.40)$$

$$(4.41)$$

²There is no decay of the dark state, and the absorption spectrum has a delta function linewidth with complete transparency.

Results

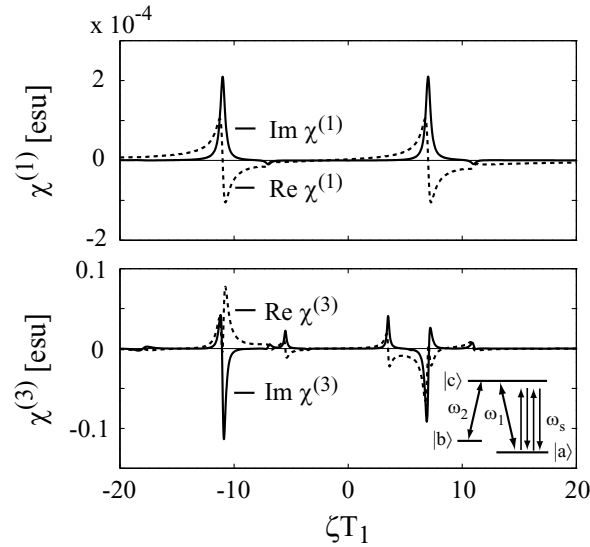


Figure 4.17: Linear and nonlinear susceptibilities of the homogeneously broadened DS-EIT system.

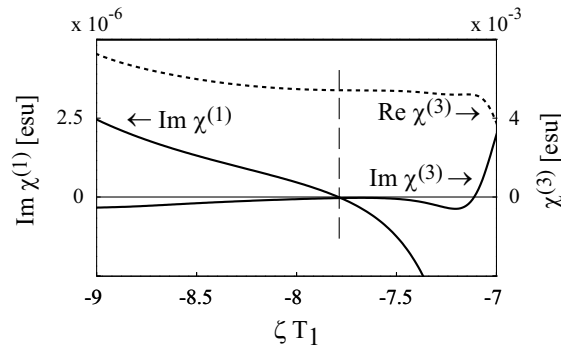


Figure 4.18: Large SPM in the absence of linear and nonlinear absorption of the Doppler-broadened DS-EIT system.

A set of field parameters can be found such that the SPM term is still large while both the linear and third-order nonlinear absorption are negligibly small (Fig. 4.17). There is also neither appreciable absorption of the pump fields nor appreciable population in the excited state. Thus, the transparency window, that is dependent on the Rabi frequencies, does not shift as the beams propagate. Doppler-broadening did not destroy this feature (Fig. 4.18).

4.5 Summary

In this chapter, a few nonlinear processes that occur in multi-level systems are introduced . Some of these processes can be enhanced by the quantum interference processes described in the previous section. Some might compete against them, resulting in a weaker signature of the quantum interference effect as will be shown in the next chapter.

5 Coherent Population Trapping in a Real Atom

5.1 Introduction

To better understand CPT and the atomic properties of sodium, pump-probe experiments were performed with a sodium vapor cell. The first experiment [84] involves probing the Doppler absorption spectrum of the sodium vapor with the frequency of the pump field held fixed. In the second experiment [85], both fields are scanned across the Doppler profile. It was mentioned in Chapter 2 that CPT can completely eliminate the response of the medium to the preparation fields. However, it was noted that CPT can still be utilized to enhance other processes. Experimental demonstrations [86] of this sort of enhancement are reported in this chapter.

5.2 Experimental Layout

Coherent CR699-21 continuous-wave (CW) dye lasers were used to provide the applied optical fields for the experiments. Rhodamine 590 tetrafluoroborate (530.38 mole), also known as R6G, dye was used to obtain a laser output frequency at the D lines of sodium. The absorption spectrum of Rhodamine 590 is shown in Fig. 5.1. This dye can be pumped by a variety of sources; the optimal pump source for operation around the $D1$ line of sodium is either an Argon-ion laser at 514 nm or a second-harmonic Nd-YAG laser at 532 nm. The solid state Spectra Physics Millennia series lasers were used. These CW pump lasers use internally diode-pumped neodymium-doped yttrium vanadate (Nd:YVO_4) crystals as the gain medium. The 1064 nm output is frequency-doubled with

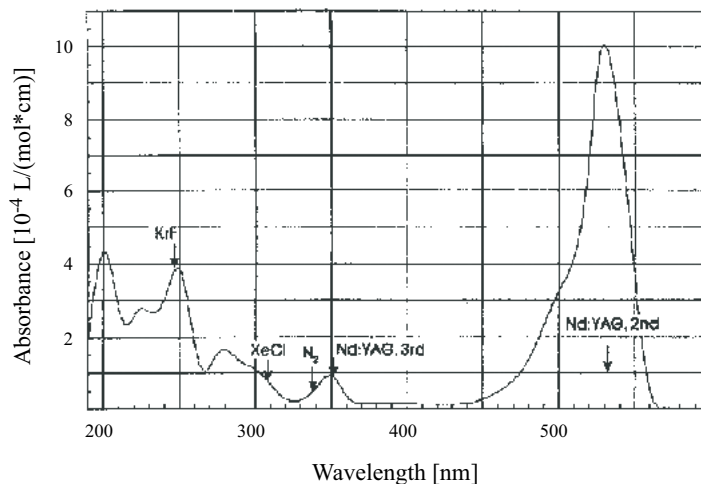


Figure 5.1: Absorption spectrum of Rhodamine 590 dye.

a temperature tuned lithium triborate (LBO) nonlinear crystal. The Millenia V is a 5W laser while the Millenia X is a 10W laser.

A Burleigh WA4500 wavemeter monitored the wavelengths of the fields. This wavemeter has a wavelength accuracy of 0.001 nm. Figure 5.2 shows the experimental layout drawn technically. The layout is fairly general and various components can be swapped out to perform the various experiments. The layouts for each experiment are drawn schematically in their respective sections. \odot (blue) indicates vertical polarization, and \leftrightarrow (red) indicates horizontal polarization. Note that the periscopes rotate the polarization of the output of the lasers from vertically polarized to horizontally polarized. The polarizing beam splitters (PBS) were used to combine and separate beams of orthogonal polarization while regular beam splitters (BS) were used if the polarization of the beams are identical. The halfwave ($\lambda/2$) plates were used to rotate the polarization of the beam. The spectra are detected with silicon photodiodes, or photomultiplier tubes, and monitored with an oscilloscope (OSC) or a spectrum analyzer (SA).

The Brimrose acousto-optic modulator (AOM), designed to operate at 590 nm, has a center frequency of 1772 MHz and is tunable (± 250 MHz). It was used to downshift the frequency of a part of the Laser 1 beam to ν_2 . This AOM is also capable of imposing an AM (50 MHz bandwidth) signal on the optical beam. The other AOM's are ISOMET 1205-C with a center frequency of 80 MHz driven by the D301B driver for frequency shifting (FS) or the 232A-1 driver for amplitude

modulation (AM). The frequency tuning range for the D301B is 60–100 MHz and the modulation bandwidth of the 232A-1 driver is 35 MHz. A part of the Laser 1 beam was double-passed through the FS ISOMET AOM to enable the frequency sweep of ν_1 .

A polarization maintaining optical fiber, designed to operate at 600 nm, was used to provide mode matching of the mutually-orthogonal, linearly polarized beams that were directed into the sodium cell. Unwanted birefringence that are caused by stress on the fiber will rotate the polarization of the beams in the fiber. Extra care was taken to prevent this rotation. A reflective diffraction grating (1500 lines/mm) was used after the cell to separate the frequency components (at the $D1$ and $D2$ lines) of the beam that have the same polarization.

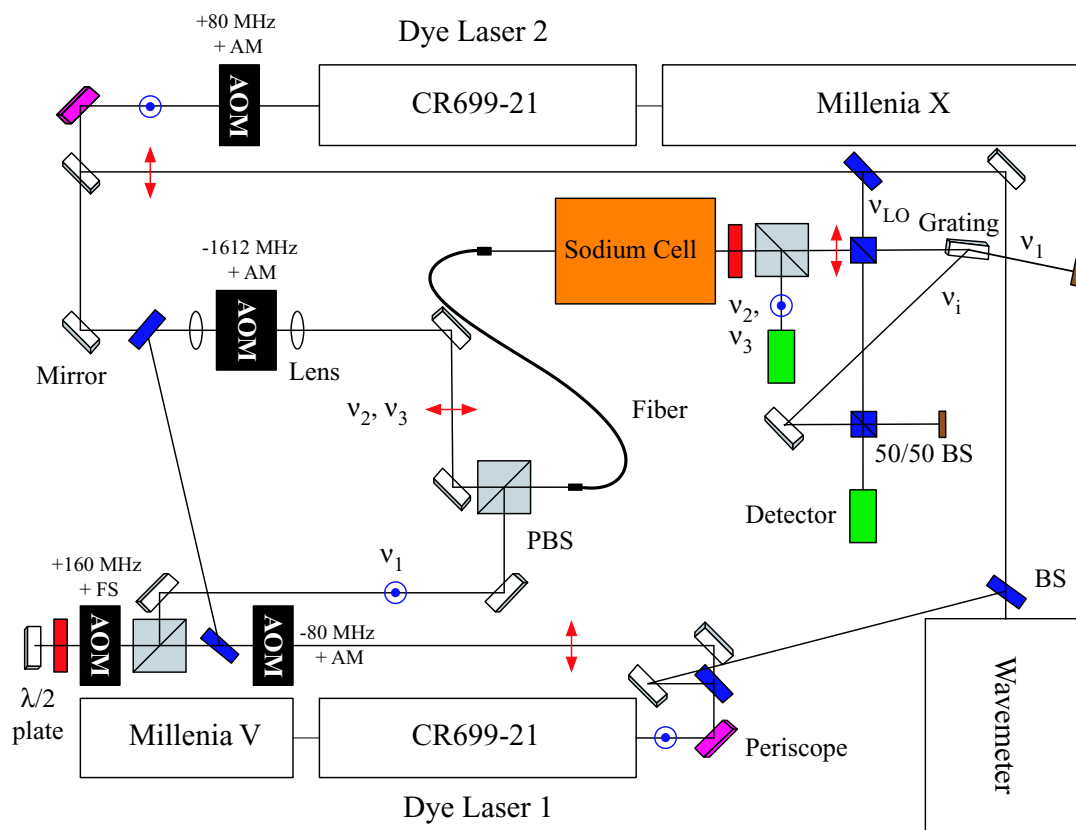


Figure 5.2: Technical drawing of the experimental layout. The components are color-coded to avoid cluttering with extra labels.

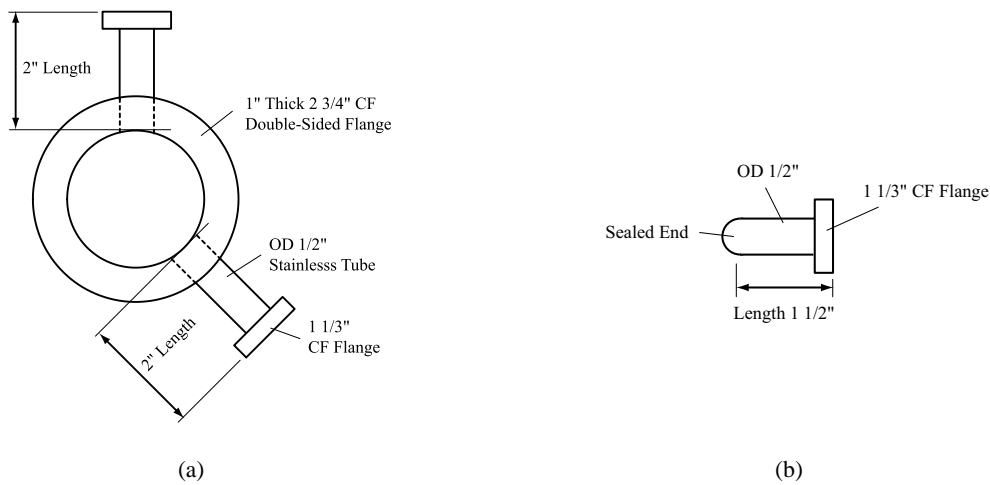


Figure 5.3: (a) Central flange and (b) cold finger of the vapor cell.

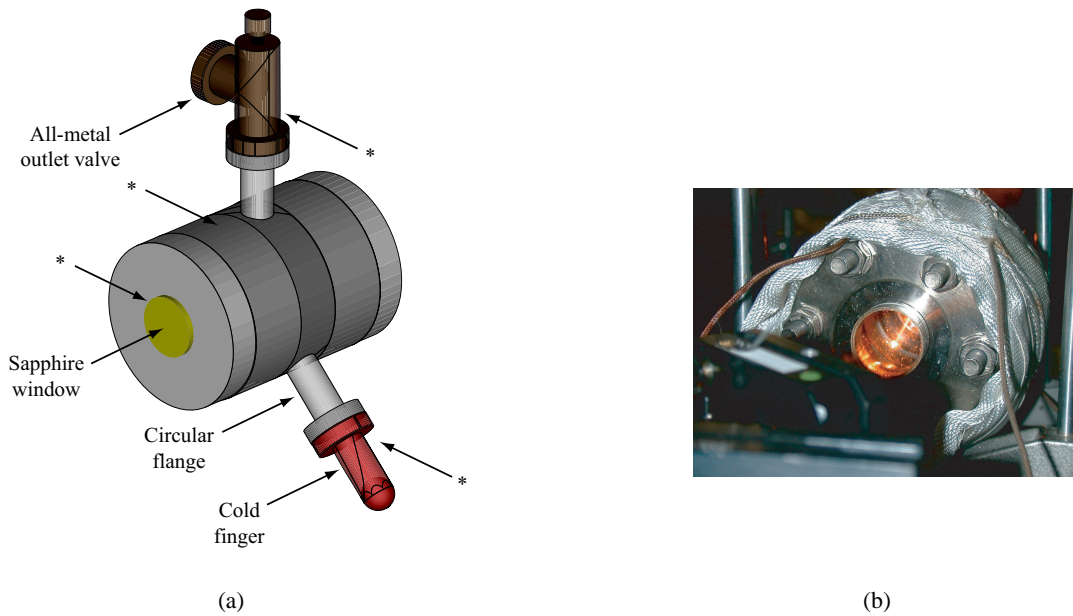


Figure 5.4: Sodium vapor cell used in the experiment. (i) Schematic drawing of the cell. * - Thermocouple wires are placed at these locations to measure the temperature. (ii) Fluorescence inside the cell.

5.2.1 Sodium vapor cell

A hot vapor cell was used for the experiments. The 7-cm-long vapor cell is made up of a stainless steel body with sapphire viewports and an all-metal outlet valve. These parts are required as they can withstand the corrosive nature of sodium and the heat from the heating tapes. A new flange [see

Fig. 5.3(a)] is designed such that the vapor cell has a short evacuation time without compromising the outlet valve that seals the cell. The solid pieces of sodium were placed in the cold finger, which was also designed and custom made [Fig. 5.3(b)]. Figure 5.4(a) shows the cell assembled from 2 3/4 in. OD circular ConFlat® (CF) flanges. Figure 5.4(b) shows the fluorescence of the sodium vapor with the excitation of the dye laser. The whole cell, comprised of the cold finger, cell body and outlet valve, was heated (max. 450°C) with electrical heating tapes and insulated, with the cold finger at a slightly lower temperature. This ensures that the sodium vapor will condensate back in the cold finger instead of condensing on the viewports. Type E thermocouple wires were placed at various locations of the cell as indicated by the asterisks in Fig.5.4(a) to measure the temperature. The conversion table for the thermocouple at ice-point is shown in Fig. 5.5. An offset equal to the room temperature needs to be added to the value obtained from the chart.

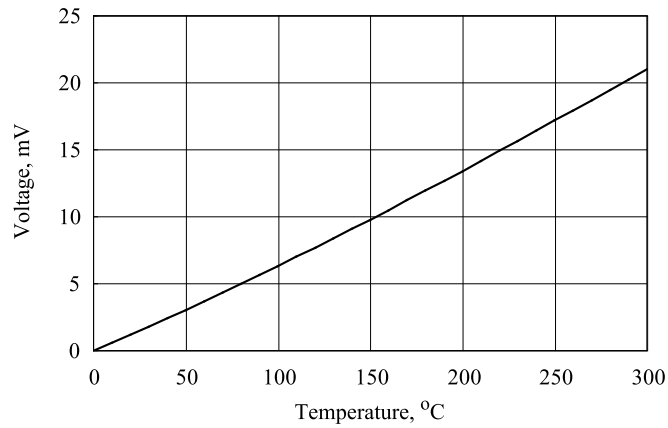


Figure 5.5: Conversion chart for Type E thermocouple wires at ice-point.

The number density of the sodium vapor is dependent on the temperature T (in degree Kelvin) of the cell which in turn governs the vapor pressure as given by [87]. The vapor pressure can be approximated by

$$p[\text{mmHg}] \cong \exp[-(a/T) + d], \quad (5.1)$$

where $a = 12423.3$ and $d = 17.3914$ for sodium. The number density is

$$N = \frac{p[\text{Pa}]}{k_B T} \text{ atoms / m}^3, \quad (5.2)$$

$$= 9.66084 \times 10^{18} \frac{p[\text{mmHg}]}{T} \text{ atoms / cm}^3. \quad (5.3)$$

Fig. 5.6 shows the vapor pressure versus temperature for atomic sodium. The curves of the monatomic and total (monatomic and diatomic) pressure overlaps almost completely in this temperature range, indicating that monatomic sodium is dominant.

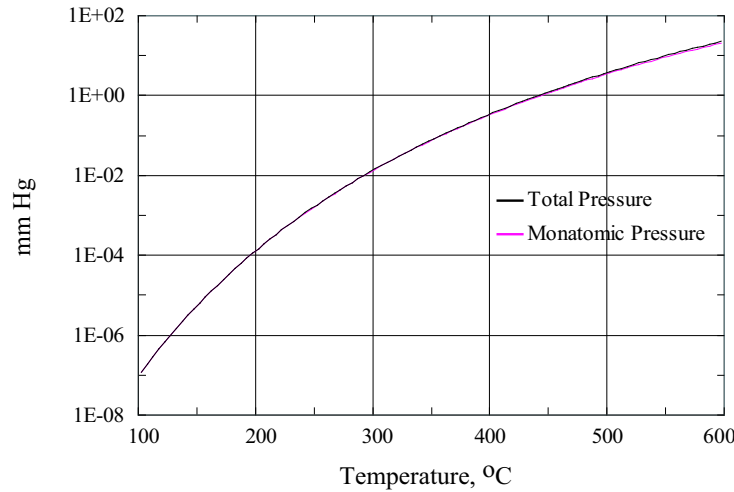


Figure 5.6: Vapor pressure versus temperature.

It is not possible to seal a temperature gauge, that is resistant to sodium, inside the cell. Therefore, the temperature of the outside of the cold finger was used to determine the number density of the sodium vapor. The value is fairly accurate once the cell has achieved local thermal equilibrium at the desired temperature.

Sapphire windows were used for the viewports of the cell since it can withstand the corrosion and the heat. However, sapphire is birefringent. The laser beam was not directed perpendicularly to the sapphire window but at a very small angle. This is to prevent the back-reflected beam from introducing an extra field into the process being studied, even if a standing-wave mode is not created. The optic axes of both of the sapphire windows are parallel to the surface of the window and positioned vertically. This causes the vertically polarized light (aligned to the optic axis) to become an extraordinary wave and the horizontally polarized light to be an ordinary wave. The incident light will not have its polarization rotated but this setup can be used only for linear orthogonally polarized light and not circularly polarized light. A slight but not overwhelming rotation still exists.

Fig. 5.7(a) shows the side view of the pumping station that was built which is capable of evacuating the vapor cell down to 10^{-7} torr. This is required to ensure there is no water vapor and other

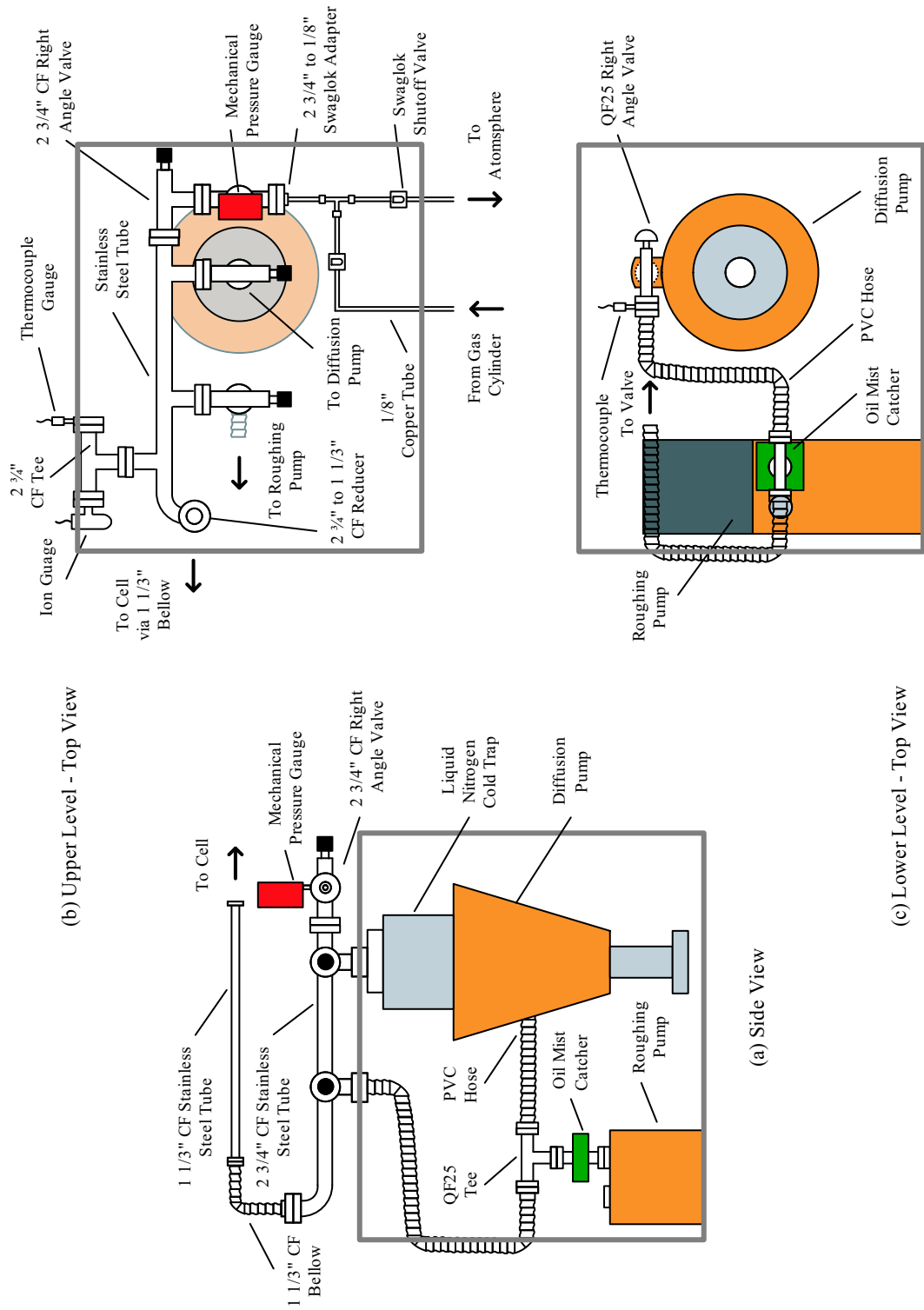


Figure 5.7: The vacuum pumping station.

contaminant inside the cell. The roughing pump was used to pump the system to low vacuum, at which point the diffusion pump takes over to pump the system down to high vacuum. The liquid nitrogen cold trap can be used to prevent back flow of pump oil into the vacuum system. The station was designed to allow buffer gas to be bled into the cell, see Fig. 5.7(b). A thermocouple and ion gauge pair was used to measure the pressure. The mechanical gauge was used to determine the amount of buffer gas when a high buffer gas density is required. A thermistor gauge was also used to verify the pressure readings. Buffer gas can be bled into the cell even when the cell is hot. However, evacuating the cell cannot be done until the cell is cooled to avoid having the sodium vapor escaping out of the cell and condensing on the tubing or in the pumps.

5.3 Thirteen Resonances of the Sodium $D1$ Line

5.3.1 Experiment

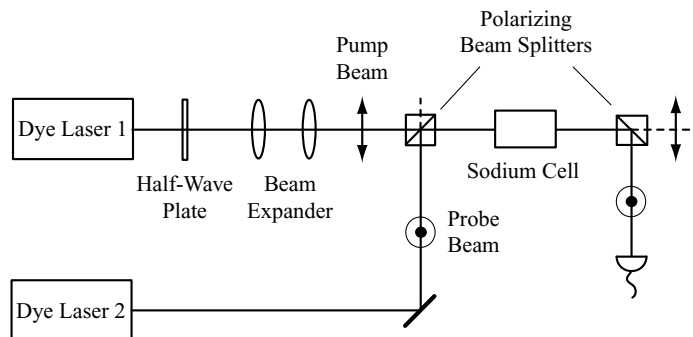


Figure 5.8: Schematic layout of the thirteen resonances experiment.

The study of the atomic properties of sodium was performed with a pump-probe experiment around the $D1$ line of sodium as depicted by Fig. 5.8. The fixed-frequency pump beam (ω_p) was obtained from a CW dye laser and a weaker frequency-scanned probe beam (ω_s) was produced by another identical dye laser. The pump and probe beams are collimated, co-propagating, collinear, and are linearly and orthogonally polarized. It was assumed that the diffusion time of sodium atoms across the path of the laser beam is the dominant contributor of the dephasing rate of the ground state coherence. As the atoms (which are pumped into the dark state) propagates out of the laser path and collide with the walls of the sodium cell, they dephase. When these atoms return to the

laser path, since they are no longer in the dark state, these atoms need to be re-prepared. These transit time effects¹ are reduced through the use of a spot size of the pump beam larger than that of the probe. This larger spot size was achieved by passing the pump beam through a telescopic beam expander. The vapor cell was pumped down to 10^{-7} torr and no buffer gas was introduced. The cell was then heated to 152°C creating a number density of 1.6×10^{11} atoms/cm³ with a minimum transmittance of 25% for the probe beam in the absence of the pump beam. After passing through the cell, the probe beam was separated from the pump beam by a polarizing beamsplitter and fed to a photodiode.

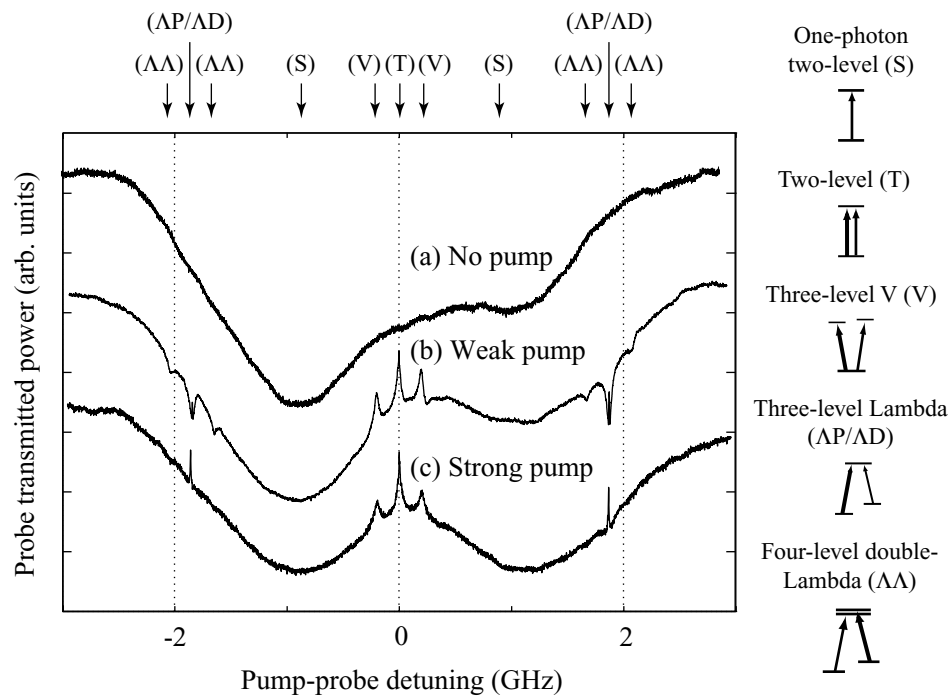


Figure 5.9: Probe transmission versus pump-probe detuning for various pump intensities. The types of resonances are labelled on the top and the subsystems where the resonances occur in are shown on the right.

Curve (a) of Fig. 5.9 shows the experimental probe beam transmission spectrum in the absence of the pump beam and is included as a reference. Curve (b) is the probe transmission for comparable

¹Transit time effects can be included as an incoherent dephasing contribution to the Raman transition.

pump (9.7 mW/cm^2) and probe intensities (1.3 mW/cm^2). Curve (c) is the probe transmission in the presence of a strongly saturating pump field (525 mW/cm^2). The curves are displaced vertically for clarity. Each of the resonances can be explained in terms of a simplified level structure denoted by the symbols at the top, and the subsystems in which the processes occur are shown on the right-side of Fig. 5.9.

The sodium $D1$ line (589 nm) is comprised of transitions from either of the two hyperfine ground levels (1772 MHz apart) to either of the two hyperfine excited levels (189 MHz apart) as shown in Fig. 3.2. The pump field is tuned to connect the mid-point of the lower levels to the mid-point of the upper levels while the frequency of the probe field is swept across the Doppler profile. The $D1$ line is Doppler-broadened and is not a pure two-level system, thus the saturation intensity is larger than that for a simple two-level transition (6 mW/cm^{-2} for sodium).

The two broad transmission dips (labelled S) 1772 MHz apart result from the single-photon Doppler-broadened transitions between the hyperfine ground levels and the excited levels. These dips have a full-width-half-maximum (FWHM) linewidth of 1500 MHz. The hyperfine excited levels, however, cannot be resolved with a single field because of Doppler broadening. The central transmission peak (T) is a consequence of forward degenerate four-wave-mixing (FDFWM) and saturation in a two-level subsystem. The inner pair of spectral features (V) is a result of difference frequency crossing (DFC) resonance and non-degenerate four-wave mixing (NDFWM) in a V subsystem. The outer pair of transmission peaks (ΔP), which is most visible in curve (c) of Fig. 5.9, results from coherent population trapping (CPT) in a Λ subsystem. The broader transmission dip (ΔD) and the pair of satellite dips ($\Delta\Delta$) around the CPT peak in curve (b) are due to optical pumping in the Λ and double- Λ system respectively.

Because of Doppler broadening of the transition frequency, both the pump and probe fields can excite all of the optical transitions in the four-level hyperfine structure. Consequently, each feature except the central peak appears twice, once on either side of the pump frequency. For a given applied field intensity and frequency, the Rabi frequency (due to different dipole strength [87, 88]) and the detuning of that field is slightly different for each transition. On the other hand, the particular geometry of the experiment resulted in an almost complete cancellation of Doppler broadening for the multi-photon transitions. Residual Doppler broadening need only be taken into account when the width of the resonance is very narrow. In each particular configuration for each of the resonances,

phase matching is partially achieved as described in Section 4.3.

Two intensity regimes were studied in the experiment. When the pump field is only weakly saturating, all thirteen resonances are visible. If the pump intensity is much larger than that of the probe field, many of the features wash out and conventional optical pumping² is significant, which effectively reduces population in the subsystem under analysis. Within each intensity regime, power-broadening did not modify the features significantly.

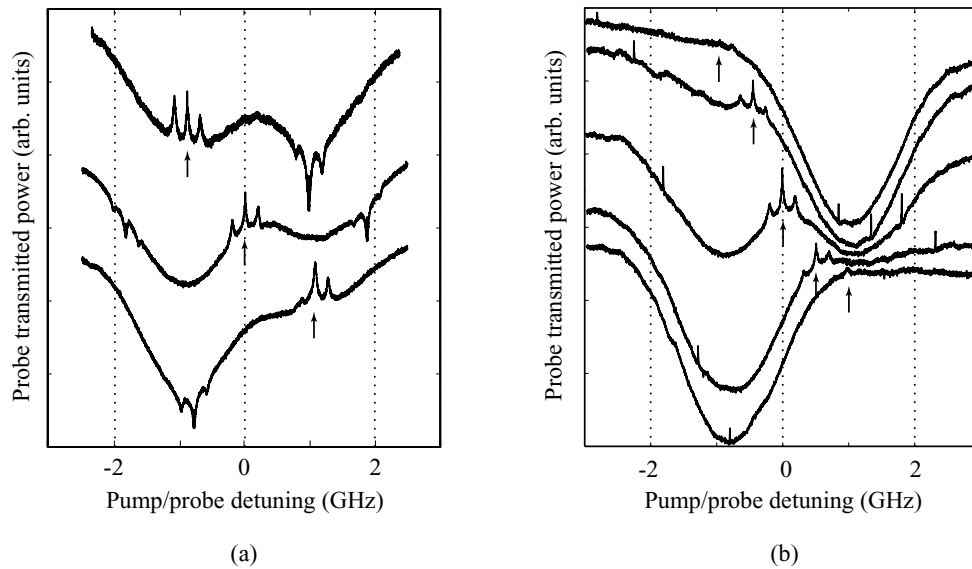


Figure 5.10: Probe transmission versus pump/probe detuning for various pump detunings with a (a) weakly saturating and (b) strongly saturating pump field. The arrow designates the pump frequency in each case.

As the pump frequency is tuned across the Doppler profile, conventional optical pumping which transfers population from one ground level to the other is evident from the top to the bottom spectra of Fig. 5.10(a) and Fig. 5.10(b). When the pump field is tuned closer to one of the V (or double- Λ) subsystems, the contributions to the red-detuned and the blue-detuned peaks (dips) are different. The robustness of the CPT signal is clearly seen as the peak still persists even in the wings of the Doppler profile. The best condition for observing the two-level and V subsystem resonances occurs when the pump field is tuned between the two hyperfine ground levels (middle spectra of Fig. 5.10).

²See Section 4.2.2.

5.3.2 Theoretical four-level model

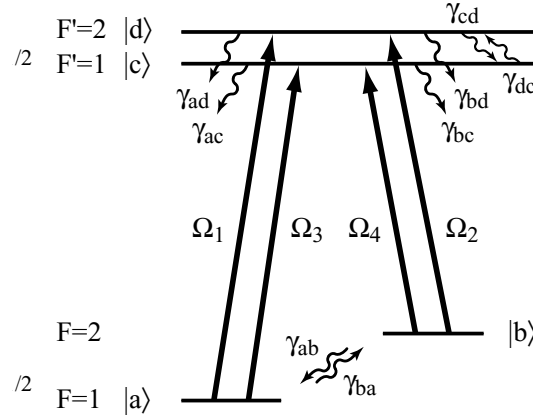


Figure 5.11: Energy level diagram of the four-level model.

The hyperfine structure of sodium was modelled with the four-level system shown in Fig. 5.11 to interpret the experimental results. The interaction Hamiltonian (\tilde{V}) is comprised of four pairs (pump \tilde{E}_p and probe \tilde{E}_s) of fields corresponding to each of the four transitions, and is represented by

$$\tilde{V}_{da} = \hbar\tilde{\Omega}_1 = -\mu_{da}\tilde{\mathcal{E}}, \quad (5.4a)$$

$$\tilde{V}_{db} = \hbar\tilde{\Omega}_2 = -\mu_{db}\tilde{\mathcal{E}}, \quad (5.4b)$$

$$\tilde{V}_{ca} = \hbar\tilde{\Omega}_3 = -\mu_{ca}\tilde{\mathcal{E}}, \quad (5.4c)$$

$$\tilde{V}_{cb} = \hbar\tilde{\Omega}_4 = -\mu_{cb}\tilde{\mathcal{E}}, \quad (5.4d)$$

where $\tilde{\mathcal{E}}$ is defined in Eq. B.1. The decay rates between hyperfine excited levels (γ_{cd} and γ_{dc}) and between hyperfine ground levels (γ_{ab} and γ_{ba}) are nonradiative and much smaller than the spontaneous emission rates of the optical transitions (γ_{ad} , γ_{bd} , γ_{ac} , and γ_{bc}). Consistent with the experimental condition of low sodium density and no buffer gas, collisional broadening ($\Gamma_{nm}^{\text{coll}}$) is ignored in the theoretical model. The equations of motion are defined in Appendix D.2 and solved with a Floquet expansion as outlined in Appendices A and B. The rotating frame transformation is performed with the frequency of the pump field at each transition. The atomic response of the probe field is calculated to first order while the response of the pump field is calculated exactly. The density matrix element obtained for a single atom is averaged over a Maxwellian profile to take

Doppler broadening into account. The MS version of the Matlab code (Appendix E) was used for the numerical simulation. The responses of each subsystem are computed separately by choosing the appropriate option.

Each hyperfine level consists of multiple Zeeman magnetic sublevels. Since stray magnetic fields are negligible under the present experimental conditions, these sublevels are nearly degenerate. A brief discussion on the effects of stray magnetic fields is presented in Section 5.3.4. By using orthogonal linear polarizations for the fields, the effect of optical pumping into uncoupled Zeeman sublevels is minimized [88]. Therefore, Zeeman sublevels are ignored in the model. Pump depletion effects and intensity variations across the beams are also neglected in the present theoretical analysis. The other parameters used in the numerical simulation correspond to those of the experimental setup.

Each resonance will now be described using a simplified elementary-system model and the numerical spectra are compared with the experimental ones.

5.3.3 Elementary system analysis

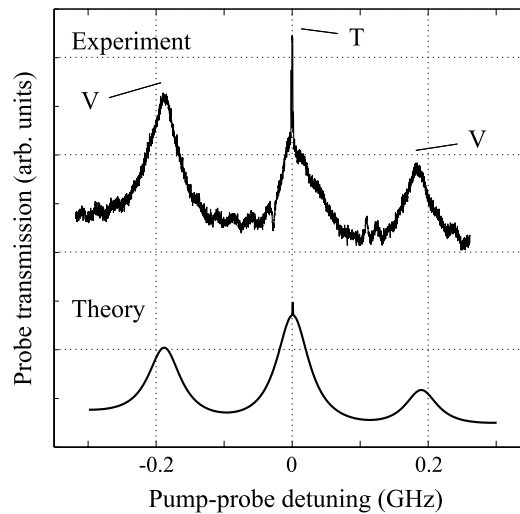


Figure 5.12: Resonances associated with the two-level and three-level V subsystems for the case of comparable pump and probe intensities.

The central degenerate transmission peak labelled T in Fig. 5.12 consists of two features: a 2 MHz FWHM sub-natural-linewidth peak superposed on a broader 45 MHz wide feature. The

narrower peak can be understood as a FDFWM process in an open two-level subsystem as depicted in Fig. 4.7. An idler photon is generated with the absorption of two pump photons and the emission of one probe photon. The decay to the other hyperfine ground level $|b\rangle$ provides additional decay channels. The additional excited level decay is governed by spontaneous emission which is larger than that of the extraneous decay of the ground level. This satisfies the requirement for resonance narrowing ($\gamma_c > \gamma_a$). In Fig. 4.7, ω_1 and ω_3 are from the same pump field and ω_2 is from the probe field. In Fig. 5.11, the pump photons are taken from the pump portion of Ω_i and the probe from the probe portion of Ω_i , where i can be either 1, 2, 3 or 4.

The width of this feature is determined by thermal redistribution, the dephasing rate between the two lasers, residual Doppler broadening, and diffusion of atoms into and out of the interaction region. In the present experiment, transit time effects are the dominant contribution of this linewidth. The idler field is of the same polarization as the probe field and both fields are polarized orthogonally to the pump field. As such, the detector measures both the probe and idler fields.

The broader peak is a consequence of saturation: hole burning [see Fig. 4.1(a)] in a Doppler-broadened two-level medium. The width is power-broadened to a few times the radiative linewidth ($1/T_1$).

The pair of 45 MHz wide transmission peaks labelled V in Fig. 5.12, 189 MHz away from the central peak, occurs as a result of saturation (DFC) and four-wave mixing (NDFWM) in a V subsystem. This effect occurs when the frequency difference of the pump and probe fields matches the frequency separation of the excited levels.

The pump field saturates the $|a\rangle \rightarrow |d\rangle$ transition, depleting the ground level (ρ_{aa}) population as shown in Fig. 4.3(a). The probe field on the $|a\rangle \rightarrow |c\rangle$ transition experiences reduced absorption as a result. When the probe field is blue-detuned from the pump field (pump on the $|a\rangle \rightarrow |c\rangle$ transition, and probe on the $|a\rangle \rightarrow |d\rangle$ transition), the other absorption dip (at +189 MHz) is obtained. The linewidths of the DFC resonances power-broadened from their 20 MHz homogeneous width.

However, the process of DFC does not account completely for these transmission peaks. The experimental curve of Fig. 5.12 shows one of the V subsystem peaks being stronger than the (broad) saturation peak of the two-level subsystem. For each hyperfine ground level, the two-level saturation process can couple to two velocity subgroups of atoms, one for each transition to an excited

hyperfine level. The DFC process, however, is resonant with only one velocity subgroup. Therefore, the DFC peak will never be larger than the two-level saturation peak regardless of where the pump field is tuned.

NDFWM in the V subsystem accounts for the discrepancy. The idler field peaks when the pump-probe detuning matches the frequency separation of the excited levels (189 MHz) as shown in Fig. 4.8. As with the FDFWM case in the two-level subsystem, the detector measures both the probe and the idler fields. But unlike the FDFWM peak, there are no line narrowing effects and the width of the resonance is of the order of the homogeneous linewidth that power-broadens to a lesser extent than the DFC feature. The theoretical spectrum of Fig. 5.12 does not include the contributions from the idler fields of both the FDFWM and NDFWM processes although all the processes are involved in the numerical simulation. When the intensity of the pump is increased, the resonance due to DFC washes out partially leaving mainly the NDFWM contribution.

The most striking manifestation of EIT in a Λ system is the dark state created through CPT. Even though there are two close-lying excited levels in the hyperfine structure, it has been shown that the extra off-resonant level only slightly perturbs the CPT system and modifies only the phase of each field component [89]. By tuning to the center of gravity of the set of hyperfine levels that constitute the upper level of the Λ subsystem, CPT can be achieved just as in a pure three-level Λ system [90]. CPT has also been observed using circularly-polarized fields to couple particular Zeeman sublevels [91].

If the intensity of the pump field is comparable to that of the probe field, a 45 MHz wide broad absorption feature centered on the 2 MHz wide CPT transmission peak is present as shown in Fig. 5.13 [see also Fig. 4.2(b)]. When the pump intensity is increased, the broad transmission dip washes out. This dip has a similar origin as the resonance described below.

In Fig. 5.13, a pair of 45 MHz wide satellite transmission dips is symmetrically displaced by 189 MHz from the central CPT feature. These two transmission dips as well as the broad dip centered on the CPT feature are inverted DFC resonances caused by optical pumping in addition to saturation. For distinction, the satellite pair will be referred to as *cross-transition resonances*, which occur only in a double- Λ system. Unlike the usual double- Λ system analyses which include at least three fields, here there are only two and the transitions they couple to do not share a common initial or final level as illustrated in Fig. 4.4(a). From Fig. 4.4(b), the absorption peak obtained is with the pump field

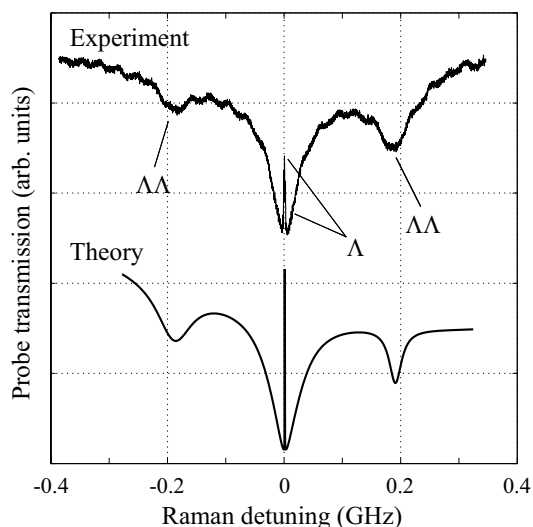


Figure 5.13: Resonances associated with the Λ and double- Λ subsystems for the case of comparable pump and probe intensities.

tuned to the $|a\rangle \rightarrow |d\rangle$ transition and the probe field to the $|b\rangle \rightarrow |c\rangle$ transition. The resonance is at the pump-probe detuning of the frequency difference between the two transitions, $-(1772 + 189)$ MHz. The other three cross-transition resonances are obtained in the same fashion as shown in Fig. 5.14.

Similarly to the DFC resonance, the width of the cross-transition resonance is also slightly power-broadened. Optical pumping lowers the saturation intensity [65] of the cross-transition resonances as well as the broad dip centered on the CPT feature. Therefore, these resonances wash out much more quickly than the NDFWM resonances in the V subsystem with increasing pump intensity, as can be seen in curve (c) of Fig. 5.9.

5.3.4 Discussion

Even weak magnetic fields can sometimes lead to subtle but important effects [92,93]. In the current experiment the influence of weak stray magnetic fields has been ignored up to this point, but it can manifest itself in two ways: (1) Optical pumping or other coherence effects between any of these Zeeman sublevels can modify the strength of the features; (2) The sub-natural-linewidth features are broadened.

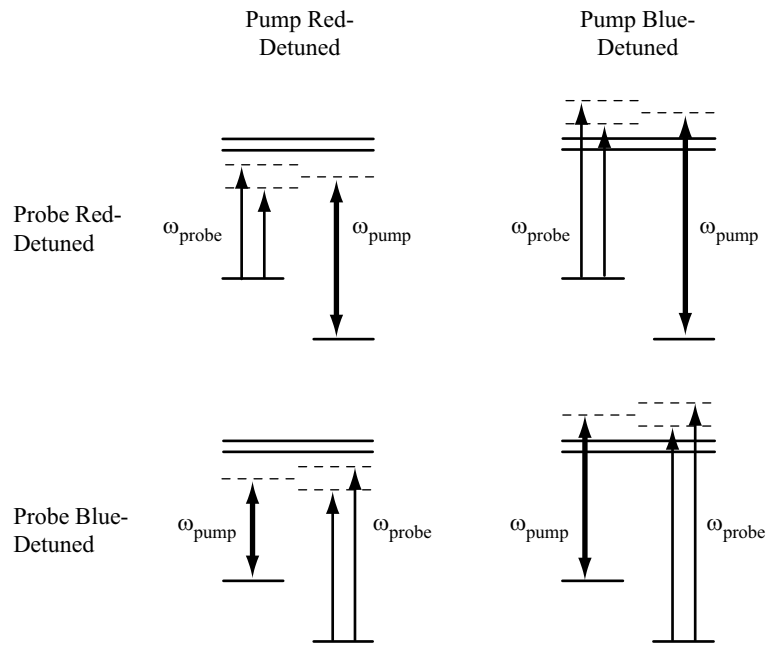


Figure 5.14: Energy level diagrams of the four cross-transition resonances.

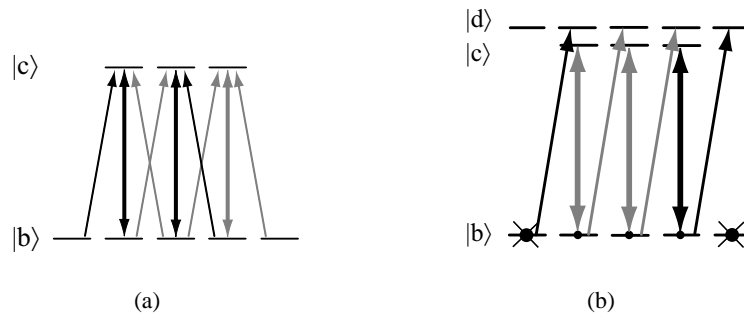


Figure 5.15: (a) Λ system between Zeeman sublevels. (b) Optical pumping to extreme Zeeman sublevels.

A narrow resonance can be obtained from coherence between Zeeman sublevels in a degenerate two-level system as analyzed by Lezama, see Eq. 20 of [94]. Figure 5.15(a) shows dark states being formed between Zeeman sublevels in a Λ configuration within the same hyperfine level which can enhance the FDFWM peak. This contribution is not included in the theoretical spectrum of Fig. 5.12. On the other hand, when the pump field is connecting the $F = 2 \rightarrow F' = 1$ transition and the probe connecting the $F = 2 \rightarrow F' = 2$ transition as shown in Fig. 5.15(b), residual absorption can occur because of optical pumping effects into the extreme Zeeman sublevels ($m_F = \pm 2$) that do not form

a V subsystem. Stray magnetic fields will broaden the sub-natural-linewidth features of FDFWM and CPT (experimental curve of Figs. 5.12 and 5.13) because the Zeeman sublevels are not exactly degenerate anymore. Background absorption countering CPT occurs when the fields are coupled in an off-Raman-resonance manner as shown in Fig. 5.16.

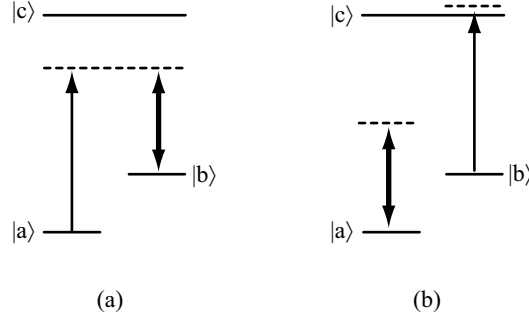


Figure 5.16: (a) On- and (b) off-Raman resonance coupling of the pump and probe fields.

Most of the features observed in this study involve strong modification of the atomic properties. Nonetheless, to order of magnitude, the strength of the CPT feature can be described in terms of an n_2 or $\chi^{(3)}$ response. Through the Kramer-Kronig relation, the change in the imaginary part of the refractive index is related to the change in the real part of the refractive index. As described in an Section 4.4.2, this narrow induced transparency feature results in a large group velocity for observing slow light.

The change in absorption is defined as $\Delta\alpha = 2\Delta n''\omega/c$, where $\Delta n''$ is the change in the imaginary part of the refractive index. Using the definition $\Delta n = n_2 I$, and the observation [see Fig. 5.9(c)] that the absorption changes by approximately 20% from the typical value of 0.14 cm^{-1} in the presence of a pump field of intensity 10 mW/cm^2 , the following can be calculated: $\text{Im}\{n_2\} = 1.1 \times 10^{-3} \text{ cm}^2/\text{W}$ or $\text{Im}\{\chi^{(3)}\} = 2.8 \times 10^{-2} \text{ esu}$. The nonlinear response per atom $\gamma^{(3)}$ is $\chi^{(3)}/N$ where $N = 10^{11} \text{ atoms/cm}^3$. The imaginary part of the response is $\text{Im}\{\gamma^{(3)}\} = 2.8 \times 10^{-13} \text{ esu}$. By comparison, the measured nonlinear response in a BEC [21], with the inclusion of an additional Stark shift, is: $\text{Im}\{n_2\} = 0.18 \text{ cm}^2/\text{W}$, $\text{Im}\{\chi^{(3)}\} = 4.5 \text{ esu}$, and $\text{Im}\{\gamma^{(3)}\} = 5.6 \times 10^{-14} \text{ esu}$.

5.4 Influence of Coherent Raman Scattering on CPT

Stray absorption as described earlier can cause the CPT resonances to be smaller but does it account completely for the observations in the experiment? A more detailed study is carried out next.

The probe laser was tuned across the Doppler profile with the frequency of the pump field fixed around the center of the $D1$ line in the preceding section and a variety of resonances were observed. In the following experiment, the resonance of CPT is studied with a smaller Raman detuning scan sampled across the Doppler profile.

5.4.1 Experiment

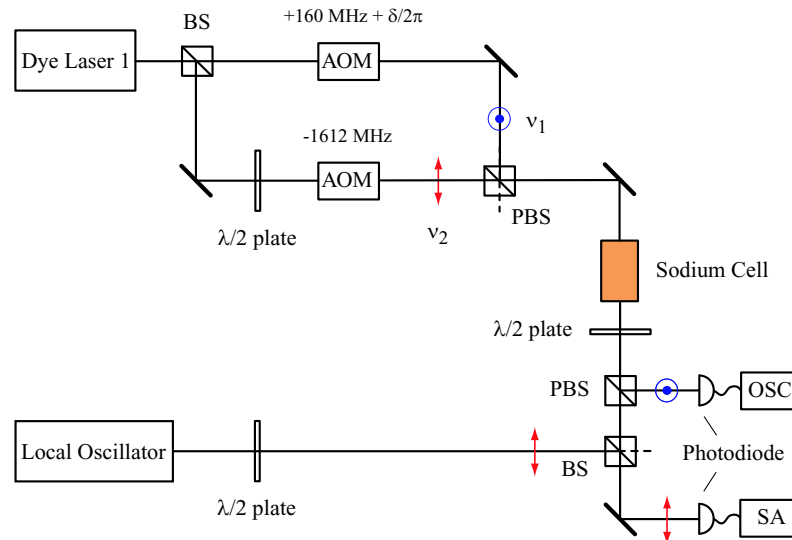


Figure 5.17: Schematic layout of the experiment to study the effect of coherent Raman scattering on CPT.

The Raman scattering - population trapping (CRS-CPT) experimental layout is depicted in Fig. 5.17. The experiment was performed with a single CW dye laser instead and the laser output was split into two beams. The polarization of one of the beams is rotated such that the two beams are of linear and mutually orthogonal polarization. The vertically polarized beam (blue) was double-passed through a variable-frequency AOM to vary the detuning ($\delta/2\pi$) around the Raman resonance and was up-shifted in frequency by 160 MHz. The frequency of this beam (ν_1) is nominally resonant with the transition between the $F = 1$ ground level and the unresolved excited levels

(F') of the sodium $D1$ line. The horizontally polarized beam (red) was passed through a fixed frequency (-1612 MHz) AOM to downshift the frequency of the beam. The frequency of this second beam (ν_2) is nominally resonant with the transition involving the $F = 2$ ground level. This layout creates a frequency difference between the two beams of 1772 MHz, close to that of the hyperfine ground levels separation of atomic sodium. These beams were combined using a polarizing beam splitter and directed into a sodium vapor cell. The power of each collimated beam going into the cell was 15 mW with a $1/e$ intensity diameter of 4 mm.

The vapor cell was shielded with a mu-metal case to reduce stray magnetic fields. 0.4 torr of helium was added to reduce the rate at which the sodium atoms diffuse out of the path of the laser beam instead of expanding the spot size of beam as was done previously. The cell was heated to 150 °C producing a number density of 10^{11} atoms/cm³. After propagation through the vapor cell, the beams were separated with a second polarizing beam splitter, detected with photodiodes, and monitored with an oscilloscope. A second dye laser was used as a local oscillator in a heterodyne detection setup to determine the frequency of any generated field. A second halfwave plate together with the polarizing beam splitter (after the cell) were used to select which polarization component is mixed with the local oscillator and sent to the spectrum analyzer. Note that any designation of field polarization refers to that of the beam before and in the cell, since the portion of the beam that is sent to the spectrum analyzer is always horizontally polarized to enable mixing with the local oscillator beam.

The detuning timings are illustrated schematically in the inset of Fig. 5.18(a). The Raman detuning ($\delta/2\pi$) was rapidly dithered as the single-photon detuning ($\Delta/2\pi$) was scanned slowly across the Doppler profile. The single-photon detunings of both beams were scanned by varying the frequency of the dye laser, whereas the Raman detuning was varied with the double-passed AOM. This dual-scan technique permits the observation of the Raman atomic response across the Doppler profile. There are three regions in the observed transmission spectra of Fig. 5.18(a). In Region I, induced absorption of the vertically polarized component is observed when the frequency difference between the two pump fields is tuned to the Raman resonance; the other component experiences increased transmission and even gain (note that the signal is larger than the far-off-resonance background). In Region II, both beams experience induced transparency. In Region III, induced absorption is observed for the horizontally polarized beam and increased transmission and

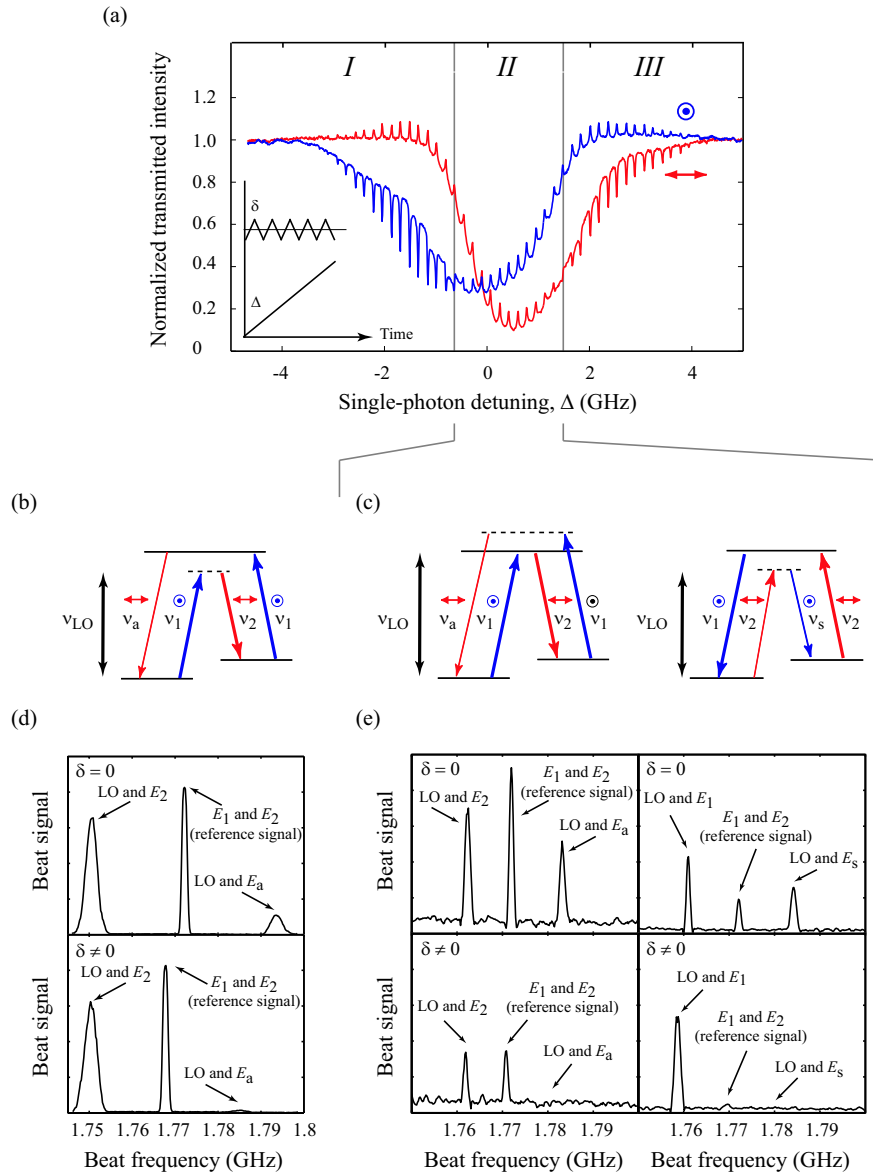


Figure 5.18: (a) Dual-scan experimental transmission spectrum of each polarization component. Inset: Timing diagram of the detuning scans. (b) Energy level diagram depicting CARS (Region I). (c) Energy level diagrams showing CARS on the left and CSRS on the right which occur simultaneously (Region II). (d) The beat signals are of the horizontally polarized fields (Region I) when the two pump fields are on ($\delta = 0$) and off ($\delta \neq 0$) the Raman resonance. (e) The beat signal of the horizontally (vertically)-polarized fields shows the presence of the CARS (CSRS) idler field (Region II).

gain is observed for the vertically polarized beam. In the transition areas between these regions [near the two vertical bars in Fig. 5.18(a)], the spectra have a dispersive-like profile. This is due to competition between the gain and induced absorption processes.

The underlying physical process giving rise to the rich spectral behavior of Fig. 5.18(a) is coherent Raman scattering. The energy-level diagram of Fig. 5.18(b) depicts CARS, which is the dominant process with red-detuned pump fields (Region I). The vertically polarized field ν_1 acts as an energy source which contributes two photons to amplify the horizontally polarized field ν_2 and create an anti-Stokes photon which is also horizontally polarized. CSRS is the dominant process with blue-detuned pump fields (Region III). In this region, the fields ν_1 and ν_2 swap roles as the energy source and recipient, and an increase in the number of vertically polarized photons is observed. In Region II, both CARS and CSRS [left and right energy level diagrams of Fig. 5.18(c)] occur simultaneously with comparable strength which leads to a cancellation of the number of photons absorbed from and emitted into each polarization component. Because of this cancellation, the transmission peaks observed in each polarization component occur entirely as a consequence of conventional CPT.

The presence of the idler field is confirmed by performing a heterodyne measurement of the frequency content of the beam emerging from the sodium cell. The frequency (ν_{LO}) of the local oscillator used in the measurement in Region I is tuned to approximately $\nu_1 - 20$ MHz as shown in Fig. 5.18(b). Figure 5.18(d) shows the heterodyne signal of the horizontally polarized component for frequencies near the difference frequency (1772 MHz) of the two pump fields (E_1 and E_2), which are red-detuned from the optical resonance. The beat signals are plotted on a linear vertical scale. The central peak of this spectrum is a reference signal representing the beat note between the two pump frequencies. This signal is present because of uncompensated birefringence in the sapphire windows of the vapor cell, which tends to mix the two initially orthogonal polarization components. This peak also has a small contribution from the beat note of E_1 and the generated field E_a . The left-most peak in the spectrum is the beat signal between the local oscillator and E_2 . The right-most peak is the beat note between the local oscillator and the generated anti-Stokes field; this contribution is greatly diminished when the two pump fields are detuned from the Raman resonance. The pump fields are tuned off the Raman resonance by shifting ν_1 (while holding ν_2 fixed), which causes the positions of the other two peaks to shift. The outer peaks are broader than

the reference peak because the two dye lasers are not phase-locked; consequently the beat frequency fluctuates. CSRS is also present but much weaker and the CSRS signal is on the vertically polarized component of the beam and far off resonance with the beat note at 2×1772 MHz.

The beat-note spectrum (not shown) for blue-detuned pump fields (Region III) have a similar appearance. The generated Stokes signal is vertically polarized and the beat note of the Stokes signal is observed (around 1772 MHz) by heterodyning the vertically polarized component of the beam with a local oscillator tuned near ν_2 .

When the pump fields are tuned near the single-photon resonance (Region II) both the CARS and CSRS processes influence the transmitted beam. The frequency of the local oscillator is tuned to approximately $\nu_1 - 10$ MHz for observing the CARS signal and approximately $\nu_2 + 10$ MHz for observing the CSRS signal, as shown in Fig. 5.18(c). CARS (CSRS) generates a horizontally (vertically) polarized idler field which can be observed in the beat signal spectrum of the horizontally (vertically) polarized beam with the pump fields on Raman resonance [Fig. 5.18(e)]. The reference and left-most peaks become lower when the pump fields are tuned away from the Raman resonance. This occurrence is due to the reduction of CPT in the off-Raman resonance condition while the pump fields are tuned near the peak of the Doppler absorption profile. This trace is noisier than that of Fig. 5.18(d) because less signal averaging was used in the present case.

The scattering efficiency is fairly large, $\lesssim 40\%$, as deduced from the dip of the spectrum in Region I of Fig. 5.18(a). In the presence of background absorption, not every scattered photon is detected. Therefore, the scattering efficiency is not calculated using the peaks. These experiments were repeated without any buffer gas in the cell and similar spectra were observed but with slightly reduced strength of the resonance features. This result shows that pressure broadening is not required for the occurrence of these Raman scattering processes. The amount and type of buffer gas were also varied. For all of the buffer gases used (helium, argon and nitrogen), the resonances are narrowed and the Raman scattering processes are enhanced as the buffer gas pressure is increased up to a value of a few torr. This behavior is due to the reduction of the ground state decoherence rate³ which, in this regime, is determined by the diffusion of sodium atoms out of the laser beam. Upon increasing the buffer gas pressure still further, all the resonances were found to weaken. In this regime pressure broadening of the optical resonance becomes important, and the saturation in-

³The reduced ground state decoherence rate causes an increase in the scattering efficiency.

tensity increases with buffer gas pressure. For the laser intensities used, the Rabi frequencies are not large enough to create a significant amount of ground state coherence. This trend was also observed in the numerical simulations.

5.4.2 Theoretical six-wave Λ model

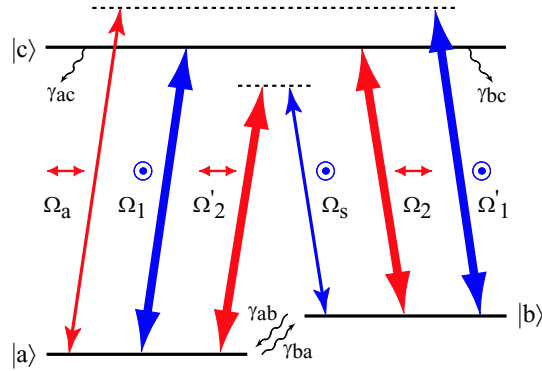


Figure 5.19: Energy level diagram of the six-wave three-level Λ system.

When two applied fields (which will be call the pump fields) are tuned to the Raman resonance of a Λ system, the probability amplitudes for excitation to the common upper level cancel as a consequence of quantum interference. A coherence between the two ground states, or equivalently a dark state [9], is thus created. In addition to providing transparency for both fields, this coherence can be utilized for the generation of an idler field by scattering a third (probe) field off this coherence. Based on energy conservation, the frequency of the idler field differs from that of the third field by the frequency difference of the two pump fields that created the coherence. However, this scattering process transfers population from one of the lower levels to the other, thus upsetting the original dark state. Absorption of additional photons out of the pump fields is necessary for re-establishing this dark state.

Although the $D1$ line of sodium couples 16 different hyperfine Zeeman levels [95], it will be approximated with a three-level Λ system. This simplification will lead to some discrepancies that are discussed at the end of this section.

In the model, each of the two applied fields ω_1 and ω_2 couple to both optical transitions of the Λ system. The ω_1 field is tuned near the a-c transition and acts as a pump field for this transition.

Likewise, the ω_2 field is tuned near the b-c transition and acts as a pump field for this transition. Since ω_1 is off resonance for the b-c transition, it serves as a probe field for this transition, and leads to the generation of light at the anti-Stokes frequency. Likewise ω_2 serves as a probe field for the a-c transition and leads to the generation of light at the Stokes frequency. This circumstance is illustrated in Fig. 5.19, which shows the Λ system with the six field contributions. The subscript ‘‘a’’ (‘‘s’’) indicates the generated anti-Stokes (Stokes) field which is not applied. The Ω_1 fields are vertically polarized while the Ω_2 fields are horizontally polarized. The labels without and with the prime (') indicate primary (pump) and secondary (probe) contributions of the applied fields respectively. The terms *pump* and *probe* are used only to distinguish between the two contributions of a particular applied field. Note that although $E_1 = E'_1$, the effective Rabi frequencies, $\Omega_{1,\text{eff}}(\Delta_1, \mu_{ca})$ and $\Omega'_{1,\text{eff}}(\Delta_1 + \zeta, \mu_{cb})$, need not be equal because the detunings and the dipole matrix elements μ_{ij} of the respective transitions are not equal. Nonetheless, the dipole matrix elements of the two optical transitions are of the same order of magnitude.

The fields are defined as

$$\tilde{E}(t) = (E_1 + E_a e^{-i\zeta t})e^{-i\omega_1 t} + (E_s e^{i\zeta t} + E_2)e^{-i\omega_2 t} + c.c., \quad (5.5)$$

where $\zeta = \omega_1 - \omega_2$. ω_1 is varied to change the Raman detuning, $\delta = \Delta_1 - \Delta_2 = \zeta - (2\pi * 1772 \text{ MHz})$, where $\Delta_1 = \omega_1 - \omega_{ca}$ and $\Delta_2 = \omega_2 - \omega_{cb}$. Angular frequencies are used exclusively for this section.

A rotating frame transformation and rotating-wave approximation are performed (as in Appendix A) on the density matrix equations of motion for a Λ system using

$$\rho_{ca} = \sigma_{ca} e^{-i\omega_1 t}, \quad (5.6a)$$

$$\rho_{cb} = \sigma_{ca} e^{-i\omega_2 t}, \quad (5.6b)$$

$$\rho_{ba} = \sigma_{ba} e^{-i(\omega_1 - \omega_2)t}. \quad (5.6c)$$

The equations are written in Appendix D.3 with the following matrix form

$$R \equiv [\sigma_{aa} \quad \sigma_{bb} \quad \sigma_{ba} \quad \sigma_{ca} \quad \sigma_{cb} \quad \sigma_{ab} \quad \sigma_{ac} \quad \sigma_{bc}]^T. \quad (5.7)$$

R can be solved (to all orders of the field strength) using the Fourier expansion and continued fraction method as outlined in Appendices B and C respectively. The atomic polarization at ω_1

is proportional to the fourth element of R_0 (Eq. 5.7) and the fifth element of R_1 (Eq. C.12). The atomic polarization at ω_2 is proportional to the fifth element of R_0 and the fourth element of R_{-1} (Eq. C.13). The atomic polarization of the anti-Stokes signal is proportional to the fourth element of R_1 , and that of the Stokes signal to the fifth element of R_{-1} . The ground state coherence is proportional to σ_{ba} (third element of R_0).

The atomic response is Doppler averaged, and the fields are propagated using the reduced wave equation

$$\frac{dE_j(\omega_j, z)}{dz} = i2\pi k_j P_j(\omega_j, z), \quad (5.8)$$

where E is the electric field, P is the Fourier component of the calculated atomic polarization, k is the wavevector, and $j = 1, 2, a$ or s . The slowly-varying amplitude approximation is used and no transverse effects are assumed. The numerical results were computed using the LP version of the Matlab code described in Appendix E.

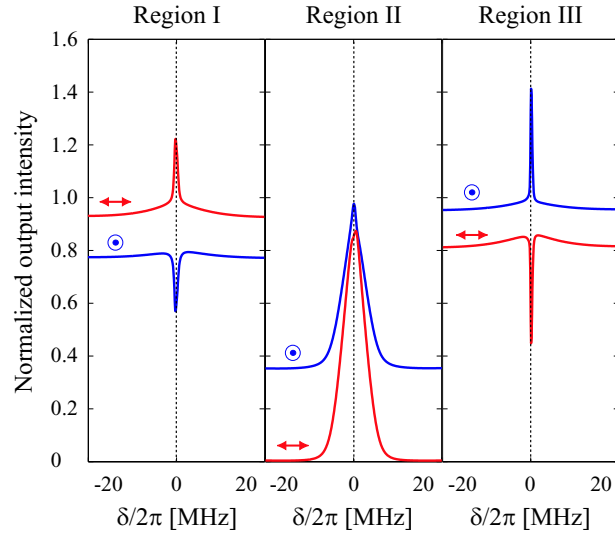


Figure 5.20: Theoretical spectra of the intensities of the two polarization components as a function of the Raman detuning δ for the three different regions of pump field detuning.

Fig. 5.20 shows the output intensities of the vertically and horizontally polarized components versus the Raman detuning δ for the three regions studied: Region I — red detuned pump fields ($\Delta = -\zeta$); Region II — pump fields tuned near to the resonance of the optical transitions ($\Delta = 0$); and Region III — blue detuned pump fields ($\Delta = \zeta$).

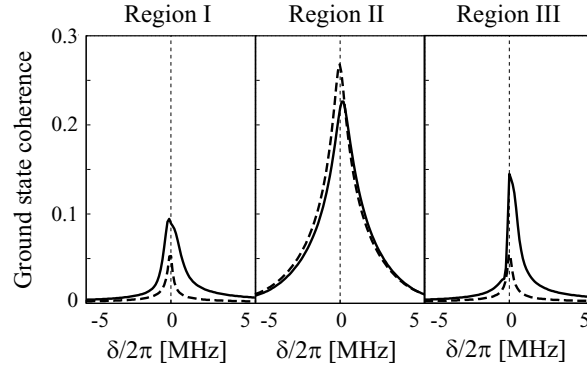


Figure 5.21: Theoretical spectra of the magnitude of the ground state coherence $|\sigma_{ba}|$, after propagation, for the 3 regions studied. The dash curve is with only CPT present while the solid curve includes both CARS and CSRS processes as well.

Fig. 5.21 shows the calculated ground state coherence $|\sigma_{ba}|$ after propagation. The dashed curve is with only CPT, and the solid curve is with both CPT and coherent Raman scattering processes present in the system. The CPT-only response is obtained by using only the zeroth Floquet order in the simulation, i.e. only the pump fields are present. In the presence of only CPT, in an ideal homogeneously broadened system without propagation, the one-photon-resonant ground state coherence has a maximal value of 0.5, which decreases significantly when the fields are far detuned from the optical resonance. In Region II, the peak coherence is slightly reduced when coherent Raman scattering is involved. However, in Regions I and III, the peak coherence is actually increased. This is not too surprising as Raman scattering is known to create coherence. The spectra in those regions are also somewhat asymmetric and shifted. With the inclusion of coherent Raman scattering, even the spectrum in Region II experiences a DC Stark-like shift.

The model also takes into account the possibility of interference between the CARS and CSRS processes. Additionally, non-parametric six-wave mixing processes are also accounted for.

The numerical results agree qualitatively with the experiment. The non-perfect transparency of the CPT resonances is due to a variety of less important experimental imperfections that result in weaker resonances due to additional absorption. For example, the 80 MHz AOM introduces sidebands which reduced the coherence between the ground states. The cleanliness of the sodium cell and purity of the buffer gases used also affects the amount of additional stray absorption that is introduced. The simplification of the theoretical model of sodium also fails to take into account other

less significant but concurrent processes that exist in the real system. When the second hyperfine excited level, or the Zeeman structure (see Fig. 3.2) is taken into account, even if they're degenerate, the CPT resonance will appear weaker, as discussed in Section 5.3.4.

5.5 Transfer of Modulation via CPT

In this section, a modulated signal is transferred from one beam to another, which can be at a very different part of the electromagnetic spectrum. There are two possible schemes: modulating one of the pump fields that are used to create the ground state coherence or modulating the probe field that scatters off that coherence. The modulated-pump scheme was performed and described here while the modulated-probe scheme was carried out in [55]. The modulated-probe (second) scheme involves a modulated probe field scattering off a steady dark state created by two unmodulated CW pump fields, see [86] for details. Since the fields can be Doppler-shifted into resonance, theoretically the second scheme has a bandwidth equivalent to the full Doppler width. A very asymmetric energy level structure is however required to achieve the transfer between different portions of the electromagnetic spectrum.

Both techniques can be used to frequency convert an ultrashort X-ray pulse created by high harmonic generation to the visible wavelength, which can then be used by current spectral phase interferometry for direct electric-field reconstruction (SPIDER) [96, 97] techniques to characterize the pulse. In the modulated-pump scheme, ultrashort X-ray pulses created by high-harmonic generation is detected by using two consecutive orders of the X-ray pulse as the pump fields. This scheme has the advantage of being able to easily transfer the modulation between fields of vastly differing frequencies compared to the modulated-probe scheme. However, the bandwidth for the modulation is comparatively limited.

5.5.1 Experiment

The experimental layout of the modulated-pump scheme is similar to that of the previous experiment. The beam ν_2 passing through the Brimrose AOM (1612 MHz) has an amplitude modulation (AM) signal imposed in addition to downshifting in frequency. The two beams were combined with a polarizing beamsplitter and coupled into a single-mode polarization-maintaining fiber designed

to operate at 600 nm. This fiber acts as a spatial filter and ensures good mode matching between the two beams. The output of the fiber was sent to the vapor cell. The intensities of each beam going into the cell are 10 mW with a beam diameter of 5 mm. The two pump fields were tuned to the Raman resonance to maximize the scattering. The multi-frequency output beam from the cell was then split with the polarizing beam splitter, and the modulated pump field together with the generated anti-Stokes idler field were mixed with a local oscillator from the second dye laser as in the previous experiment.

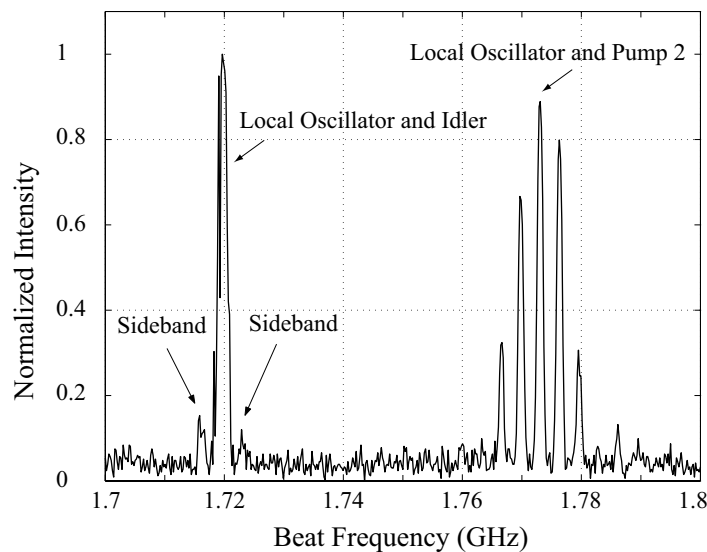


Figure 5.22: Beat signal spectrum of pump 2 and the idler with the local oscillator. The local oscillator is tuned near the frequency of pump 1. The triangular wave AM signal (sinc^2 envelope spectrum) imposed on pump 2 is transferred to the idler signal.

A modulated dark state is created by introducing an amplitude modulation on one of the pump field. When the unmodulated probe field is scattered off this ground state coherence, the modulation is transferred to the generated idler field as well, as can be clearly seen in Fig. 5.22. The modulation used is a 4 MHz triangular wave amplitude modulation which gives a sinc^2 envelope spectrum. However, Fig. 5.22 shows that only the first sidebands are transferred to the idler field. This is due to the limited bandwidth of CPT, i.e. the transparency window. This bandwidth is determined by the ground state decoherence rate. In this case, that rate is power broadened to a few MHz.

5.5.2 Theory

Although this scheme was performed using only the $D1$ line of sodium with one of the pump fields also acting as the probe field, the same results can be obtained using both D lines and three separately applied (non-degenerate) fields. Both pump fields can also be modulated (with the AM AOM in Fig. 5.2). In this proof-of-principle experiment, an up-conversion scheme generating a CARS idler field was used as opposed to a down-conversion of X-ray to optical frequencies.

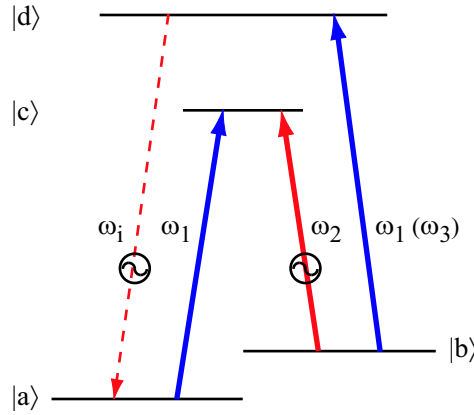


Figure 5.23: The modulated-pump scheme with modulation imposed only on ω_2 .

To numerically model the exact experiment that was performed requires applying a double Floquet expansion to the equations of motion, which is very computationally demanding. Instead, the model used will be for the more generic case with a double- Λ system and three individual fields. Only the pump field ω_2 is amplitude modulated and with a sine wave (one pair of sidebands). Figure 5.23 shows the energy level diagram of the model.

The equations of motion are similar to those of the 13 resonances experiment in Section 5.3 as shown in Appendix D.2. The elements of the interaction Hamiltonian V are however different and are given below.

$$\tilde{V}_{ca} = \hbar\tilde{\Omega}_1 = -\mu_{ca}E_1, \quad (5.9a)$$

$$\tilde{V}_{cb} = \hbar\tilde{\Omega}_m = -\mu_{cb}E_m, \quad (5.9b)$$

$$\tilde{V}_{db} = \hbar\tilde{\Omega}_3 = -\mu_{db}E_3, \quad (5.9c)$$

$$\tilde{V}_{da} = \hbar\tilde{\Omega}_i = -\mu_{da}E_i, \quad (5.9d)$$

where $E_m = (E_s e^{i\beta t} + E_2 + E_s e^{-i\beta t}) e^{-i\omega_2 t}$ is electric field component of the modulated pump field, E_i is that of the idler field, and β is the modulation frequency of pump field 2. Note that the fields on the optical transitions differs from those in Fig. 5.11. A rotating frame and a rotating wave approximation are performed with the following:

$$\rho_{ca} = \sigma_{ca} e^{-i\omega_1 t}, \quad (5.10a)$$

$$\rho_{cb} = \sigma_{cb} e^{-i\omega_2 t}, \quad (5.10b)$$

$$\rho_{db} = \sigma_{db} e^{-i\omega_3 t}, \quad (5.10c)$$

$$\rho_{da} = \sigma_{da} e^{-i\omega_i t}, \quad (5.10d)$$

$$\rho_{ba} = \sigma_{ba} e^{-i(\omega_1 - \omega_2)t} = \sigma_{ba} e^{-i(\omega_1 - \omega_2)t}, \quad (5.10e)$$

$$\rho_{dc} = \sigma_{dc} e^{-i(\omega_i - \omega_1)t} = \sigma_{dc} e^{-i(\omega_3 - \omega_2)t}. \quad (5.10f)$$

To eliminate the higher frequency components, the fields are required to be on the Raman resonance and that energy is conserved ($\omega_i = \omega_1 - \omega_2 + \omega_3$), for the last two equalities of Eqs. 5.10 to hold. The rule of population conservation is then used to eliminate ρ_{cc} from the equations. A Floquet expansion with the modulation frequency (β) as the index, and the continued fraction approximation are also applied. The equations of motion are solved as before with Doppler broadening and propagation.

5.6 Measurement of the Ground State Decoherence Rate

To characterize the sodium vapor in the cell, a ground state relaxation measurement is performed. The population (γ) and coherence (Γ) decay rates were measured using the configurations shown in Fig. 5.24 (see also Figs. 5.2 for the experimental layout). The same experimental layout (Fig. 5.25) was used in the modulated-probe scheme of the modulation transfer experiment in [55]. A photomultiplier tube (PMT) was used to detect the weak signal at the $D2$ line (ω_3 or ω_i). Note that the probe field ω_3 is applied to the $F = 2$ ground level and horizontally polarized just like the modulated-probe scheme in the previous section. This is accomplished by tuning the field slightly to the red side of resonance to ensure that it is far off resonance on the $F = 1 \rightarrow 3P_{3/2}$ transition. The probe field is made weak so that it does not redistribute the population through optical pumping.

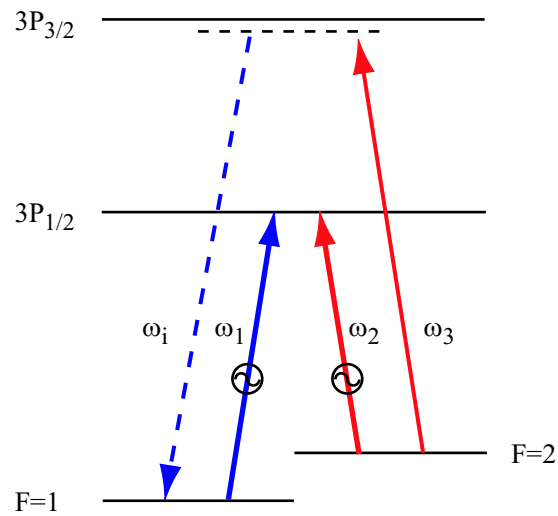


Figure 5.24: Energy level diagram depicting the method to measure the ground states relaxation rates.

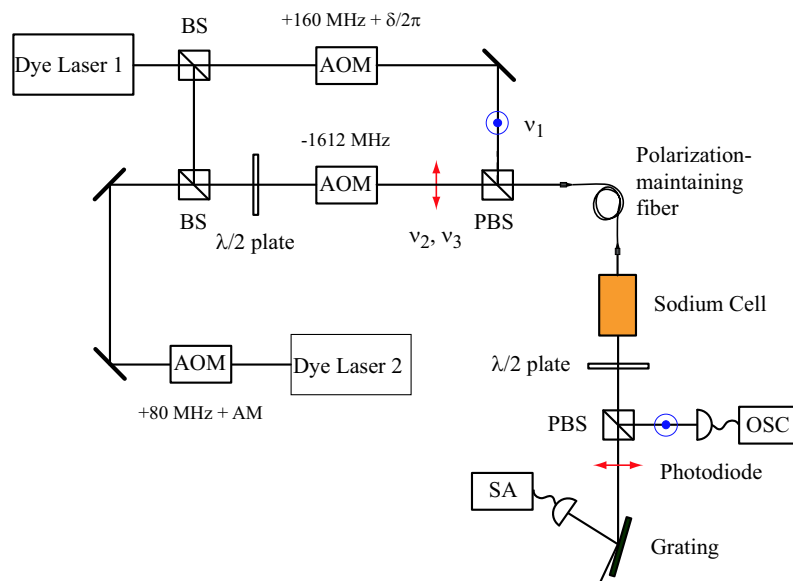


Figure 5.25: Experimental layout to measure the ground state relaxation rate of sodium.

The population decay rate was measured by observing the rate at which the ground state population returns to its no-field condition. Pump field ω_1 is blocked leaving only one amplitude modulated pump field (ω_2) to optically pump population to the $F = 1$ ground level (non-absorbing state). During the variable period of (off) time, the ground state population redistributes back to the absorbing

state and the transmitted probe field intensity is reduced.

To measure the ground state coherence relaxation rate, coherent Raman scattering is employed: the decay of the generated idler signal is directly related to the ground state decoherence rate. In this measurement, both the pump fields are modulated to prevent optical pumping during the measurement time slot.

5.6.1 Results

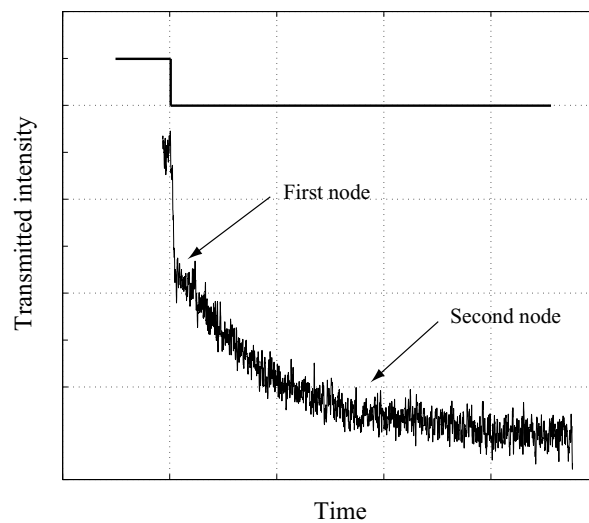


Figure 5.26: Intensity transmission trace of relaxation measurement.

Figure 5.26 shows a typical intensity trace of the relaxation measurement. The top curve is the pump field, and the bottom curve is the probe (idler) field for the population (coherence) relaxation rate measurement. On the transmitted signal trace, the steep linear drop before the first node is due to leak-through of the pump field. For example, in the population relaxation measurement, a portion of the pump field ω_2 was not completely separated from the probe field by the grating and was thus detected. The steep fall off shows the pump field switching off. The slower exponential decay after the second node is due to the sidebands imposed by the ISOMET AOM's as described earlier. Only the portion between the two nodes was used to curve-fit the measurement to extract the relaxation time. A diffusion model based on Brownian motion is used.

The relaxation rates were measured as a function of helium buffer gas pressure in the cell.

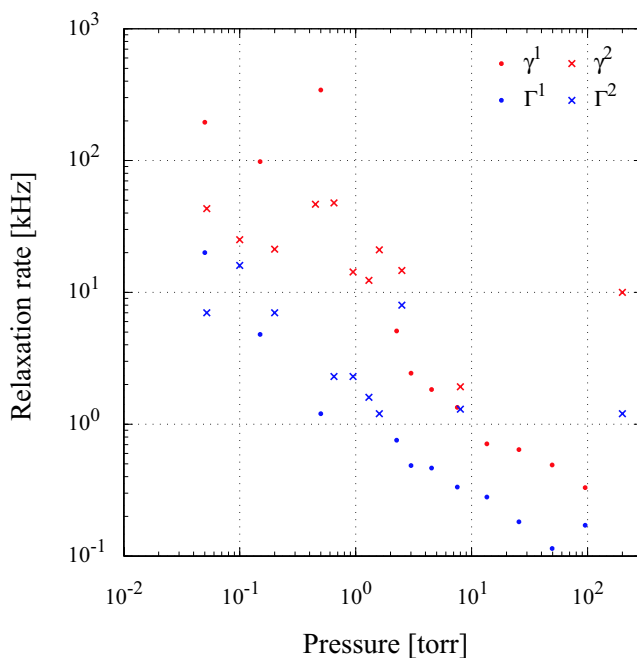


Figure 5.27: Ground states population (γ) and coherence (Γ) relaxation rates as a function of helium buffer gas pressure using two sets of pressure gauges.

Without a well calibrated pressure sensor, two different sensors were used to verify the data: a thermocouple-mechanical gauge pair and a thermistor gauge. The upper limit of the measurement range of the thermocouple is around 1 torr, and pressure readings above that were taken from the mechanical gauge. The thermistor gauge on the other hand is capable of spanning through the pressure range of interest. Figure 5.27 shows the population (γ) and coherence (Γ) relaxation rates at pressure readings from the thermocouple-mechanical gauges (¹) and the thermistor gauge (²). All curves have a trend of decreasing relaxation rate as the pressure is increased. This indicates that the cell is operating at the transit-time (diffusion) regime: the buffer gas is slowing down the rate in which the sodium atoms diffuse across the laser beam.

5.7 Summary

Multiple resonances are observed on the Doppler-broadened $D1$ line of atomic sodium in a pump-probe spectroscopic experiment. Each of these resonances has been explained in terms of simple

physical processes involving a four-level atomic system or a subset of this system. These resonances arise from various saturation effects (with sub-Doppler linewidth), and various atomic coherence effects (with sub-natural linewidth).

Coherent Raman scattering and its influence on CPT in a low-density atomic sodium vapor were also studied. The transmission spectra of the applied laser fields possess features having subnatural linewidths as a consequence of the quantum coherence of the underlying physical processes. An interplay between the Raman scattering processes and CPT is observed. When Raman scattering dominates, the usual CPT transparency peak can become inverted leading to a form of EIA.

By utilizing the ground state coherence as a source for coherent Raman scattering, frequency conversion can be achieved even with modulated fields. This is especially useful for down-converting X-ray attosecond pulses, created via high harmonic generation, for detection with SPIDER apparatus designed for the optical frequencies.

The ground state coherence can also be used to measure the population and coherence relaxation rates of sodium. The general trend of the result shows that the vapor cell is indeed operating in the transit-time regime.

6 The Semiconductor Band Structure

6.1 Introduction

Semiconductor systems differ greatly from atomic systems but yet have an uncanny resemblance. Just like ground states and excited states in an atomic system, a semiconductor system has a valence band and a conduction band separated by the band gap. Intrinsically, semiconductor systems have two carriers: electrons and holes. With proper design, a semiconductor system can be single-carrier as in atomic systems.

The carriers can also interact with each other and these interactions, known as many body effects, complicate any analysis of the system. The presence of phonons in solids also provides an extra form of interaction. Although the single-particle properties are still relevant, many body effects need to be included, which sometimes might alter the properties of the system radically.

The next two chapters provide a brief overview on the basics of semiconductor materials and the quantum well to aid reader in understanding the theoretical work at the end of Chapter 7.

6.2 Crystal Structure

In an atomic system of the sort described in the preceding chapters, the atoms are far apart and their valence electrons do not interact with each other. When the atoms are brought closer together to form a solid, bonding occurs and the discrete energy levels of the electrons form bands of very closely spaced levels as shown in Fig. 6.1(a).

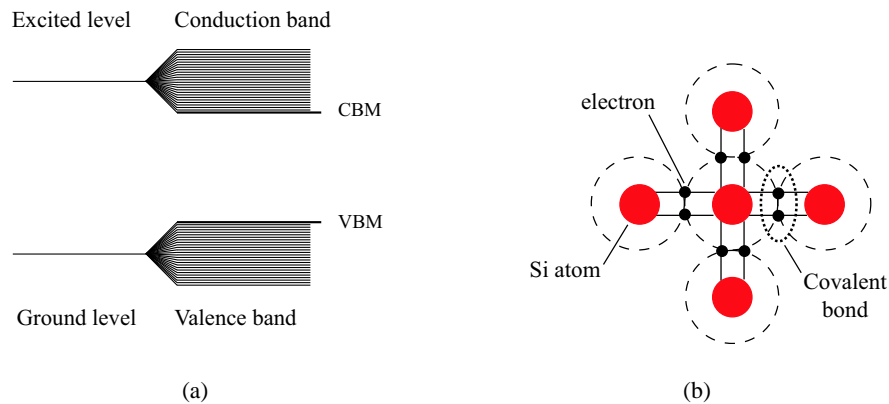


Figure 6.1: (a) Discrete energy levels forming bands in a semiconductor system. (b) A planar view of covalent bonds of semiconductors.

The most common and important bond in semiconductors is the covalent bond. Two adjacent atoms can share their valence electrons until the atom has a full outer shell by sharing with other neighboring atoms. Figure 6.1(b) shows the covalent bonds of a Group IV atom (e.g. silicon) and having a full outer shell of 8 “shared” electrons. Compounds can also form stable semiconductors through covalent bonds. Examples are the III-V semiconductors like gallium-arsenide.

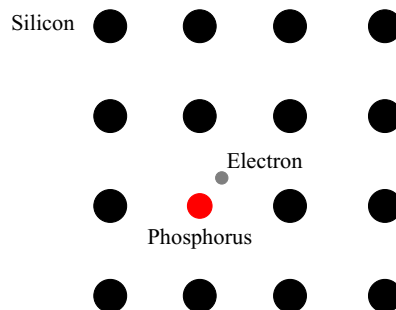


Figure 6.2: A donor atom with a free electron in the crystal lattice.

The semiconductor can also be doped (impurity atoms added), and that impurity atom that takes over one of the lattice site can be a donor or an acceptor (see Fig. 6.2). A donor (acceptor) has an extra electron (hole) that is free to move about the lattice. The concept of a hole is that it is positively charged carrier, an entity of a “missing electron”.

The treatment of the band structure will be given more formally below. There are two prevailing models: the $\mathbf{k} \cdot \mathbf{p}$ and the $\hat{\epsilon} \cdot \mathbf{p}$ theory. The concept of an effective mass will be shown with the $\mathbf{k} \cdot \mathbf{p}$

theory and the transition selection rules with the $\hat{\epsilon} \cdot \mathbf{p}$ theory.

6.2.1 The $\mathbf{k} \cdot \mathbf{p}$ theory

The $\mathbf{k} \cdot \mathbf{p}$ theory assumes that the band structure problem is solved at a particular point, k_o , with high symmetry. This point is taken as $k_o = 0$, the Γ -point of the Brillouin zone. It also assumes that all the energy eigenvalues $E_n(0)$ and their corresponding Bloch functions $u_n(k_o = 0, \mathbf{r}) = u_n(0, \mathbf{r})$ are known.

The treatment begins with the time-independent Schrödinger's equation, $H\Psi = E\Psi$, where the Hamiltonian is

$$H = \frac{\mathbf{p}^2}{2m_0} + V(\mathbf{r}), \quad (6.1)$$

$\mathbf{p} = -i\hbar\nabla$ is the momentum, m_0 is the electron rest mass, $V(\mathbf{r})$ is the periodic potential of the crystal, and \mathbf{r} is the three-dimensional spatial coordinate. The wavefunctions in a periodic crystal are the Bloch functions

$$\Psi_{n\mathbf{k}}(\mathbf{r}) = u_{n\mathbf{k}}(\mathbf{r})e^{i\mathbf{k} \cdot \mathbf{r}}, \quad (6.2)$$

where n is the band index, and \mathbf{k} is the wavevector. With ∇ operating on the plane-wave part of the wavefunction, only the “atomic-like” part of the Bloch functions need to be considered,

$$\left[\frac{(\mathbf{p} + \hbar\mathbf{k})^2}{2m_0} + V(\mathbf{r}) \right] u_{n\mathbf{k}}(\mathbf{r}) = E_{n\mathbf{k}}u_{n\mathbf{k}}(\mathbf{r}), \quad (6.3)$$

$$\left[\frac{p^2}{2m_0} + \frac{\hbar\mathbf{k} \cdot \mathbf{p}}{m_0} + \frac{\hbar^2 k^2}{2m_0} + V(\mathbf{r}) \right] u_{n\mathbf{k}}(\mathbf{r}) = E_{n\mathbf{k}}u_{n\mathbf{k}}(\mathbf{r}). \quad (6.4)$$

Envelope function approximation:

The most economical description of the energy bands in semiconductors is the effective mass approximation, which is also known as the envelope function approximation or multiband $\mathbf{k} \cdot \mathbf{p}$ method. It uses a minimal set of parameters that are determined empirically from experiments. By means of a perturbative approach, it provides a continuation in the wavevector k of the energy bands in the vicinity of some special point in the Brillouin zone.

In the four-band [conduction band (CB), heavy hole band (HH), light hole band (LH), and split off band (SO)], eight-band when spin is included, $\mathbf{k} \cdot \mathbf{p}$ approximation, coupling or transitions are among these four bands only. All higher empty conduction bands and lower filled valence bands are ignored. The interaction between the bands causes them to bend away from each other. The energies of the bands can be calculated using the non-degenerate perturbation theory, where

$$E_{nk} = E_{n0} + \frac{\hbar^2 k^2}{2m_0} + \frac{\hbar^2}{m_0^2} \sum_{i \neq n} \frac{|\mathbf{k} \cdot \langle i | \mathbf{p} | n \rangle|^2}{E_{n0} - E_{i0}} + \dots \quad (6.5)$$

The energy can be expressed in terms of an effective mass,

$$\frac{1}{m^*} = \frac{1}{m_0} + \frac{2}{m_0^2} \sum_{i \neq n} \frac{(\hat{k} \cdot \mathbf{p})^2}{E_{n0} - E_{i0}}, \quad (6.6)$$

where the k -component of the momentum \mathbf{p} is used. Using these equations (6.5 and 6.6), the energies of the four bands can be computed and the energy-wavevector ($E - k$) plots are parabolic which is the simplest approximation commonly used. To include an energy-dependent effective mass into the model, the higher order terms in Eq. 6.5) are used and this is equivalent to taking the non-parabolicity of the bands into account.

In the conduction band, the electron effective mass can be calculated using

$$\frac{m_0}{m_e^*} = 1 + \frac{2p_{cv}^2}{3m_0} \left(\frac{2}{E_g} + \frac{1}{E_g + \Delta_{so}} \right), \quad (6.7)$$

where E_g is the bandgap energy, Δ_{so} is the split-off energy and $p_{cv}^2 = \hbar^2 |\langle f | \frac{\partial}{\partial z} | i \rangle|^2$ and $\frac{p_{cv}^2}{2m_0}$ is usually approximately 22 eV. In a one dimensional (1D) quantum well structure, the energy-dependent effect masses are calculated with the following relations [98]:

$$\frac{m_w^*(E)}{m_0} = \frac{m_w^*}{m_0} [1 + E/(E_{g,w} + \Delta_w/3)], \quad (6.8a)$$

$$\frac{m_b^*(E)}{m_0} = \frac{m_b^*}{m_0} [1 + (V - E)/(E_{g,b} + \Delta_b/3)], \quad (6.8b)$$

where the subscript w (b) denotes the well (barrier) layer, and V is the potential of the barrier.

The conduction band is an s-like state just like the ground state of sodium. The valence band is p-like and consists of 3 bands (HH, LH and SO). In addition, there are spin up and spin down states

(for the electron) for each band. The quantum states $|j, m_j\rangle$ that describe the four bands are

$$\begin{aligned}
 CB : \quad & \left| \frac{1}{2}, \frac{1}{2} \right\rangle = i |S \uparrow\rangle, \\
 & \left| \frac{1}{2}, -\frac{1}{2} \right\rangle = i |S \downarrow\rangle, \\
 \\
 HH : \quad & \left| \frac{3}{2}, \frac{3}{2} \right\rangle = \frac{1}{\sqrt{2}} |(X + iY) \uparrow\rangle, \\
 & \left| \frac{3}{2}, -\frac{3}{2} \right\rangle = \frac{1}{\sqrt{2}} |(X - iY) \downarrow\rangle, \\
 \\
 LH : \quad & \left| \frac{3}{2}, \frac{1}{2} \right\rangle = \frac{1}{\sqrt{6}} |(X + iY) \downarrow\rangle - \sqrt{\frac{2}{3}} |Z \uparrow\rangle, \\
 & \left| \frac{3}{2}, -\frac{1}{2} \right\rangle = -\frac{1}{\sqrt{6}} |(X - iY) \uparrow\rangle - \sqrt{\frac{2}{3}} |Z \downarrow\rangle, \\
 \\
 SO : \quad & \left| \frac{1}{2}, \frac{1}{2} \right\rangle = \frac{1}{\sqrt{3}} |(X + iY) \downarrow\rangle + \frac{1}{\sqrt{3}} |Z \uparrow\rangle, \\
 & \left| \frac{1}{2}, -\frac{1}{2} \right\rangle = -\frac{1}{\sqrt{3}} |(X - iY) \uparrow\rangle + \frac{1}{\sqrt{3}} |Z \downarrow\rangle.
 \end{aligned} \tag{6.9}$$

The states $|\uparrow\rangle$ and $|\downarrow\rangle$ represent the electron spin up and down respectively. The states $|X\rangle$, $|Y\rangle$, and $|Z\rangle$ display the coordinate in which they are odd; they are even in the other two coordinate. The $|S\rangle$ state is even in all three Cartesian coordinates.

6.2.2 The $\hat{\epsilon} \cdot \mathbf{p}$ theory

There is a similar theory (to the $\mathbf{k} \cdot \mathbf{p}$ approximation) which is also often used to describe semiconductor materials; instead of taking the $\hat{\mathbf{k}}$ -component of the momentum \mathbf{p} , the Coulomb gauge and the component of the momentum in the direction of the polarization of the optical field are used. The absorption is defined as

$$\alpha = \frac{2\hbar W}{n_R \epsilon_0 \omega A^2 c}, \tag{6.10}$$

where A is the magnitude of the vector potential, n_R is the real part of the refractive index, and W is the transition rate given by the Fermi Golden Rule

$$W = \frac{2\pi}{\hbar} |\langle \Psi_f | H_{int} | \Psi_i \rangle|^2 \rho_J(\hbar\omega) \delta(E_f - E_i - \hbar\omega), \tag{6.11}$$

where E_i (E_f) is the energy of the initial (final) state, $\hbar\omega$ is the transition energy, and $\delta(\dots)$ is a delta function. If the initial and final states are partially occupied, the transition probability has to

be weighted by the occupancy factor given by the Fermi distribution function $f(E)$,

$$W_{fi} = W f(E_i)[1 - f(E_f)], \quad (6.12)$$

where the Fermi-Dirac distribution is given by

$$f(E) = \frac{1}{1 + e^{(E-\mu)/k_B T}} \approx e^{-(E-\mu)/k_B T}, \quad (6.13)$$

and the right-hand-side of Eq. 6.13 is the Boltzmann approximation. μ is the chemical potential and is approximated with the Fermi energy E_F at low temperatures,

$$\mu = E_F \left[1 - \frac{\pi^2}{12} \left(\frac{k_B T}{E_F} \right)^2 + \frac{\pi^4}{80} \left(\frac{k_B T}{E_F} \right)^4 + \dots \right]. \quad (6.14)$$

At higher donor densities, the Fermi energy level E_F moves up into the conduction band and it is no longer valid to use the Boltzmann approximation for the Fermi-Dirac function. The Fermi energy is defined as the energy state that has a $\frac{1}{2}$ probability of being occupied at a temperature of $T = 0$ K. E_F can be calculated using

$$E_F = \frac{E_c + E_v}{2} + \frac{1}{2} k_B T \ln \frac{N_v}{N_c} \quad \text{intrinsic semiconductor,} \quad (6.15)$$

$$E_{Fn} = E_c + k_B T \ln \frac{N_D}{N_c} \quad \text{n-doped semiconductor,} \quad (6.16)$$

$$E_{Fp} = E_v - k_B T \ln \frac{N_A}{N_v} \quad \text{p-doped semiconductor,} \quad (6.17)$$

where E_c is the energy of the conduction band minimum (CBM), E_v is the energy of the valence band maximum (VBM), N_c (N_v) is the conduction (valence) band effective density of states, and N_D (N_A) is the donor (acceptor) impurity density. The ratio $\frac{N_v}{N_c}$ is equal to $(m_h^*/m_e^*)^{3/2}$, where m_h^* and m_e^* are the effective masses of the hole and electron respectively. The Fermi energy can also be represented by the Fermi wavevector using $E_F = \frac{\hbar^2 k^2}{2m^*}$, where

$$k_F = \sqrt[3]{3\pi^2 N'} \quad \text{for 3D,} \quad (6.18)$$

$$= \sqrt{2\pi N'} \quad \text{for 2D,} \quad (6.19)$$

and $N' = \frac{N}{L^3}$ for the three dimensional (3D) electron density, or $N' = \frac{N}{L^2}$ for the two-dimensional (2D) sheet density. Note that bulk material is considered a 3D medium and a one dimensional (1D) quantum well is a 2D medium.

The delta function in Eq. 6.11 ensures energy conservation. Since there is not a single initial or final state, the transition probability has a *density of states* term. The *joint density of states* defines the number of states (n) per unit volume which can be excited per unit energy bandwidth and is defined as

$$\rho_J(E) = \frac{\Delta n}{\Delta \hbar\omega} = \frac{dn}{dE}. \quad (6.20)$$

For a quantum well, the joint density of states for a single subband is

$$\rho_J(\hbar\omega) = \frac{m^*}{\hbar^2 \pi W}, \quad (6.21)$$

where W is the width of the well layer.

The wavefunctions can be normalized with

$$\Psi(\mathbf{r}) = \frac{1}{\sqrt{N}} \sum_{n,\mathbf{k}} u_{n\mathbf{k}}(\mathbf{r}) e^{i\mathbf{k}\cdot\mathbf{r}}, \quad (6.22)$$

where N is the number of primitive cells, such that $\int \int \int_{\text{whole crystal}} \Psi^* \Psi dV = 1$, and $\int \int \int_{\text{whole crystal}} u^* u dV = 1$. Here, n is the wavefunction index. In a quantum well, the atomic part can be further decomposed into the confined part and the lateral part:

$$\Psi(\mathbf{r}) = \frac{1}{\sqrt{N}} \sum_{n,\mathbf{k}_{\parallel}} u_{n\mathbf{k}_{\parallel}}(\mathbf{r}_{\parallel}) \varphi(z) e^{i\mathbf{k}\cdot\mathbf{r}}, \quad (6.23)$$

where $\varphi(z) \propto \sin\left(\frac{n\pi z}{W}\right)$ is the envelope function in the confined direction \hat{z} , and $\mathbf{k}_{\parallel}(\mathbf{r}_{\parallel})$ is the wavevector (two-dimensional spatial coordinate) in the transverse direction.

In the Coulomb gauge ($\nabla \cdot \mathbf{A} = 0$), the electric field is related to the vector potential \mathbf{A} and the scalar potential ϕ by

$$\vec{\mathcal{E}} = -\nabla\phi - \frac{1}{c} \frac{\partial \mathbf{A}}{\partial t}, \quad (6.24)$$

where

$$\vec{\mathcal{E}} = \hat{\varepsilon} \frac{\mathcal{E}_0}{2} \left[e^{i(\mathbf{k}\cdot\mathbf{r}-\omega t)} + e^{-i(\mathbf{k}\cdot\mathbf{r}-\omega t)} \right]. \quad (6.25)$$

In the absence of free charges or current, $\phi = 0$ and

$$\mathbf{A} = \hat{\varepsilon} \frac{\mathcal{E}_0}{i2\omega} \left[e^{i(\mathbf{k}\cdot\mathbf{r}-\omega t)} + e^{-i(\mathbf{k}\cdot\mathbf{r}-\omega t)} \right], \quad (6.26)$$

where $\hat{\varepsilon}$ is the direction of the polarization of the electric field. The one electron Hamiltonian in the presence of an electromagnetic field is

$$H = \frac{1}{2m_0} (\mathbf{p} - e\mathbf{A})^2 + V(\mathbf{r}) + e\phi, \quad (6.27)$$

$$= \frac{p^2}{2m_0} + V(\mathbf{r}) - \frac{e}{2m_0} (\mathbf{p} \cdot \mathbf{A} + \mathbf{A} \cdot \mathbf{p}) + \left(\frac{e\mathbf{A}}{2m_0} \right), \quad (6.28)$$

where e is the electron charge, and $\phi = 0$ is used again. In the low intensity limit, the last term of Eq. 6.28 is dropped. With $\mathbf{p} \cdot \mathbf{A} = \mathbf{A} \cdot \mathbf{p}$ in the Coulomb gauge, the interaction hamiltonian becomes

$$H_{int} = \frac{ie\mathcal{E}_0}{2m_0\omega} (\hat{\varepsilon} \cdot \mathbf{p}), \quad (6.29)$$

$$= \frac{\hbar e\mathcal{E}_0}{2m_0\omega} \nabla_\varepsilon, \quad (6.30)$$

where $\mathbf{p} = -i\hbar\nabla$ is used, and $\nabla_\varepsilon = \hat{\varepsilon} \cdot \nabla$. The matrix element for a (001)-oriented quantum well is

$$\begin{aligned} \langle \Psi_f | \nabla_\varepsilon | \Psi_i \rangle &= \langle u_f^* \varphi_f^* | \nabla_\varepsilon | u_i \varphi_i \rangle, \\ &= \int \int \int_{\text{unit cell}} u_f^* \nabla_\varepsilon u_i dV \times \frac{1}{N} \sum_{z_i} \varphi_f^*(z) \varphi_i(z) \\ &+ \int \int \int_{\text{unit cell}} u_f^* u_i dV \times \frac{1}{N} \sum_{z_i} \varphi_f^*(z) \nabla_\varepsilon \varphi_i(z), \end{aligned} \quad (6.31)$$

where the first term on the right-hand-side of Eq. 6.31 represents the interband transition (IBT), and the second term is the intersubband transition (ISBT). The $e^{i\mathbf{k}\cdot\mathbf{r}}$ factors of the wavefunctions integrate to 1 if $\mathbf{k}_{\parallel}^f = \mathbf{k}_{\parallel}^i$, otherwise they make the matrix element equal to zero, so only vertical transitions need to be considered. Figure 6.3 shows the energy-wavevector ($E - k$) diagram of a quantum well with interband and intersubband transitions. The circles represent occupied energy states.

In analogy with atomic systems, an oscillator strength can be defined as

$$F_{fi} = \frac{2m^*(E_f - E_i)}{\hbar^2} |\mu_{fi}|^2. \quad (6.32)$$

From the second term of Eq. 6.31, the dipole moment of an ISBT is defined as

$$\mu_{fi} = e \langle f | \frac{\partial}{\partial z} | i \rangle \hat{\varepsilon} \cdot \hat{z}, \quad (6.33)$$

where $\hat{\varepsilon} \cdot \hat{z} = \cos(\theta)$, and θ is the angle between the direction of the electric field polarization ($\hat{\varepsilon}$) and the layer axis (growth direction, taken to be in the z-direction). The $\hat{\varepsilon} \cdot \hat{z}$ term is used to decompose

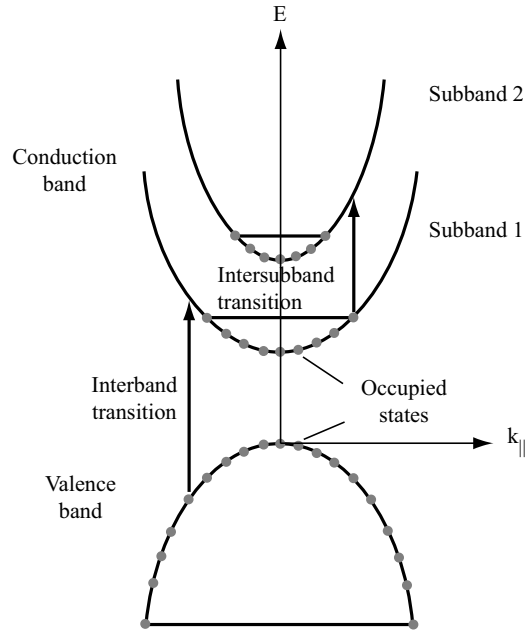


Figure 6.3: Energy-wavevector diagram showing interband and intersubband transitions.

the electric field if it is not polarized in the layer axis. Equation 6.33 defines the selection rules for ISBT: The electric field must be polarized in the layer axis to induce intersubband transitions. Correspondingly, when the electric field is polarized orthogonal to the layer axis, interband transitions are induced. For symmetric wells, since Eq. 6.33 is odd (in z), only transitions with odd Δn are allowed. In asymmetric wells, the rules are relaxed.

The differences between ISBT and IBT are as follow. ISBT is narrow, resonance-like while IBT has a broad range of energies because of (energy dependent) density of state considerations. ISBT is between same Bloch states and different envelope states, while IBT is between different Bloch states and same envelope states. The dipole moment of a transition is dependent on the structural width: ISBT is dependent on the well width of the quantum well (W), and IBT is dependent on the lattice constant ($L_{lattice}$) of the bulk material which is of the order of the Bohr radius a_0 . Therefore, $\frac{\mu_{ISBT}}{\mu_{IBT}} \sim 10 - 50$, although the absorption coefficient can sometimes be comparable.

6.3 Heterostructure

When two different semiconductor are joint, a heterojunction (Fig. 6.4) is formed. The Fermi energy level (E_F) of each semiconductor lines up, therefore shifting the band extrema accordingly: the conduction band offset (CBO) is $\Delta E_c = \chi_1 - \chi_2$, and the valence band offset (VBO) is $\Delta E_v = \Delta E_g - \Delta E_c$, where χ is the electron affinity, and ΔE_g is the difference in bandgap energy of the 2 semiconductors. The electron affinity is defined as the energy required to bring an electron from the CBM to the vacuum level (ionization). An analog to the heterojunction is a p-n diode where dissimilar dopants are used instead of dissimilar compounds.

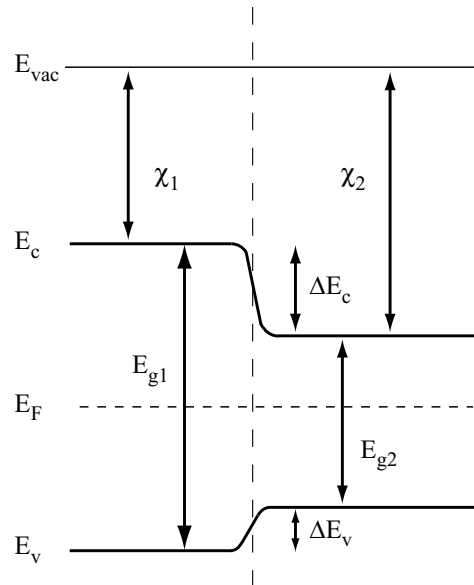


Figure 6.4: Energy level diagram of a heterojunction.

If the heterostructure is connected to an electrical source with the low bandgap material connected to the cathode, electrons from the cathode (right-hand-side) will flow towards the anode. Since there is a potential step at the heterojunction, if the applied voltage is comparatively small, the electrons will be trapped in the low-bandgap-side of the structure. The holes are, however, not trapped in this structure with this bias. Figure 6.4 shows a straddling configuration (or Type I) heterostructure. There are also staggered (Type II) and broken-gap (Type III) configurations although broken-gap ones are used only for special applications because the electron can easily tunnel through from the conduction band to the valence band on the other side of the heterojunction.

6.4 1D Quantum Well

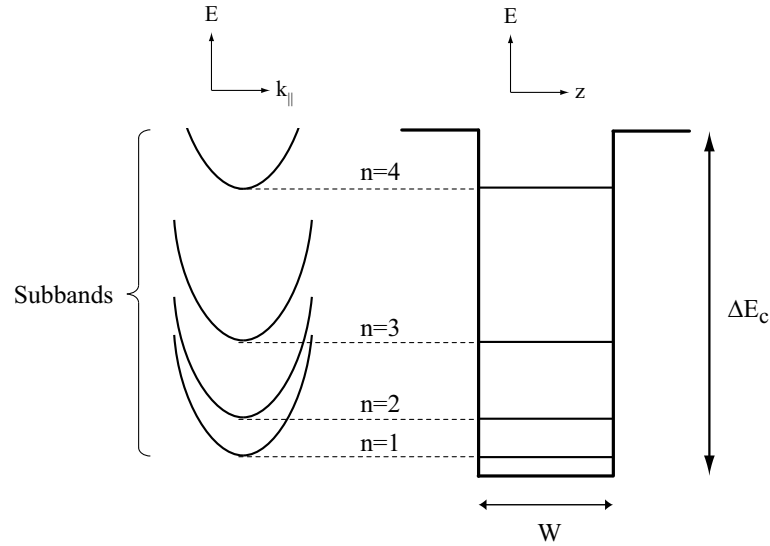


Figure 6.5: Subbands within the conduction band of a 1D quantum well.

When two heterojunctions are placed back-to-back with the center (well) layer shrunk to the de Broglie wavelength, a quantum well is created. As with the example given above, the carriers will be trapped in the well layer. A more important characteristic of a quantum well is that the (energy) band structure becomes quantized. Figure 6.5 shows a quantum well with quantized subbands within the conduction band. In a 1D quantum well with confinement in the \hat{z} direction, the energy of the subbands (in the infinite barrier model) are

$$E = E_x + E_y + E_z, \quad (6.34)$$

where

$$E_{xy} = \frac{\hbar^2 k_{\parallel}^2}{2m^*}, \quad (6.35)$$

$$E_{z,n} = \frac{\hbar^2 \pi^2}{2m^*} \left(\frac{n^2}{W^2} \right), \quad (6.36)$$

where n denotes the sublevel, and m^* is the effective mass of the carrier. Since the system is confined only in one dimension, subbands are obtained instead of sublevels (continuous range of energy levels due to the two unconfined dimensions) as in the left-hand-side diagram of Fig. 6.5. The electron effective mass m_e^* is used for m^* when calculating the energies of the subbands in the

conduction band. The well depth ($\Delta E_c = e|\chi_1 - \chi_2|$) is calculated from its composition and that of the barriers through the electron affinities, χ 's.

The conduction band is usually used for many intersubband applications because the electron mass is smaller than even the light hole's mass. This translates to higher mobility or tunnelling probability which permits the construction of faster optical switches, for example. The well depth in the conduction band is also generally larger than that in the valence band for most commonly used semiconductors.

The quantum well is usually physically very narrow (nanometers), therefore the interaction region is minute. The interaction length can be increased by stacking multiple single wells, forming a multiple quantum well structure as shown in Fig. 6.6(a). However, even with today's advanced molecular beam epitaxy techniques each well is slightly different from the other. In the same well, the layer thickness can also vary. This inhomogeneity causes the transition to broaden to a value that can be much larger than Doppler broadening in an atomic system. Alternatively, a single or few well(s) can be placed in a cavity with the surfaces of the wafer acting as mirrors as shown in Fig. 6.6(b). This approach can have a smaller inhomogeneously-broadened linewidth than the thicker single-pass multiple quantum well structure. The input facet is cleaved at an angle so that the optical beam is directed perpendicular into the wafer. With the high refractive indices of some semiconductors, significant refraction will occur if the optical beam is injected at an angle. In addition, total internal refraction can be utilized, instead of depositing reflecting layers on the wafer, to (partially) trap the optical beam.

6.5 Intersubband Transition

Quantum wells are already well developed for many optical applications. They utilize interband, intraband and intersubband transitions. Intraband or intersubband (within the same band) transitions are simpler because they involve only one type of carriers: electrons or holes, and these transitions are not affected by the recombination rate.

By varying the width of the well and the compositions of the material in the whole structure, a range of the number of subbands and transition energies can be created. By varying the thickness of

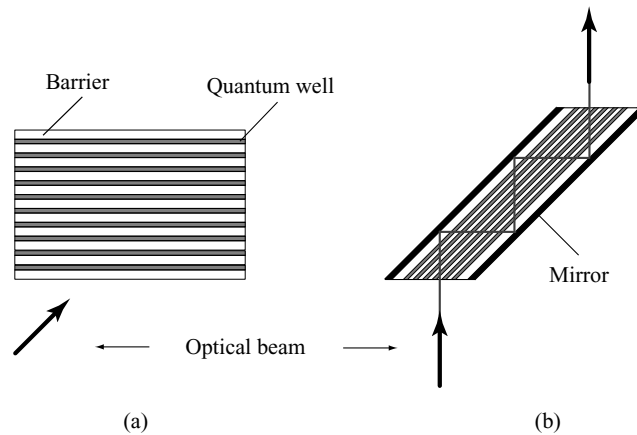


Figure 6.6: Two approaches to increase the interaction length of a quantum well medium: (a) Multiple quantum well structure, (b) single/multiple well(s) in a cavity.

the barrier between two coupled-wells, the coupling (dipole) strength and decay rate between levels in different wells can also be adjusted.

Intersubband transitions have large dipole moments [28, 34] and can be used to simulate transitions in an atomic system. These intersubbands in traditional semiconductors have transition frequencies in the far-infrared. With careful design and proper material selection, transitions at the communication wavelengths (1.3 and 1.55 μm) can be achieved [99]. The selection rules [100] for transitions among these levels are however different from an atomic system:

- an electric field polarized perpendicular to the plane of the layers is required to induce a transition,
- for a symmetric well, Δn must be odd.

The lifetimes of the excited levels of a typical atomic system (16 ns for radiatively-broadened sodium) is relatively long compared to those of the subbands in a quantum well system, which the latter are governed mainly by dephasing processes. In addition, the dephasing rates of the quantum well system are affected by more factors than in an atomic system. All forms of phonon scattering from the bulk material [101] to the interface regions [102] play a role in dephasing the transitions in the system.

6.6 System Dynamics

In a semiconductor system (or any solid), the atoms are bonded so closely together that they interact with each other and modify the energy level structure. Carrier-carrier interactions called many body effects, and phonons in solids modify the dynamics of the system as well. These interactions are included in the equations of motion either through the Hamiltonian or as an additional (phenomenologically-introduced) collision terms.

A complete and detailed analysis of these effects will involve transport theory. However, phenomenologically-introduced decay and dephasing terms are often used in the equations of motion to simplify the analysis when the focus is in the photo-induced dynamics and other properties of the system as is the case in the current work.

6.6.1 Many body effects

There are a few models [103] being used when treating many body effects, examples are the Hartree-Fock approximation, plasma screening, and the plasmon-pole approximation.

The Hartree-Fock approximation

In the Hartree-Fock approximation, the electrons are assumed to not interact with one another. Since the solution to the electronic problem is known for the single-electron atom (hydrogen), the Hamiltonian and the total electronic wavefunction are separated. The *Hartree product* or the N -electron wavefunction is obtained using the *Slater determinant*,

$$\Psi_{HP}(\mathbf{x}_1, \mathbf{x}_2, \dots, \mathbf{x}_N) = \frac{1}{\sqrt{N!}} \begin{vmatrix} \chi_1(\mathbf{x}_1) & \chi_1(\mathbf{x}_2) & \cdots & \chi_1(\mathbf{x}_N) \\ \chi_2(\mathbf{x}_1) & \chi_2(\mathbf{x}_2) & \cdots & \chi_2(\mathbf{x}_N) \\ \vdots & \vdots & \ddots & \vdots \\ \chi_N(\mathbf{x}_1) & \chi_N(\mathbf{x}_2) & \cdots & \chi_N(\mathbf{x}_N) \end{vmatrix}, \quad (6.37)$$

where $\chi_N(\mathbf{x}_N)$ is the electron wavefunction of electron N at position \mathbf{r}_N and spin ω ($\mathbf{x} = \{\mathbf{r}, \omega\}$). The antisymmetry principle is satisfied with this functional form for the wavefunction. In the two-electron wavefunction, if 2 electrons are placed in the same orbital at the same time $\chi_1 = \chi_2$, then

$\Psi_{HP}(\mathbf{x}_1, \mathbf{x}_2) = 0$. This is a result of the *Pauli exclusion principle* which is a consequence of the antisymmetry principle.

The assumption that the electrons can be described by an antisymmetrical product (Slater determinant) is equivalent to the assumption that each electron moves independently of each other but feels a Coulomb repulsion due to the average of the positions of all electrons. The electron also experiences an exchange interaction due to the antisymmetrization. That is why the Hartree-Fock theory is also referred to as the mean-field theory.

Plasma Screening

One of the most important effects of many body interaction in an electron plasma is plasma screening. The effective single particle interaction Hamiltonian can be written as

$$V_{\text{eff}}(r) = V(r) + V_{\text{ind}}(r), \quad (6.38)$$

where $V(r)$ is the Coulomb potential of a test charge, and $V_{\text{ind}}(r)$ is the induced potential of the screening particles. The induced potential obeys Poisson's equation and becomes

$$V_{\text{ind}}(q) = -\frac{4\pi e}{\epsilon_0 q^2} \rho_q = V_q V_{\text{eff}}(q) P^1(q, \omega), \quad (6.39)$$

where ρ_q is the charge density, q is the wavevector, V_q is the Coulomb interaction potential, and $P^1(q, \omega)$ is the first order approximation of the polarization function $P(q, \omega)$, and is defined as

$$P^1(q, \omega) = \sum_{\mathbf{k}} \frac{f_{\mathbf{k}-\mathbf{q}} - f_{\mathbf{k}}}{\hbar(\omega + i\delta + \omega_{\mathbf{k}-\mathbf{q}} - \omega_{\mathbf{k}})}, \quad (6.40)$$

where $f_{\mathbf{k}}$ is the carrier (Fermi-Dirac) distribution function. Substituting Eq. 6.39 into the Fourier transform of Eq.6.38 yields the dynamically screen Coulomb potential:

$$V_{\text{eff}} = \frac{V_q}{\epsilon(q, \omega)} \equiv V_s(q, \omega), \quad (6.41)$$

where the dynamic dielectric function is the Lindhard formula,

$$\epsilon(q, \omega) = 1 - V_q P^1(q, \omega). \quad (6.42)$$

Plasmon-Pole Approximation

In the long wavelength limit ($q \rightarrow 0$), Eq. 6.42 becomes the classical (Drude) dielectric function

$$\epsilon(0, \omega) = 1 - \frac{\omega_{pl}^2}{\omega^2}, \quad (6.43)$$

while in the static limit ($\omega + i\delta \rightarrow 0$),

$$\epsilon(q, 0) = 1 + \frac{\kappa^2}{q^2} \quad \text{for 3D,} \quad (6.44)$$

$$= 1 + \frac{\kappa}{q} \quad \text{for 2D,} \quad (6.45)$$

where the screening wavenumber is defined as

$$\kappa = \sqrt{\frac{4\pi e^2}{\epsilon_0} \frac{\partial N'_{3D}}{\partial \mu}} \quad \text{for 3D,} \quad (6.46)$$

$$= \frac{2me^2}{\epsilon_0 \hbar^2} f_{k=0} \quad \text{for 2D,} \quad (6.47)$$

and μ is the chemical potential. In both 2D and 3D, the inverse dielectric function is

$$\frac{1}{\epsilon(0, \omega)} = \frac{\omega^2}{(\omega + i\delta)^2 - \omega_{pl}^2} = 1 + \frac{\omega_{pl}^2}{(\omega + i\delta)^2 - \omega_{pl}^2}, \quad (6.48)$$

which has just 1 pole. This is used to construct an approximation for the full dielectric function $\epsilon(q, \omega)$, by replacing the continuum of poles obtained from the Lindhard formula with an effective plasmon pole at ω_q . This is the plasmon-pole approximation (replace ω_{pl} in the denominator of Eq. 6.48 with ω_q). The square of the effective plasmon frequency is

$$\omega_q^2 = \omega_{pl}^2 \left(1 + \frac{q^2}{\kappa^2} \right) + \nu_q^2 \quad \text{for 3D,} \quad (6.49)$$

$$= \omega_{pl}^2(q) \left(1 + \frac{q}{\kappa} \right) + \nu_q^2 \quad \text{for 2D,} \quad (6.50)$$

where the plasma frequency is

$$\omega_{pl} = \sqrt{\frac{4\pi N' e^2}{m}} \quad \text{for 3D,} \quad (6.51)$$

$$= \sqrt{\frac{2\pi N' e^2}{\epsilon_0 m} q} \quad \text{for 2D,} \quad (6.52)$$

and usually, $\nu_q^2 = Cq^4$, where C is a numerical constant.

6.6.2 Collision terms

The single particle density matrix equations of motion for a particular \mathbf{k} state is given by [42]

$$\frac{\partial \rho_{nm}^k}{\partial t} = -\frac{i}{\hbar} \left[H_0 + H_{int}, \rho_{nm}^k \right] + \frac{\partial \rho_{nm}^k}{\partial t} \Big|_{\text{relax}} . \quad (6.53)$$

H_0 is the system's Hamiltonian in the absence of the infrared field(s) and includes all the many body effects mentioned in previous sections, and H_{int} is the interaction Hamiltonian. The phenomenologically-included relaxation term consists of

$$\frac{\partial \rho_{nm}^k}{\partial t} \Big|_{\text{relax}} = \gamma_{nm}^k \rho_{nm}^k + \frac{\partial \rho_{nm}^k}{\partial t} \Big|_{\text{e-p}} + \frac{\partial \rho_{nm}^k}{\partial t} \Big|_{\text{e-e}} . \quad (6.54)$$

From this point forward, all analyses will be taken w.r.t. a quantum well structure (2D medium). γ_{nm} includes spontaneous decay rates (usually negligible) and other inelastic processes. The population decays (due to scattering processes) within the same subband are to other k states of the same subband, $\gamma_{nn}^{kk'}$. The terms $\frac{\partial \rho_{nm}^k}{\partial t} \Big|_{\text{e-p}}$ and $\frac{\partial \rho_{nm}^k}{\partial t} \Big|_{\text{e-e}}$ represent the incoherent contributions of the electron-phonon and electron-electron scattering processes respectively. The damping rates due to electron-electron scattering is always large (small) in the $|1, \mathbf{k}\rangle$ ($|2, \mathbf{k}\rangle$) state relative to the rates due to electron-phonon scattering, where $|1, \mathbf{k}\rangle$ ($|2, \mathbf{k}\rangle$) is the lower (upper) subband.

Incoherent electron-phonon scattering

For upper subbands which are separated from the ground subband by energies larger than those of the longitudinal-optical (LO) phonons, electron-LO phonon scattering is dominant. For the ground subband, this is primarily collisions between electrons and acoustic phonons which are weak and diffusive. The electron-phonon Hamiltonian can be written as [101, 104]

$$H_{\text{e-p}} = \sum_{\mathbf{q}} \left[\alpha(\mathbf{q}) e^{-i\mathbf{q}\cdot\mathbf{r}} b_{\mathbf{q}}^\dagger + c.c. \right], \quad (6.55)$$

where $b_{\mathbf{q}}^\dagger$ is the creation operator for a phonon in the mode \mathbf{q} and

$$|\alpha_{\text{LO}}(\mathbf{q})|^2 = 2\pi\hbar\omega_{\text{LO}} \frac{e^2 q^2}{L^3(q^2 + \kappa^2)} \left(\frac{1}{\epsilon_\infty} - \frac{1}{\epsilon_s} \right), \quad (6.56)$$

is the strength of the electron-optical phonon interaction (Fröhlich term), where ϵ_∞ and ϵ_s are the high energy and static dielectric constants respectively, L^3 is the volume, and $\hbar\omega_{\text{LO}}$ is the LO-phonon energy.

$$|\alpha_{\text{LA}}(\mathbf{q})|^2 = \frac{C_o}{L^3} \hbar \omega(\mathbf{q}), \quad (6.57)$$

is the strength of the electron-acoustic phonon interaction (deformation potential approximation). $C_o = \frac{D^2}{2\rho c_s^2}$, where D is the deformation potential for electrons, ρ is the density and c_s is the longitudinal velocity of sound. The scattering rate from an initial state $|i, \mathbf{k}_i\rangle$ to a final state $|f, \mathbf{k}_f\rangle$ is given by the Fermi Golden Rule [$W_{i \rightarrow f}(\mathbf{k}_i, \mathbf{k}_f)$, Eq. 6.11].

In general, the electron-phonon scattering is k -dependent. However, the linear response calculated with representative value is similar to that obtained from evaluating the complete system simultaneously. The phonon scattering is thus represented phenomenologically by

$$\frac{\partial \rho_{11}^k}{\partial t} |_{\text{e-p}} = \frac{\partial \rho_{11}^k}{\partial t} |_{\text{diff}}, \quad (6.58)$$

$$\frac{\partial \rho_{22}^k}{\partial t} |_{\text{e-p}} = -\gamma_2^p \rho_{22}^k, \quad (6.59)$$

where γ_2^p is the intersubband transition rate of an electron in the second subband due to emission of LO phonons. The off-diagonal terms are

$$\frac{\partial \rho_{nm}^k}{\partial t} |_{\text{e-p}} = -\Gamma_{nm}^p \rho_{nm}^k, \quad (6.60)$$

where Γ_{nm}^p is the dephasing rate caused by the electron-phonon scattering process and is given by

$$\Gamma_{nm}^p = \frac{1}{2} (\gamma_m^p + \gamma_n^p). \quad (6.61)$$

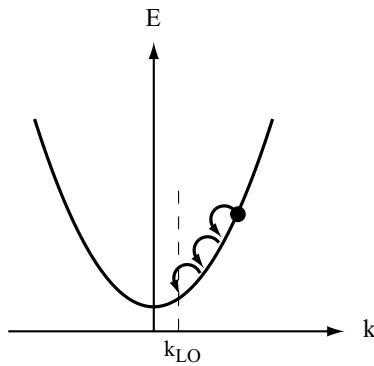


Figure 6.7: Intrasubband electron-phonon scattering.

For the ground subband, γ_1^p is the electron-acoustic phonon scattering rate $\left(\frac{\partial \rho_{11}^k}{\partial t} |_{\text{diff}}\right)$. LO-phonon scattering from much higher subbands to the ground subband can usually be ignored as

this requires phonons with very large wavevectors (energy). Electrons in states with $k > k_{LO}$ will undergo very fast intrasubband transitions (within the subband) until they reach a state with $k < k_{LO}$ (Fig. 6.7). If the subbands are separated by an integer number of LO-phonon energies, the electron will end up in a state with the same wavevector after an intersubband scattering.

Incoherent electron-electron scattering

This is a major damping process for electrons in the ground subband with wavevectors less than k_{LO} ($= \frac{\omega_{LO}}{c}$, the wavevector corresponding to an electron kinetic energy equal to that of LO phonons). This process depends on the electron density and distribution, and includes dynamic screening of the electron-electron interaction. Electron-electron effects are ignored in the upper bands because the upper bands are affected by the much faster electron-LO phonon scattering process and also because the electron envelope functions in these subbands are asymmetric and very much less localized in the well compared to those in the ground subband.

The electron-electron scattering rate is written as

$$\frac{\partial \rho_{nm}^k}{\partial t} |_{e-e} = \gamma_n^{\text{in}}(\mathbf{k}, \rho_{nn}^k) (1 - \rho_{nn}^k) - \gamma_n^{\text{out}}(\mathbf{k}, \rho_{nn}^k) \rho_{nn}^k. \quad (6.62)$$

$\gamma_n^{\text{in}}(\mathbf{k}, \rho_{nn}^k)$ and $\gamma_n^{\text{out}}(\mathbf{k}, \rho_{nn}^k)$ are the scattering in and out rates of state $|n, \mathbf{k}\rangle$ due to the electron-electron scattering process. The polarization dephasing rate is

$$\frac{\partial \rho_{nm}^k}{\partial t} |_{e-e} = -\Gamma_{nm}^{e-e}(k) \rho_{nm}^k + \frac{\partial \rho_{nn}^k}{\partial t} |_{\text{nd}}^{e-e}, \quad n \neq m \quad (6.63)$$

where the diagonal contribution to the dephasing rate is given by

$$\Gamma_{nm}^{e-e}(k) = -\text{Im}(\Sigma_n^{e-e}(k) + \Sigma_m^{e-e}(k)), \quad (6.64)$$

and Σ_n^{e-e} is the retarded self-energy which is related to γ_n^{out} and γ_n^{in} by

$$\text{Im}\{\Sigma_n^{e-e}(k)\} = -\frac{1}{2}(\gamma_n^{\text{in}} + \gamma_n^{\text{out}}). \quad (6.65)$$

The second term in Eq. 6.63 is the non-diagonal contribution of the electron-electron scattering process of the polarization dephasing rate. It describes the rate of polarization transfer between the state \mathbf{k} and other states due to scattering. This term partially cancels the diagonal contribution. In the limit of high electron density, this term can be neglected due to strong screening. Intersubband transitions caused by electron-electron scattering is ignored but this can be significant when the energy spacing between the subbands is small.

Interface roughness scattering

When the width of the layer of a quantum well structure varies, the transition wavelengths are shifted. Well width variations between various wells in a multiple quantum well structure therefore appear as an inhomogeneous (Doppler-like) broadening. Lateral variations (within a single heterointerface) usually dominate over inter-interface variations. In the case of very narrow layers where the dimensions of the variations are of the order of the layer width, these variations are very pronounced leading to interface roughness scattering [102, 105, 106] which reduces the electron mobility or equivalently increases the dephasing, leading to a broader absorption linewidth.

6.7 Summary

The concepts of atomic physics have been extended to relate to semiconductor physics, and a few relevant theories are introduced to help analyze a semiconductor system. The quantum well is also introduced, showing potential for realizing a Λ system to observe CPT.

7 Coherent Population Trapping in an Artificial Atom

7.1 Introduction

Due to the versatility of semiconductors, the demands for various diverse applications require the use of compounds from groups further away on the periodic table, e.g. II-VI compounds. Three-element or ternary alloys are also often employed. Two Group III or two Group V elements can be used to form a ternary semiconductor. Examples are $\text{Al}_x\text{Ga}_{1-x}\text{As}$ and $\text{AlAs}_{1-x}\text{Sb}_x$.

For the processes studied in the first half of this manuscript to have practical applications, a more robust medium is required. The quantum well fits the criteria to bridge physics to engineering in this case.

Coherence effects [107] have been observed in quantum well structures showing that it is possible to achieve EIT [41, 108] and CPT [36] in such a material system. Coupled-double wells [42] were proposed where the coupling and decay rates between levels in different wells can be controlled by the parameters of the barrier layer. The systems proposed in the literature however do not provide complete control of all the parameters. Such a limitation defeats one of the purpose of using quantum wells: the ability to alter almost any parameter to suit the application. In a three-level Λ system, the ability to control the decay and dephasing rates between the two ground levels is of upmost importance for CPT applications. The ability to control the decay rates from the excited level is also important as this decay rate determines the intensities of the fields required.

7.2 Quantum Well Structures

In the current quest to create a Λ system in a quantum well structure [109], the suitability of various basic designs were first considered. Although in a quantum well there exist subbands instead of discrete sublevels (as in the 1D analysis earlier or in a quantum dot structure), the simplification of subbands to sublevels is used. A uni-carrier (electrons) system is also used as a design criteria to eliminate inter-carrier interactions that will complicate the system. Therefore, only ISBT within the conduction band is utilized.

The quantum wells can be doped with one of the many schemes, for example delta doping or barrier doping, to bring the Fermi energy level above the sublevels that are designated as ground levels. Barrier doping is preferred as the positive impurity ions left behind are not in the well layer which can introduce an additional interaction.

There are a few potential structures for observing coherence effects, and ultimately CPT, using intersubband transitions in the conduction band of quantum wells. They are: a single well, a staggered well [42], a coupled-double well [108, 110, 111], and the one being proposed here: the *Island* well structure.

The single well structure, shown in Fig. 7.1(a), is the simplest to fabricate, and a Λ system can be realized using the $n = 1, 3$ and 4 sublevels. The two transitions, $|1\rangle \rightarrow |4\rangle$ and $|3\rangle \rightarrow |4\rangle$ are in the same physical layer. In this configuration, the decay rate between the two ground levels is around half of the decay rate between the excited level and the ground level. Population in level $|3\rangle$ decays to an intermediate level $|2\rangle$ that can then decay to level $|1\rangle$, all at the same rate. These decay rates are also not easily controllable.

A variation of the single well is the asymmetric or staggered well shown in Fig. 7.1(b). The well layer actually consists of two different layers of differing CBM energies, forming a step. Since the symmetry is broken, the second transition selection rule discussed in Chapter 6 do not apply, and transitions between any levels are allowed. The transition strengths are now calculated by the overlap of the respective wavefunctions. A Λ system is possible but the ground state decoherence rate is not very low.

The coupled-double well has two variations. If the two wells have an upper level of similar energies, as shown in Fig. 7.1(c), population in the excited level in one well can resonantly tunnel

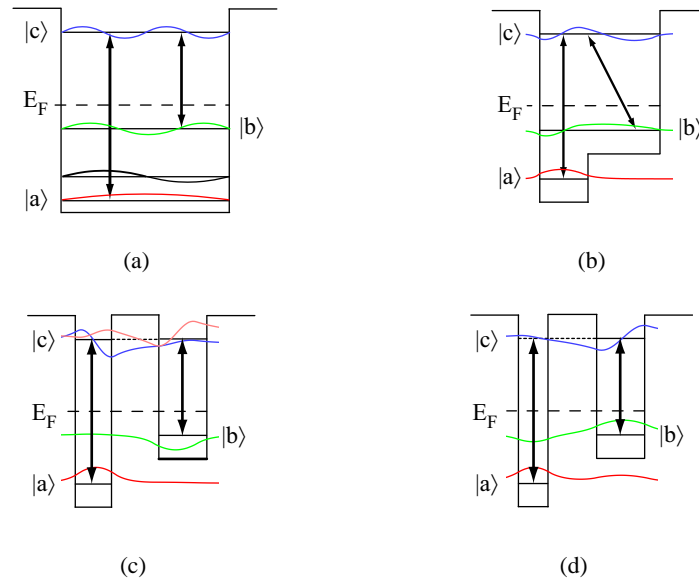


Figure 7.1: (a) The single well, (b) the staggered well, (c) resonantly, and (d) non-resonantly tunneled coupled-double well.

through the barrier to the excited level in the other well (a doublet is actually formed). This population can then be coupled to the ground level in the second well by an applied field. If the two wells do not have an upper level in close proximity (in energy), as in Fig. 7.1(d), then population in the excited level of one of the wells will tunnel non-resonantly through the barrier to the ground level in the second well. This non-resonant tunnelling will reduce the coupling strength (or equivalently the dipole moment) and the decay rate between the excited level and the second ground level. The benefit of the coupled-double well design is that the relative coupling strength and the excited level decay rates of the two transitions can be varied by the barrier thickness. However, the decay rate between the ground levels also varies by the same amount since they have the same barrier width.

By extending the concept of utilizing a barrier layer as an additional mean of controlling the decay rate and dipole moment, a triple well structure where the wavefunctions each of the levels of a Λ system are confined in their individual layers would yield the ideal layout. However, such a design will result in many interfaces where interface phonons can dominant the dephasing rates.

A compromise, using a variation of the staggered well termed the *Island* well as shown in Fig. 7.2, is proposed. The layers are: (i) $\text{AlAs}_{.56}\text{Sb}_{.44}$ barrier, (ii) $\text{In}_{.53}\text{Ga}_{.47}\text{As}$ deep well, and (iii) $\text{Al}_x\text{Ga}_{1-x}\text{As}_y\text{Sb}_{1-y}$ shallow well (the *Island*), all lattice-matched to InP. This structure is designed

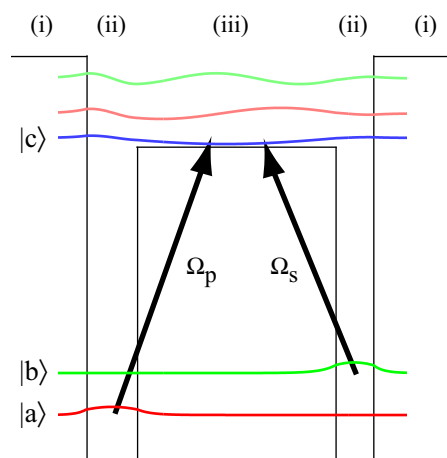


Figure 7.2: *Island well structure to create a Λ system.*

to confine the wavefunctions of the ground levels in physically separate layers with a thick barrier layer to minimize the dephasing rate of this non-optical transition. The dipole moments and transitional wavelengths of each of the two optical transitions are tailored for telecommunication applications, i.e. utilizing $1.3 \mu\text{m}$ and $1.55 \mu\text{m}$ fields.

To realize this design, a quaternary alloy is required for the shallow well layer in addition to the two ternaries for the deep well and barrier layers. The antimonide system, consisting of aluminum-arsenide-antimonide (AlAsSb) and indium-gallium-arsenide (InGaAs), latticed matched to indium phosphide (InP) has been shown to possess intersubband transitions, within the conduction band, of the communication wavelengths [99, 112]. It is well known within the fabrication community that replacing aluminum with gallium will lower the bandgap energy of the alloy. Therefore, the aluminum-gallium-arsenide-antimonide (AlGaAsSb) quaternary alloy is used for the shallow well layer.

7.3 Multi-Element Alloys

Although the parameters of most commonly used binary compounds are well known at low temperatures, the ultimate goal is to design semiconductors to operate at room temperature. Unfortunately some of the parameters, e.g. bandgap energy (E_g) and valence band offset (VBO), are temperature

(T) dependent. They can however be computed using Varshni's equation [113],

$$E_g(T) = E_g(0) - \frac{\alpha T^2}{T + \beta}, \quad (7.1)$$

where α and β are adjustable Varshni parameters. The room temperature parameters are then used in interpolation schemes to obtain the parameters of ternary alloys. It is found that quite often, linear interpolation over-estimate the parameter and a bowing factor is added as proposed by Vergard:

$$T_{XY} = xB_X + (1 - x)B_Y - x(1 - x)C, \quad (7.2)$$

where x is the composition, T_{XY} is the parameter of interest of the alloy, B is the parameter of the constituent (X or Y), and C is the bowing factor. The bandgap and other parameters, unless stated otherwise, are calculated in this manner. The conduction band offset CBO is equal to $E_g + \text{VBO}$, since VBO is negative for a Type I heterojunction.

The electron effective mass, introduced in Chapter 6.2.1, is then obtained using

$$\frac{m_o}{m_e^*} = (1 + 2F) + \frac{E_P(E_g + 2\Delta_{so}/3)}{E_g(E_g + \Delta_{so})}. \quad (7.3)$$

Both the E_P and F parameters are usually temperature independent, and the temperature variation of the effective mass arises only through the temperature-dependent bandgap energy. The following is a summary of the procedure used to obtain the parameters of a ternary alloy:

1. use the Varshni equation (Eq. 7.1) to obtain the bandgap energy of the binary compound at temperature T ,
2. linearly interpolate (Eq. 7.2) the E_P and F parameters for the ternary,
3. use the bowing parameter specified for the alloy to derive $E_g(T)$ and $\Delta_{so}(T)$ from Eq. 7.2,
4. obtain the temperature-dependent electron mass in the alloy using Eq. 7.3.

The parameters of the relevant binary compounds and ternary alloys for the three common points in the Brillouin zone (Γ , X and L) are compiled in Tables 7.1 and 7.2 respectively with $T' = (T - 300) \cdot 10^{-5}$. The bowing parameter is not used in the calculation if it is not stated. All (ternary) alloys are lattice matched to InP. CBO and VBO values are taken w.r.t. the indium antimonide (InSb) valence band maximum. Data in Roman (*Italic*) are taken (calculated) from tables of recommended

Semiconductor	InP	GaAs	InAs	AlAs	AlSb	GaSb
Bandgap	Direct (Γ)	Direct (Γ)	Direct (Γ)	Indirect (X)	Indirect (X)	Direct (Γ)
Composition x						
Latt. const. a (\AA)	$5.8697+2.79T'$	$5.65325+3.88T'$	$6.0583+2.74T'$	$5.6611+2.9T'$	$6.1355+2.6T'$	$6.0959+4.72T'$
$E_g^\Gamma(0K)$ [eV]	1.4236	1.519	0.417	3.099	2.386	0.812
α^Γ [meV/K]	0.363	0.5405	0.274	0.885	0.42	0.417
β^Γ [K]	162	204	93	530	140	140
$E_g^\Gamma(300K)$ [eV]	<i>1.3528857</i>	<i>1.4224821</i>	<i>0.3542519</i>	<i>3.0030361</i>	<i>2.3000909</i>	<i>0.7267045</i>
$C_{E_g}^\Gamma$ [eV]						
$E_g^X(0K)$ [eV]	$2.384-3.7 \times 10^{-4}T$	1.981	1.433	2.24	1.696	1.141
α^X [meV/K]	-	0.46	0.276	0.7	0.39	0.475
β^X [K]	-	204	93	530	140	94
$E_g^X(300K)$ [eV]	<i>2.273</i>	<i>1.8988571</i>	<i>1.3697939</i>	<i>2.1640964</i>	<i>1.6162276</i>	<i>1.0324975</i>
C_g^X [eV]						
$E_g^L(0K)$ [eV]	2.014	1.815	1.133	2.46	2.329	0.875
α^L [meV/K]	0.363	0.605	0.276	0.605	0.58	0.597
β^L [K]	162	204	93	204	140	140
$E_g^L(300K)$ [eV]	<i>1.9432857</i>	<i>1.7069643</i>	<i>1.0697939</i>	<i>2.3519643</i>	<i>2.2103636</i>	<i>0.7528864</i>
$C_{E_g}^L$ [eV]						
VBO [eV]	-0.94	-0.8	-0.59	-1.33	-0.41	-0.03
C_{VBO}^Γ [eV]						
CBO [eV]						
Δ_{so} [eV]	0.108	0.341	0.39	0.28	0.676	0.76
$C_{\Delta_{so}}$ [eV]						
E_P [eV] (w/o bow)	20.7	28.8	21.5	21.1	18.7	27
F (w/o bow)	-1.31	-1.94	-2.9	-0.48	-0.56	-1.63
$m_e^*(\Gamma)/m_0$	<i>0.0751677</i>	<i>0.0622614</i>	<i>0.02208</i>	<i>0.1456351</i>	<i>0.1352348</i>	<i>0.0350103</i>
m_e^*/m_0 from [114]	0.0795	0.067	0.026	0.15	0.14	0.039

Table 7.1: Band parameters at 300 K for the binary compounds.

$\text{In}_x\text{Ga}_{1-x}\text{As}$	$\text{AlAs}_{1-x}\text{Sb}_x$	$\text{GaAs}_{1-x}\text{Sb}_x$	$\text{Al}_x\text{Ga}_{1-x}\text{As}$	$\text{Al}_x\text{Ga}_{1-x}\text{Sb}$	Semiconductor
Direct (Γ)	Indirect (X)	Direct (Γ)			Bandgap
0.53	0.44	0.49	-	-	Composition x
5.8679	5.8698	5.8701			Latt. const. a (\AA)
					$E_g^\Gamma(0\text{K})$ [eV]
					α^Γ [meV/K]
					β^Γ [K]
2.4966202	0.7241941				$E_g^\Gamma(300\text{K})$ [eV] (w/ bow)
0.477	0.8	1.43	1.31x-0.127	1.22x-0.044	$C_{E_g}^\Gamma$ [eV]
					$E_g^X(0\text{K})$ [eV]
					α^X [meV/K]
					β^X [K]
1.2697136	1.8540421	1.1744609			$E_g^X(300\text{K})$ [eV] (w/ bow)
1.4	0.28	1.2	0.055	0	C_g^X [eV]
					$E_g^L(0\text{K})$ [eV]
					α^L [meV/K]
					β^L [K]
1.287061	2.220668	0.9395861			$E_g^L(300\text{K})$ [eV] (w/ bow)
0.33	0.28	1.2	0	0	$C_{E_g}^L$ [eV]
-0.594042	-0.503856	-0.157806			VBO [eV] (w/ bow)
-0.38	-1.71	-1.06			C_{VBO}^Γ [eV]
0.1434574	1.9927642	0.5663881			CBO [eV]
0.329605	0.41728	0.39637			Δ_{so} [eV] (w/ bow)
0.15	0.15	0.6	0	0.3	$C_{\Delta_{\text{so}}}$ [eV]
24.931	20.044	27.918			E_P [eV] (w/o bow)
-2.4488	-0.5152	-1.7881			F (w/o bow)
0.0378406	0.1313229	0.0318179			$m_e^*(\Gamma)/m_0$
0.0378	0.1317	0.0319			m_e^*/m_0 from [114]

Table 7.2: Band parameters at 300 K for the ternary alloys.

values in [114]. For comparison, the recommended values of the effective masses in [114] are given in the last row. Note that the bowing parameter for AlGaAs and AlGaSb are composition dependent, and AlAs_{0.56}Sb_{0.44} at compositions above ≈ 0.42 is an indirect gap semiconductor. The parameters for AlGaAs and AlGaSb are not calculated since they cannot be lattice matched to InP.

The quaternary alloy AlGaAsSb can be designed using two ternary alloys that are lattice matched to InP: (AlAs_{0.56}Sb_{0.44})_x(GaAs_{0.51}Sb_{0.49})_{1-x}. All the parameters for the quaternary can be calculated using the equivalent of Eq. 7.2 and the bowing parameter can be added if it is known. In theory, since the two ternaries are lattice-matched to InP, the quaternary will also be lattice-matched. In order to express the quaternary in a more commonly used notation, the following equality is used:

$$\text{Al}_x\text{Ga}_{1-x}\text{As}_y\text{Sb}_{1-y} \equiv (\text{AlAs}_{0.56}\text{Sb}_{0.46})_x(\text{GaAs}_{0.51}\text{Sb}_{0.49})_{1-x}, \quad (7.4)$$

where

$$y = 0.51 + 0.05x \quad 0 \leq x \leq 1. \quad (7.5)$$

However, a more detailed method as outlined by Adachi [115] is used instead. The quaternary is constructed from 4 binaries with compositions of the form $\text{A}_x\text{B}_{1-x}\text{C}_y\text{D}_{1-y}$. The quaternary parameter Q can be interpolated from the binary parameters (B 's) using

$$Q(x, y) = xyB_{AC} + x(1 - y)B_{AD} + (1 - x)yB_{BC} + (1 - x)(1 - y)B_{BD}, \quad (7.6)$$

or from the ternaries (T 's) if they are known:

$$\begin{aligned} Q(x, y) = & \{x(1 - x)[yT_{ABC}(x) + (1 - y)T_{ABD}(x)] \\ & + y(1 - y)[xT_{ACD}(y) + (1 - x)T_{BCD}(y)]\} / \{x(1 - x) + y(1 - y)\}, \end{aligned} \quad (7.7)$$

where the T 's can be obtained from Eq. 7.2 or measured experimentally. Note that even though two of the ternaries used in Eq. 7.7 cannot be lattice matched to InP, the resulting quaternary will be. The composition relation for lattice-matching $\text{Al}_x\text{Ga}_{1-x}\text{As}_y\text{Sb}_{1-y}$ to InP is

$$y = \frac{0.2262 + 0.0396x}{0.44265 + 0.03175x} \quad 0 \leq x \leq 1. \quad (7.8)$$

In the calculation of the lattice constant a , since there is no bowing Eqs. 7.6 and 7.7 gave the same results. A brief comparison of all three methods was performed. The first method is the linear

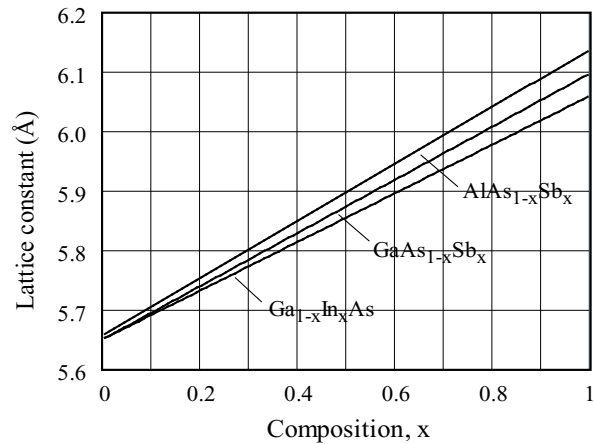


Figure 7.3: Lattice constant versus composition for the three ternaries that are lattice matched to InP.

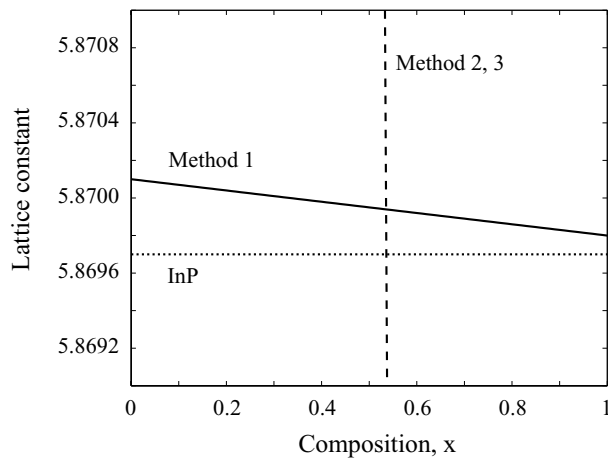


Figure 7.4: Lattice constant versus composition, calculated from the various methods.

interpolation of the two ternaries (based on well known values) using Eq. 7.2 and the composition relation defined by Eq. 7.5. The second method uses a 2D linear interpolation of the four binaries (Eq. 7.6) which does not include any bowing. The third method uses a 2D interpolation of the four ternaries (Eq. 7.7). This method uses Vegard's law to compute the parameters of the ternaries with bowing included, but does not include bowing when calculating the quaternary. Methods 2 and 3

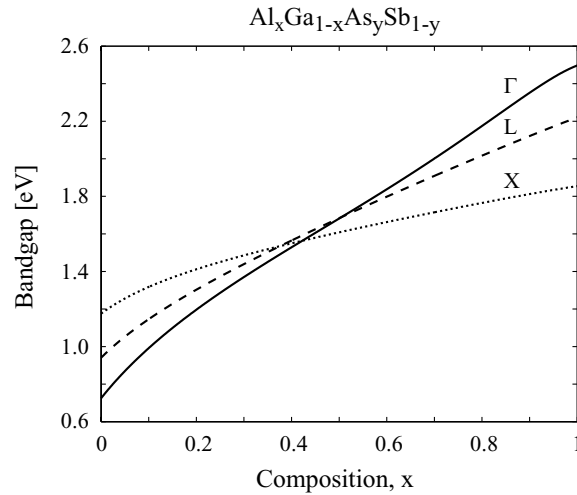


Figure 7.5: Direct and indirect bandgap energies of the quaternary calculated using Method 3.

use Eq. 7.8 for the composition relation. As an example, $x = 0.77$ was used,

$$\text{Method 1:} \quad y = 0.5485, \quad a = 5.8702 \text{ \AA}, \quad E_g^\Gamma = 2.0890 \text{ eV},$$

$$\text{Method 2:} \quad y = 0.5495, \quad a = 5.8697 \text{ \AA}, \quad E_g^\Gamma = 2.3236 \text{ eV},$$

$$\text{Method 3:} \quad y = 0.5495, \quad a = 5.8697 \text{ \AA}, \quad E_g^\Gamma = 2.1217 \text{ eV},$$

where $a_{\text{InP}} = 5.8697 \text{ \AA}$. Method 1 underestimate the bandgap energy and this is due to the fact that the 2 well known ternaries are not perfectly lattice matched to InP (see Figs. 7.3 and 7.4 and Table 7.2). The quaternary thus calculated cannot be perfectly lattice matched to InP. It should be noted that the mismatch is small, and within the tolerance of current fabrication techniques. Since Method 2 does not include any bowing, it overestimates the bandgap energy. It is also interesting to note that the bandgaps calculated with Method 3 have some upward bowing, see Fig. 7.5. This is caused by the use of Eqs. 7.7 and 7.8 and the composition dependence of the bowing parameter of AlGaAs and AlGaSb, which resulted in higher powers of the composition parameter in the equation.

7.4 Numerical Results of CPT in a Quantum Well System

7.4.1 The Island Well

It must be noted that the response of the system (Fig. 7.2) is the sum of the individual responses due to all sets of \mathbf{k} states with non-zero occupation probability weighted by the Fermi-Dirac distribution

function. To simplify the analysis, the single particle response is calculated using the density matrix equations of motion (Eqs. 6.53 and 6.54) with two applied optical fields, for a particular \mathbf{k} state. Since the linewidth of the CPT feature is dependent on the decoherence rate of the two ground levels, therefore non-scattering rates in the non-diagonal terms are included explicitly.

The electron-electron scattering (decay) and the LA-phonon scattering are taken to be intrasubband, from state k' to state k and vice versa. It is assumed that electron-electron scattering does not result in an intersubband transition because the excited level is well-separated from the ground levels, and there is no scattering of any sort between the two ground levels as the levels are in physically different quantum wells. The unperturbed population is assumed evenly distributed in the two ground levels since the Fermi level is in between the ground levels and the excited level. Therefore, any energy renormalization in the Hamiltonian due to many body effects affect both ground state equally, and therefore is unimportant in a Raman transition and will not be included.

The population in the excited state is also assumed small and thus electron-electron scattering of the excited state is negligible. In general, the (electron-phonon) scattering processes that cause intersubband transitions dominate over the spontaneous decay. In the present case, the sublevels are well separated which reduces the probability for intersubband transition but the wells are very narrow resulting in interface phonon scattering being the dominant dephasing process. It is assumed that there is no momentum change ($k_i = k_f$) for this type of scattering.

Electron-electron and LA phonon scattering are included only as a dephasing process, and the \mathbf{k} dependence of these dephasing rates are also ignored. The second term of Eq. 6.63 has been ignored with the assumption of screening due to high electron density. The term Γ_{ij}^{ns} is added to the decoherence rate, which is due to non-scattering processes like transit-time effects.

In the absence of any applied fields and using the rule of population conservation, in steady-state $\frac{\partial \rho_{aa}}{\partial t} |_{\text{diff}} = -\frac{\partial \rho_{aa}}{\partial t} |_{\text{e-e}}$. Similar relation holds for $\frac{\partial \rho_{bb}}{\partial t} |_{\text{diff}}$.

A rotating frame transformation is performed with the rotating wave approximation where

$$\rho_{ba} = \sigma_{ba} e^{-i(\omega_a - \omega_b)t}, \quad (7.9a)$$

$$\rho_{ca} = \sigma_{ca} e^{-i\omega_a t}, \quad (7.9b)$$

$$\rho_{cb} = \sigma_{cb} e^{-i\omega_b t}. \quad (7.9c)$$

The rule of population conservation ($\rho_{aa}^k + \rho_{bb}^k + \rho_{cc}^k = 1$) is used again to eliminate σ_{cc} from the equations of motion, and the reduced equations are written in Appendix D.4. The relaxation rates are assumed to be real.

7.4.2 Solving the eigenvalue problem in FEMLAB

The structural layout of the quantum well design can be drawn graphically using the FEMLAB interface or the code can be written direct into the m-file as describe in Appendix F. The eigenfunctions (wavefunctions) and eigenvalues (energies) of each of the sublevels (subbands when the lateral dimensions of the quantum well are taken into considerations) of the 1D structure are solved with the time-independent Schrödinger's equation of the form (used in FEMLAB)

$$-\nabla(c\nabla u) + au = \lambda u, \quad (7.10)$$

where u is the eigenfunction, λ is the eigenvalue, a is the energy potential (barrier height), and

$$\begin{aligned} c &= \frac{\hbar^2}{2m^*} \\ &= \frac{0.0381511}{m_e^*/m_0} \quad \text{in units of nm.} \end{aligned} \quad (7.11)$$

The dipole moments and transition wavelengths can then be computed from the wavefunction overlap integrals and energy level differences.

7.4.3 Photo-induced dynamics

The equations of motion in Appendix D.4 are used to calculate the absorption of the probe field as was done previously for the atomic system. For the simulation to be valid under CPT conditions, the absorption of the probe field is calculated exactly without using perturbation theory. The parameters in Table 7.3 are used in the simulation.

Fig. 7.6 shows the absorption of the probe field on the $|b\rangle \rightarrow |c\rangle$ transition versus pump-probe detuning for various pump field intensities. The CPT absorption dip is present despite additional sources of dephasing in a quantum well system, and the resonance feature power-broadens at higher field intensities.

Dipole/ non-scattering decay			Electron-electron scattering		
μ_{ca}	$0.22424 e / \sqrt{2}$	nm	γ_{aa}^{e-e}	1E4	ps^{-1}
μ_{cb}	$0.01853 e / \sqrt{2}$	nm	γ_{bb}^{e-e}	1E4	ps^{-1}
$\gamma_{ab,transit}$	0.1	ps^{-1}	γ_{cc}^{e-e}	1E3	ps^{-1}
Radiative decay			Electron-phonon scattering		
γ_{ab}	0.02	ps^{-1}	γ_{aa}^{e-p}	1E4	ps^{-1}
γ_{ba}	0.02	ps^{-1}	γ_{bb}^{e-p}	1E4	ps^{-1}
γ_{ac}	1	ps^{-1}	γ_{cc}^{e-p}	1E4	ps^{-1}
γ_{bc}	1	ps^{-1}	γ_{ab}^{e-p}	2E1	ps^{-1}
			γ_{ac}^{e-p}	1E5	ps^{-1}
			γ_{bc}^{e-p}	1E5	ps^{-1}

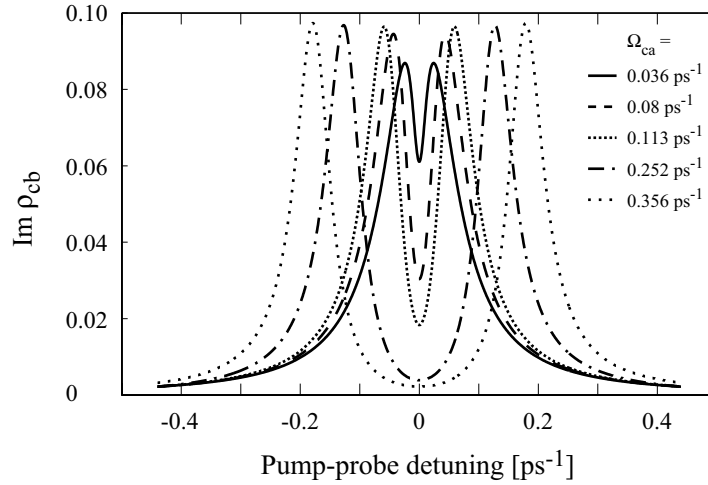
Table 7.3: Parameters used in the simulation of the *Island* well.

Figure 7.6: Probe absorption versus pump-probe detuning for various pump field intensities.

7.5 Summary

This chapter concludes the feasibility study of observing CPT in a quantum well system. An *Island* well was designed to mimic a Λ system as obtained in an atomic system. The antimonide-based quaternary system was used to create a uni-carrier system that operates at the two telecommuni-

cation wavelengths. As with predictions and observations of other quantum interference effects in quantum well systems in the literature, CPT is predicted and can be observed when the experimental difficulties are resolved.

8 Conclusion

Coherent population trapping (CPT) can be considered as a subset of a more general effect called electromagnetically induced transparency (EIT). It is a quantum interference effect with which a large ground state coherence is created that renders an otherwise opaque medium transparent. The transparency is within a very narrow window (sub-natural-linewidth) and has been experimentally observed to be only a few tens of Hz wide [24, 26]. The transparency feature can be employed in a variety of applications from frequency references to enhancement of other nonlinear processes (through the combination of the ground state coherence and the reduce or elimination absorption of the fields).

Sodium is commonly used to study nonlinear and coherence effects. Although many of these effects are described theoretically using an idealized three-level Λ system, the energy level structure of sodium is much more complicated.

In this thesis, CPT was studied in a sodium vapor cell. It is found that in addition to the CPT resonances, a variety of other resonances are observed in the Doppler-broadened $D1$ line, ranging from optical pumping effects to wave mixing processes. In particular, coherent Raman scattering directly affects the process of CPT; induced absorption and gain can be achieved instead of induced transparency. This complication can be turned around and be used as a means of frequency conversion, even with modulated signals.

The potential for diverse applications will be severely limited without a more practical medium to operate in. Unfortunately, sodium vapor cells are not suitable to make devices out of for these applications. Therefore, a feasibility study is undertaken in the quest for such a medium. Quantum

well systems are ideal in the present case. A new structure is designed, which utilizes the fairly new antimonide material system, for operation at telecommunication wavelengths. This *Island* well is engineered to resemble a Λ system in an atomic system. Numerical simulations predict the possibility of observing CPT. There are however a few experimental hurdles to overcome before this effect can be observed in the laboratory.

The widths of the wells in the design are very narrow, a few monolayers thick. Fabricating this structure can be difficult as it will be pushing the limits of current molecular beam epitaxy (MBE) technology. Interface phonon scattering might also prove to be too severe as a very intense laser beam is required to saturate the transitions (due to the broadening of the transition caused by phonon scattering). Although high-powered lasers are available, the damage threshold of the material has to be calculated before deployment.

The antimonide material system is relatively new, with only a handful of characterization measurements being performed. Therefore, the samples fabricated might deviate from design much more than the required tolerances. An alternative is to operate at lower wavelengths ($2\ \mu\text{m}$) or use a more mature material system for example AlGaAs-GaAs-AlInP which operates at even longer wavelengths. In that case, other scattering processes might dominate over surface phonon scattering. As long as the transition energies are above the LO phonon energy, the analysis done previously is still valid with an appropriate change of decay and dephasing rates implemented in the numerical simulation.

Here is a chronological list of follow-up work:

1. Fine tune the antimonide fabrication technique.
2. Include more dephasing processes and many body effects in the numerical model (less idealized).
3. Characterize single well systems.
4. Observe CPT in an *Island* well.

In summary, the objectives of this thesis work are to study CPT in a “real” (atomic) system and investigate the possibility of observing CPT in a semiconductor system (the “artificial” atom). These objectives have been achieved. This work has also laid the foundation for an exciting followup work of fabricating the quantum well structure, and implementing the diverse applications based on CPT.

Bibliography

- [1] M. Planck. *Verh. d. deutsch phys. Ges.*, 2:202, 237, 1900.
- [2] N. Bohr. *Phil. Mag.*, 26(6):1, 476, 857, 1913.
- [3] A. Einstein. *Ann. d. Physik*, 17(4):132, 1905.
- [4] P.A.M. Dirac. *Proc. Roy. Soc.*, A114:243, 710, 1927.
- [5] U. Fano. Effects of configuration interaction on intensities and phase shifts. *Phys. Rev.*, 124(6):1866, December 1961.
- [6] G. Alzetta, A. Gozzini, L. Moi, and G. Orriols. An experimental method for the observation of RF transitions and laser beat resonances in oriented Na vapour. *Nuovo Cimento B*, 36B(1):5, Nov 1976.
- [7] H.R. Gray, R.M. Whitley, and C.R. Stroud, Jr. Coherent trapping of atomic populations. *Opt. Lett.*, 3:218, 1978.
- [8] S.E. Harris, J.E. Field, and A. Imamoglu. Nonlinear optical processes using electromagnetically induced transparency. *Phys. Rev. Lett.*, 64(10):1107, March 1990.
- [9] E. Arimondo. Coherent population trapping in laser spectroscopy. volume 5 of *Progress in Optics XXXV*. Elsevier Science B.V., Amsterdam, 1996.
- [10] J. P. Marangos. Topical review: Electromagnetically induced transparency. *J. Mod. Optics*, 45(3):471–503, 1998.
- [11] S.E. Harris. Lasers without inversion: Interference of lifetime-broadened resonances. *Phys. Rev. Lett.*, 62(9):1033, February 1989.

- [12] O. Kocharovskaya and P. Mandel. Amplification without inversion: The double- λ scheme. *Phys. Rev. A*, 42(1):523, July 1990.
- [13] A. Imamoglu, J.E. Field, and S.E. Harris. Lasers without inversion: A closed lifetime broadened system. *Phys. Rev. Lett.*, 66(9):1154, March 1991.
- [14] Y.F. Zhu. Lasing without inversion in a closed three-level system. *Phys. Rev. A*, 45:6149, 1992.
- [15] G. Grynberg, M. Pinard, and P. Mandel. Amplification without population inversion in a V three-level system: A physical interpretation. *Phys. Rev. A*, 54:776, 1996.
- [16] M.D. Lukin, P.R. Hemmer, M. Löffler, and M.O. Scully. Resonant enhancement of parametric processes via radiative interference and induced coherence. *Phys. Rev. Lett.*, 81(13):2675, September 1998.
- [17] B.S. Ham, M.S. Shahriar, and P.R. Hemmer. Enhancement of nondegenerate four-wave mixing owing to electromagnetically induced transparency in a spectral hole-burning crystal. *Optics Lett.*, 22(15):1138, August 1997.
- [18] M.O. Scully. Enhancement of the refractive index via quantum coherence. *Phys. Rev. Lett.*, 67(14):1855, September 1991.
- [19] U.W. Rathe, M. Fleischhauer, S.Y. Zhu, T.W. Hänsch, and M.O. Scully. Nonlinear theory of index enhancement via quantum coherence and interference. *Phys. Rev. A*, 47(6):4994, June 1993.
- [20] V. Wong, R.W. Boyd, C.R. Stroud, Jr., R.S. Bennink, and D.L. Aronstein. Absorptionless self-phase-modulation via dark-state electromagnetically-induced-transparency. *Phys. Rev. A*, 65:013810, 2001.
- [21] L.V. Hau, S.E. Harris, Z. Dutton, and C.H. Behroozi. Light speed reduction to 17 metres per second in an ultracold atomic gas. *Nature (London)*, 397(February):594, February 1999.
- [22] J.E. Thomas, P.R. Hemmer, S. Ezekiel, C.C. Leiby, Jr., R.H. Picard, and C.R. Willis. Observation of Ramsey fringes using a stimulated, resonance Raman transition in a sodium atomic beam. *Phys. Rev. Lett.*, 48(13):867, March 1982.

- [23] P.R. Hemmer, S. Ezekiel, and C.C. Leiby, Jr. Stabilization of a microwave oscillator using a resonance Raman transition in a sodium beam. *Opt. Lett.*, 8(8):440, August 1983.
- [24] S. Brandt, A. Nagel, R. Wynands, and D. Meschede. Buffer-gas-induced linewidth reduction of coherent dark resonances to below 50 Hz. *Phys. Rev. A.*, 56(2):R1063, August 1997.
- [25] J. Kitching, S. Knappe, and L. Hollberg. Miniature vapor-cell atomic-frequency references. *Appl. Phys. Lett.*, 81(3):553, July 2002.
- [26] M. Merimaa, T.L., I. Tittoonen, and E. Ikonen. All-optical atomic clock based on coherent population trapping in ^{85}Rb . *J. Opt. Soc. Am. B*, 20(2):273, February 2003.
- [27] A. Kamgar, P. Kneschaurek, G. Dorda, and J.F. Koch. Resonance spectroscopy of electronic levels in a surface accumulation layer. *Phys. Rev. Lett.*, 32(22):1251, June 1974.
- [28] L.C. West and S.J. Eglash. First observation of an extremely large-dipole infrared transition within the conduction band of a GaAs quantum well. *Appl. Phys. Lett.*, 46(12):1156, June 1985.
- [29] C.G. Bethea, B.F. Levine, V.O. Shen, R.R. Abbott, and S.J. Hsieh. 10 μm GaAs/AlGaAs multiquantum well scanned array infrared imaging camera. *IEEE Trans. Elect. Devices*, 38(5):1118, May 1991.
- [30] N. Holonyak, Jr., R.M. Kolbas, E.A. Rezek, and R. Chin. Bandfilling in metalorganic chemical vapor deposited $\text{Al}_x\text{Ga}_{1-x}\text{As}$ -GaAs- $\text{Al}_x\text{Ga}_{1-x}\text{As}$ quantum-well heterostructure lasers. *J. Appl. Phys.*, 49(11):5392, June 1978.
- [31] F. Capasso, J. Faist, C. Sirtori, and A.Y. Cho. Infrared (4-11 μm) quantum cascade lasers. *Solid State Comms.*, 102(2-3):231, 1997.
- [32] D.V. Regelman, U Mizrahi, D. Gershoni, E. Ehrenfreund, W.V. Schoenfeld, and P.M. Petroff. Semiconductor quantum dots: a quantum light source of multicolor photons with tunable statistics. *Phys. Rev. Lett.*, 87(25):257401, December 2001.
- [33] D. Fröhlich, A. Nöthe, and K. Reimann. Observation of the resonant optical Stark effect in a semiconductor. *Phys. Rev. Lett.*, 55(12):1335, September 1985.

- [34] C. Sirtori, F. Capasso, D.L. Sivco, and A.Y. Cho. Giant, triply resonant, third-order nonlinear susceptibility $\chi_{3\omega}^{(3)}$ in couple quantum wells. *Phys. Rev. Lett.*, 68(7):1010, February 1992.
- [35] Y. Zhao, D. Huang, and C. Wu. Electromagnetically induced transparency of interband transitions in quantum wells. *Quantum Opt.*, 6:327, 1994.
- [36] M. Phillips and H. Wang. Electromagnetically induced transparency due to intervalence band coherence in a GaAs quantum well. *Opt. Lett.*, 28(10):831, May 2003.
- [37] M.C. Phillips, H. Wang, I. Rumyantsev, N.H. Kwong, R. Takayama, and R. Binder. Electromagnetically induced transparency in semiconductors via biexciton coherence. *Phys. Rev. Lett.*, 91(18):183602, October 2003.
- [38] J. Faist, C. Sirtori, F. Capasso, S.G. Chu, L.N. Pfeiffer, and K.W. West. Tunable Fano interference in intersubband absorption. *Opt. Lett.*, 21(13):985, July 1996.
- [39] A. Imamoğlu and R.J. Ram. Semiconductor lasers without population inversion. *Opt. Lett.*, 19(21):1744, November 1994.
- [40] S.M. Sadeghi, J.F. Young, and J. Meyer. Intersubband optical response of semiconductor quantum wells dressed by strong infrared fields. *Phys. Rev. B*, 51(19):13349, May 1995.
- [41] G.B. Serapiglia, E. Paspalakis, C. Sirtori, K.L. Vodopyanov, and C.C. Phillips. Laser-induced quantum coherence in a semiconductor quantum well. *Phys. Rev. Lett.*, 84(5):1019, 2000.
- [42] S.M. Sadeghi, S.R. Leffler, and J. Meyer. Quantum interference and nonlinear optical processes in the conduction bands of infrared-coupled quantum wells. *Phys. Rev. B*, 59(23):15388, 1999.
- [43] S.H. Autler and C.H. Townes. Stark effect in rapidly varying fields. *Phys. Rev.*, 100(2):703, October 1955.
- [44] B. R. Mollow. Power spectrum of light scattered by two-level systems. *Phys. Rev.*, 188(5):1969, December 1969.
- [45] S. Alam. *Lasers without Inversion and Electromagnetically Induced Transparency*. SPIE, 1999.

- [46] J.H. Eberly. Transmission of dressed fields in three-level media. *Quant. Semiclass. Optics*, 7:373, 1995.
- [47] M.O. Scully and M.S. Zubairy. *Quantum Optics*. Cambridge University Press, 1997.
- [48] D.J. Fulton, S. Shepherd, R.R. Moseley, B.D. Sinclair, and M.H. Dunn. Continuous-wave electromagnetically induced transparency: A comparison of V, λ and cascade systems. *Phys. Rev. A*, 52:2302, 1995.
- [49] A. Van Der Ziel. *Solid state physical electronics*. Prentics-Hall, Inc., 1957.
- [50] H.U. Borgstedt. *Applied chemistry of the alkali metals*. Plenum Press, 1987.
- [51] F. Schuda. *High resolution spectroscopy using a CW stabilized dye laser*. PhD thesis, University of Rochester, New York, 1974.
- [52] D.A. Steck. Sodium D line data. Unpublished. <http://steck.us/alkalidata/>.
- [53] A. Corney. *Atomic and laser spectroscopy*. Oxford University Press, 1977.
- [54] E.B. Alexandrov, M.P. Chaika, and G.I.Khvostenko. *Interference of atomic states*. Springer-Verlag, Berlin, 1993.
- [55] R.S. Bennink. *Frequency conversion of optical signals using coherently prepared media*. PhD thesis, University of Rochester, The Institute of Optics, Rochester, NY14627, 2004.
- [56] C. Cohen-Tannoudji, B. Du, and F. Laloë. *Quantum mechanics*, volume II. Wiley, New York, 1977.
- [57] C. Doppler. *Abh. Königl, böhm. Geselsch*, 2:466, 1842.
- [58] W. Happer. Optical pumping. *Rev. Mod. Phys.*, 44(2):169, April 1972.
- [59] M. Sargent III. Spectroscopic techniques based on Lamb's laser theory. *Phys. Rep.*, 43:223, 1978.
- [60] W. E. Lamb, Jr. Theory of an optical maser. *Phys. Rev. A*, 134:A1430, 1964.

- [61] W.R. Bennett, Jr. Hole burning effects in a He-Ne optical maser. *Phys. Rev.*, 126(2):580, April 1962.
- [62] H.R. Schlossberg and A. Javan. Saturation behavior of a Doppler-broadened transition involving levels with closely-spaced structure. *Phys. Rev.*, 150:267, 1966.
- [63] S. Mandel and P.N. Ghosh. Line shape and frequency shift of lamb dip and crossover-resonance dip in closely spaced transitions. *Phys. Rev. A*, 45:4990, 1992.
- [64] M.S. Feld and A. Javan. Laser-induced line-narrowing effects in coupled doppler-broadened transitions. *Phys. Rev.*, 177:540, 1969.
- [65] M.D. Levenson. *Introduction to Nonlinear Laser Spectroscopy*. Academic, New York, 1982.
- [66] J. Shirley, R.J. Hall, and A.C. Eckbreth. Folded BOXCARS for rotational Raman studies. *Opt. Lett.*, 5(9):380, September 1980.
- [67] D.G. Steel and J.T. Remillard. Resonant nearly degenerate backward four-wave mixing in open and closed systems. *Phys. Rev. A*, 36(9):4330, November 1987.
- [68] E.J. Woodbury and W.K. Ng. *Proc. I.R.E.*, 50:2367, 1962.
- [69] P.D. Maker and R.W. Terhune. Study of optical effects due to an induced polarization third order in the electric field strength. *Phys. Rev.*, 137(3A):A801, February 1965.
- [70] J.W. Nibler and G.V. Knighten. Coherent anti-Stokes Raman spectroscopy. In A. Weber, editor, *Raman Spectroscopy of Gases and Liquids*, volume 11 of *Topics in Current Physics*, chapter 7, page 253. Springer-Verlag, Berlin, 1978.
- [71] N. Bloembergen. *Am. J. Phys.*, 35:989, 1967.
- [72] Y.R. Shen. In M. Cardona, editor, *Light Scattering in Solids*, volume 8 of *Topics in Appl. Physics*, page 275. Springer-Verlag, Berlin, 1975.
- [73] M.D. Levenson and J.J. Song. Coherent Raman spectroscopy. In M.S. Feld and V.S. Letokhov, editors, *Coherent Nonlinear Optics*, volume 21 of *Topics in Current Physics*, page 293. Springer-Verlag, Berlin, 1980.

- [74] D.L. Rousseau, J.M. Friedman, and P.F. Williams. Coherent anti-stokes Raman spectroscopy. In A. Weber, editor, *Raman Spectroscopy of Gases and Liquids*, volume 11 of *Topics in Current Physics*, chapter 6, page 203. Springer-Verlag, Berlin, 1978.
- [75] R.W. Boyd. *Nonlinear Optics*. Academic, New York, 1992.
- [76] J.S. Aitchison, Y. Silberberg, A.M. Weiner, d.E. Leaird, M.K. Oliver, J.L. Jackel, E.M. Vogel, and P.W.E. Smith. Spatial optical solitons in planar glass waveguides. *JOSA B*, 8(6):1290, June 1991.
- [77] V.I. Bespalov and V.I. Talanov. Filamentary structure of light beams in nonlinear liquids. *JETP Lett.*, 3:307, 1966.
- [78] R.S. Bennink, V. Wong, A.M. Marino, D.L. Aronstein, R.W. Boyd, C.R. Stroud, Jr., S. Lukishova, and D.J. Gauthier. Honeycomb pattern formation by laser-beam filamentation in atomic sodium vapor. *Phys. Rev. Lett.*, 88(11):113901, March 2002.
- [79] G.P. Agrawal. *Nonlinear fiber optics*. Academic, New York, second edition, 1989.
- [80] L.G. Joneckis and J.H. Shapiro. Quantum propagation in a Kerr medium: Lossless, dispersionless fiber. *JOSA B*, 10(6):1102, June 1993.
- [81] M.S. Bigelow, N.N. Lepeshkin, and R.W. Boyd. Observation of ultraslow light propagation in a ruby crystal at room temperature. *Phys. Rev. Lett.*, 90(11):113903, March 2003.
- [82] R.S. Bennink, R.W. Boyd, C.R. Stroud, Jr., and V. Wong. Enhanced self-action effects by electromagnetically induced transparency in the two-level atom. *Phys. Rev. A*, 63:033804, 2001.
- [83] A.D. Wilson-Gordon and H. Friedmann. Enhanced index of refraction: a comparison between two- and three-level systems. *Optics Commun.*, 94(4):238, November 1992.
- [84] V. Wong, R.W. Boyd, C.R. Stroud, Jr., R.S. Bennink, and A. Marino. Multiple Resonances in the Sodium D1 Line. *Phys. Rev. A*, 68:012502, July 2003.

- [85] V. Wong, R.S. Bennink, A. Marino, R.W. Boyd, C.R. Stroud, Jr., and F.A. Narducci. Influence of coherent Raman scattering on coherent population trapping in atomic sodium vapor. *Phys. Rev. A*, 2004. Accepted.
- [86] R.S. Bennink, V. Wong, A.M. Marino, R.W. Boyd, and C.R. Stroud, Jr. Frequency conversion of optical signals using coherently prepared media. 2004. To be submitted.
- [87] R.B. Miles and S.E. Harris. Optical third-harmonic generation in alkali metal vapors. *IEEE J. Quant. Elect.*, 9(4):470, April 1973.
- [88] P.R. Hemmer. *Precision studies of stimulated resonance Raman scattering in atomic beams*. PhD thesis, Massachusetts Institute of Technology, Massachusetts, 1984.
- [89] I.E. Mazets, B.G. Matisov, E. Cerboneschi, and E. Arimondo. Normal modes for electromagnetically induced transparency in the presence of off-resonance transitions. *Phys. Lett. A*, 229:77, 1997.
- [90] H. Xia, S.J. Sharpe, A.J. Merriam, and S.E. Harris. Electromagnetically induced transparency in atoms with hyperfine structure. *Phys. Rev. A*, 56(5):R3362, 1997.
- [91] F. Renzoni, W. Maichen, L. Windholz, and E. Arimondo. Coherent population trapping with losses observed on the Hanle effect of the D1 sodium line. *Phys. Rev. A*, 55(5):3710, May 1997.
- [92] D. Budker, D.J. Orlando, and V. Yashchuk. Nonlinear laser spectroscopy and magneto-optics. *Am. J. Phys.*, 67(7):584, July 1999.
- [93] K. Motomura and M. Mitsunaga. High-resolution spectroscopy of hyperfine Zeeman components of the sodium D1 line by coherent population trapping. *J. Opt. Soc. Am. B*, 19(10):2456, October 2002.
- [94] A. Lezama, S. Barreiro, A. Lipsich, and A.M. Akulshin. Coherent two-field spectroscopy of degenerate two-level systems. *Phys. Rev. A*, 61:013801, December 1999.
- [95] L. Allen and J.H. Eberly. *Optical Resonance and Two-Level Atoms*. Wiley, New York, 1975.

- [96] L. Gallmann, D.H. Sutter, N. Matuscheck, G. Steinmeyer, U. Keller, C. Iaconis, and I.A. Walmsley. Characterization of sub-6-fs optical pulses with spectral phase interferometry for direct electric-field reconstruction. *Opt. Lett.*, 24(18):1314, September 1999.
- [97] T.M. Shuman, M.E. Anderson, J. Bromage, C. Iaconis, L. Waxer, and I.A. Walmsley. Real-time SPIDER: ultrashort pulse characterization at 20 Hz. *Opt. Express*, 5(6):134, September 1999.
- [98] D.F. Nelson, R.C. Miller, and D.A. Kleinman. Band nonparabolicity effects in semiconductor quantum wells. *Phys. Rev. B*, 35(14):7770, May 1987.
- [99] T. Mozume, H. Yoshida, A. Neogi, and M. Kudo. Near-infrared intersubband absorption in InGaAs/AlAsSb grown by molecular beam epitaxy. *J. Cryst. Growth*, 201/202:1077, 1999.
- [100] R.Q. Yang and J.M. Xu. Selection rules of intersubband transitions in conduction-band quantum wells. *Phys. Rev. B*, 50(11):7474, September 1994.
- [101] R. Ferreira and G. Bastard. Evaluation of some scattering times for electrons in unbiased and biased single- and multiple-quantum-well structures. *Phys. Rev. B*, 40(2):1074, July 1989.
- [102] K.L. Campman, H. Schmidt, A. Imamoğlu, and A.C. Gossard. Interface roughness and alloy-disorder scattering contributions to intersubband transition linewidths. *Appl. Phys. Lett.*, 69(17):2554, October 1996.
- [103] H. Haug and S.W. Koch. *Quantum theory of the optical and electronic properties of semiconductors*. World Scientific Publishing Co. Pte. Ltd., 3rd edition, 2001.
- [104] J.H. Smet, C.G. Fonstad, and Q. Hu. Intrawell and interwell intersubband transitions in multiple quantum wells for far-infrared sources. *J. Appl. Phys.*, 79(12):9305, June 1996.
- [105] H. Sakaki, T. Noda, K. Hirakawa, M. Tanaka, and T. Matsusue. Interface roughness scattering in GaAs/AlAs quantum wells. *Appl. Phys. Lett.*, 51(23):1934, December 1987.
- [106] G. Weber. The effect of electric field on intrasubband and intersubband transitions via interface phonons in GaAs-AlAs quantum wells. *J. Phys. C*, 4:9831, 1992.

- [107] H. Schmidt and A. Imamoğlu. Nonlinear optical devices based on a transparency in semiconductor intersubband transitions. *Optics Commun.*, 131:333, November 1996.
- [108] H. Schmidt and R.J. Ram. All-optical wavelength converter and switch based on electromagnetically induced transparency. *Appl. Phys. Lett.*, 76(22):3173, May 2000.
- [109] V. Wong, A. Schweinsberg, R.W. Boyd, and G.W. Wicks. Coherent population trapping in an Island well. *LS XIX Tech. Digest*, page 99, 2003.
- [110] A. Neogi, T. Mozue, H. Yoshida, and O. Wada. Intersubband transitions at 1.3 and 1.55 μm in a novel coupled InGaAs-AlAsSb double-quantum-well structure. *IEEE Photon. Tech. Lett.*, 11(6):632, June 1999.
- [111] H. Yoshida, T. Mozume, A Neogi, and O. Wada. Ultrafast all-optical switching at 1.3 μm /1.55 μm using novel InGaAs/AlAsSb/InP coupled double quantum well structure for intersubband transitions. *Elect. Lett.*, 35(13):1102, June 1999.
- [112] A.V. Gopal, H. Yoshida, T. Simoyama, N. Georgiev, T. Mozume, and H. Ishikawa. Well-width and doping-density dependence of 1.35 μm intersubband transition in InGaAs/AlAsSb quantum wells. *Appl. Phys. Lett.*, 80(25):4696, June 2002.
- [113] Y.P. Varshni. Temperature dependence of the energy gap in semiconductors. *Physica*, 34(1):149, 1967.
- [114] I. Vurgaftman, J.R. Meyer, and L.R. Ram-Mohan. Band parameters for III-V compound semiconductors and their alloys. *J. Appl. Phys.*, 89(11):5815, June 2001.
- [115] S. Adachi. Band gaps and refractive indices of AlGaAsSb, GaInAsSb, and InPAsSb: Key properties for a variety of the 2-4 μm optoelectronic device applications. *J. Appl. Phys.*, 61(10):4869, January 1987.
- [116] S. Papadementriou, S. Chakmakjian, and C. R. Stroud, Jr. Optical subharmonic Rabi resonances. *J. Opt. Soc. Am. B*, 9(7):1182, July 1992.

Appendix

A General Density Matrix Equations of Motion

The response of the probe field is calculated from the general form of the density matrix equations of motion:

$$\dot{\tilde{\rho}}_{nn} = -\frac{i}{\hbar} \sum_{\nu} (\tilde{V}_{n\nu} \tilde{\rho}_{\nu n} - \tilde{\rho}_{n\nu} \tilde{V}_{\nu n}) + \sum_{l>n} \gamma_{nl} \tilde{\rho}_{ll} - \sum_{l<n} \gamma_{ln} \tilde{\rho}_{nn}, \quad (\text{A.1})$$

$$\begin{aligned} \dot{\tilde{\rho}}_{nm} = & -\frac{i}{\hbar} \sum_{\nu} (H_{0,n\nu} \tilde{\rho}_{\nu m} - \tilde{\rho}_{n\nu} H_{0,\nu m}) - \frac{i}{\hbar} \sum_{\nu} (\tilde{V}_{n\nu} \tilde{\rho}_{\nu m} - \tilde{\rho}_{n\nu} \tilde{V}_{\nu m}) \\ & - \Gamma_{nm} \tilde{\rho}_{nm}, \end{aligned} \quad (\text{A.2})$$

where the dephasing rate is defined as

$$\Gamma_{nm} = \frac{1}{2} \left(\sum_{l<n} \gamma_{ln} + \sum_{l<m} \gamma_{lm} \right) + \Gamma_{nm}^{\text{coll}}, \quad (\text{A.3})$$

and $\Gamma_{nm}^{\text{coll}}$ is the dephasing rate due to elastic collision. The H_0 's are the diagonal elements of the unperturbed Hamiltonian, the V 's are the off-diagonal elements of the interaction Hamiltonian, and the γ_{nl} 's are the phenomenologically-introduced decay rates from level $|l\rangle$ to level $|n\rangle$. ρ_{nn} represents the population amplitude of level $|n\rangle$ and ρ_{nm} represents the coherence between levels $|n\rangle$ and $|m\rangle$.

A rotating frame transformation is performed for the off-diagonal density matrix elements by separating the rapidly oscillating terms of the density matrix elements and applied fields:

$$\rho_{nm} = \sigma_{nm} e^{-i\omega_j t}, \quad (\text{A.4})$$

$$\mathcal{E} = E_0 e^{-i\omega_j t}, \quad (\text{A.5})$$

where ω_j is the frequency of the applied field on the $|m\rangle \rightarrow |n\rangle$ transition. The rotating wave approximation is then applied by keeping only the slowly varying terms (dropping all terms that oscillate at $2\omega_j$). These transformation and approximation are used to isolate the solution to the frequency of interest (usually much lower than the optical frequency). The rule of population conservation

$$\sum \sigma_{nn} = 1, \quad (\text{A.6})$$

is applied to eliminate one of the excited levels from the equations. The equations for various systems are written out explicitly in Appendix D. They can however be written more compactly in matrix form:

$$\dot{R} + S = BR, \quad (\text{A.7})$$

where R is a column vector of the density matrix elements, \dot{R} is the first order time derivative of R , B is the matrix that consists of the Hamiltonian and relaxation terms, and the vector S is the driving term of the differential equation. The driving term results from the incorporation of the conservation of probability. R can then be solved to all orders of the field strength or perturbatively. If there is a bichromatic field on any of the transitions, a Floquet expansion is required to solve the equations.

B Floquet Expansion

When two fields of dissimilar frequencies are applied to a single optical transition, the equations of motion can be solved with a Floquet harmonic (Fourier) expansion. The bichromatic field is defined as

$$\tilde{\mathcal{E}} = E_p e^{-i\omega_p t} + E_s e^{-i\omega_s t} + \text{c.c.}, \quad (\text{B.1})$$

and the Rabi frequency can be defined as

$$\tilde{\Omega} = \left(\Omega_p + \Omega_s e^{-i\zeta t} \right) e^{-i\omega_p t}, \quad (\text{B.2})$$

where Ω_p (Ω_s) is the Rabi frequency of the pump (probe) field E_p (E_s), and ζ is the pump-probe detuning ($\zeta = \omega_s - \omega_p$). The vector S and matrix B in Eq. A.7 are each partitioned into terms with different time dependence

$$S = \Omega_s^* S_{-1} e^{i\zeta t} + S_0 + \Omega_s S_1 e^{-i\zeta t}, \quad (\text{B.3})$$

$$B = \Omega_s^* B_{-1} e^{i\zeta t} + B_0 + \Omega_s B_1 e^{-i\zeta t}. \quad (\text{B.4})$$

Substituting these definitions into Eq. A.7, the matrix form of the equations of motion becomes

$$\dot{R} + \Omega_s^* S_{-1} e^{i\zeta t} + S_0 + \Omega_s S_1 e^{-i\zeta t} = (\Omega_s^* B_{-1} e^{i\zeta t} + B_0 + \Omega_s B_1 e^{-i\zeta t}) R. \quad (\text{B.5})$$

A simple application of Floquet's theorem shows that the steady-state ($\dot{R} = 0$) solution R to Eq. B.5 will have only terms at the harmonics of the detuning ζ . The perturbative (in field strength)

approach is performed by assuming that E_s is weak enough so that the Floquet harmonic expansion can be truncated at the third order:

$$\begin{aligned}
R &= R_0 + \Omega_s^* R_{-1} e^{i\zeta t} + \Omega_s R_1 e^{-i\zeta t} \\
&+ (\Omega_s^*)^2 R_{-2} e^{2i\zeta t} + |\Omega_s|^2 H_0 + (\Omega_s)^2 R_2 e^{-2i\zeta t} \\
&+ (\Omega_s^*)^3 R_{-3} e^{3i\zeta t} + \Omega_s^* |\Omega_s|^2 H_{-1} e^{i\zeta t} + \Omega_s |\Omega_s|^2 H_1 e^{-i\zeta t} + (\Omega_s)^3 R_3 e^{-3i\zeta t}. \quad (\text{B.6})
\end{aligned}$$

The coefficients are obtained by substituting Eq. B.6 into Eq. B.5 and equating the coefficients of the different harmonics of ζ and corresponding powers of Ω_s . The resulting equations are:

- Zeroth Floquet order terms:

With Ω_s^0 , setting $\dot{R}_0 = 0$:

$$\begin{aligned}
S_0 &= B_0 R_0, \\
R_0 &= B_0^{-1} S_0. \quad (\text{B.7})
\end{aligned}$$

- First Floquet order terms:

With Ω_s :

$$\begin{aligned}
-i\zeta R_1 + S_1 &= B_0 R_1 + B_1 R_0, \\
R_1 &= (B_0 + i\zeta)^{-1} (S_1 - B_1 R_0), \quad (\text{B.8})
\end{aligned}$$

and with Ω_s^* :

$$\begin{aligned}
i\zeta R_{-1} + S_{-1} &= B_0 R_{-1} + B_{-1} R_0, \\
R_{-1} &= (B_0 - i\zeta)^{-1} (S_{-1} - B_{-1} R_0). \quad (\text{B.9})
\end{aligned}$$

- Second Floquet order terms:

With $(\Omega_s)^2$:

$$\begin{aligned}
-2i\zeta R_2 &= B_0 R_2 + B_1 R_1, \\
R_2 &= -(B_0 + 2i\zeta)^{-1} B_1 R_1, \quad (\text{B.10})
\end{aligned}$$

with $(\Omega_s^*)^2$:

$$\begin{aligned} 2i\zeta R_{-2} &= B_0 R_{-2} + B_{-1} R_{-1}, \\ R_{-2} &= -(B_0 - 2i\zeta)^{-1} B_{-1} R_{-1}, \end{aligned} \quad (\text{B.11})$$

and with $|\Omega_s|^2$:

$$\begin{aligned} 0 &= B_0 H_0 + B_1 R_{-1} + B_{-1} R_1, \\ H_0 &= -B_0^{-1} (B_1 R_{-1} + B_{-1} R_1). \end{aligned} \quad (\text{B.12})$$

- Third Floquet order terms:

With $(\Omega_s)^3$:

$$\begin{aligned} -3i\zeta R_3 &= B_0 R_3 + B_1 R_2, \\ R_3 &= -(B_0 + 3i\zeta)^{-1} B_1 R_2, \end{aligned} \quad (\text{B.13})$$

with $(\Omega_s^*)^3$:

$$\begin{aligned} 3i\zeta R_{-3} &= B_0 R_{-3} + B_{-1} R_{-2}, \\ R_{-3} &= -(B_0 - 3i\zeta)^{-1} B_{-1} R_{-2}, \end{aligned} \quad (\text{B.14})$$

with $\Omega_s |\Omega_s|^2$:

$$\begin{aligned} -i\zeta H_1 &= B_0 H_1 + B_1 H_0 + B_{-1} R_2, \\ H_1 &= -(B_0 + i\zeta)^{-1} (B_1 H_0 + B_{-1} R_2), \end{aligned} \quad (\text{B.15})$$

and with $\Omega_s^* |\Omega_s|^2$:

$$\begin{aligned} i\zeta H_{-1} &= B_0 H_{-1} + B_{-1} H_0 + B_1 R_{-2}, \\ H_{-1} &= -(B_0 - i\zeta)^{-1} (B_1 R_{-2} + B_{-1} H_0). \end{aligned} \quad (\text{B.16})$$

The density matrix element $\sigma^{(1)}$ corresponding to the linear susceptibility of the probe field can be obtained from the R_1 vector, while the nonlinear susceptibility (for self-phase modulation) which

is proportional to $\sigma^{(3)}$ is obtained from the H_1 vector. The full¹ susceptibility of the pump field and the population in the levels, $\sigma^{(0)}$'s, can be obtained from the R_0 vector. Using

$$\tilde{P}(t) = \varepsilon_0[\chi^{(1)}\tilde{E}(t) + \chi^{(2)}\tilde{E}^2(t) + \chi^{(3)}\tilde{E}^3(t)], \quad (\text{B.17})$$

the susceptibilities for the probe field in MKS units are:

$$\chi^{(1)}(MKS) = \frac{N}{\varepsilon_0}\sigma^{(1)}|\mu|^2 2/\hbar, \quad (\text{B.18})$$

$$\chi^{(3)}(MKS) = \frac{N}{3\varepsilon_0}\sigma^{(3)}|\mu|^4 (2/\hbar)^3, \quad (\text{B.19})$$

where μ is the dipole moment, and N is the number density. Similarly, the full susceptibility of the pump field is

$$\chi_p(MKS) = \frac{N}{\varepsilon_0}\sigma^{(0)}|\mu|^2 2/(\hbar\Omega_p). \quad (\text{B.20})$$

These susceptibilities can be converted to gaussian units using

$$\chi^{(1)}(CGS) = \frac{1}{4\pi}\chi^{(1)}(MKS), \quad (\text{B.21})$$

$$\chi^{(3)}(CGS) = \frac{1}{1.4 \times 10^{-8}}\chi^{(3)}(MKS). \quad (\text{B.22})$$

¹To all orders of field strength.

C Continued Fraction

The equations of motion can also be solved to all orders of the field strength for all their harmonic terms as is done in [116]. However, when the driving term (S) of the differential equation (Eq. A.7) has harmonic content, a slight modification is required. Each term in the equations of motion is expanded accordingly as is done in Appendix B:

$$S = S_{-1}e^{i\zeta t} + S_0 + S_1e^{-i\zeta t}, \quad (\text{C.1})$$

$$B = B_{-1}e^{i\zeta t} + B_0 + B_1e^{-i\zeta t}, \quad (\text{C.2})$$

$$R = \dots + R_{-3}e^{i3\zeta t} + R_{-2}e^{i2\zeta t} + R_{-1}e^{i\zeta t} + R_0 + R_1e^{-i\zeta t} + R_2e^{-i2\zeta t} + R_3e^{-i3\zeta t} + \dots \quad (\text{C.3})$$

In the steady state, we can then write the recurrence relation for the harmonic terms of R as

$$B_1R_{q-1} + A_qR_q + B_{-1}R_{q+1} = S_q, \quad (\text{C.4})$$

where q is the index of the harmonic order, and $A_q = B_0 + (iq\zeta)$.

Multiplying both sides by A_q^{-1} , Eq. C.4 becomes

$$C_qR_{q-1} + R_q + G_qR_{q+1} = S_q, \quad (\text{C.5})$$

where

$$C_q = A_q^{-1}B_1, \quad (\text{C.6})$$

$$G_q = A_q^{-1}B_{-1}, \quad (\text{C.7})$$

$$b_q = A_q^{-1}S_q, \quad (\text{C.8})$$

and b_q is non-zero only for $q = 0, \pm 1$.

Solving the continued fraction of Eq. C.5, the expansion is truncated to a large index Q such that $R_Q = 0$ for $q > Q$. R_Q, R_{Q-1} and so on are then iteratively eliminated using $R_Q = -C_Q R_{Q-1}$ until the relation for $q = 2$:

$$R_2 = -(I - G_2[I - G_3\{\dots G_{Q-1}(I - G_{Q-1}C_Q)^{-1}C_{Q-1}\dots\}^{-1}C_4]^{-1}C_3)^{-1}C_2R_1, \quad (\text{C.9})$$

where I is the identity matrix. Everything to the left of R_1 in the above equation is now defined as N^+ so that

$$R_2 = N^+ R_1. \quad (\text{C.10})$$

Since b_1 is non-zero, the relation between R_1 and R_0 has an additional term (b_1),

$$R_1 = (I + G_1N^+)^{-1}b_1 - (I + G_1N^+)^{-1}C_1R_0, \quad (\text{C.11})$$

$$R_1 = -Y^+b_1 + M^+R_0, \quad (\text{C.12})$$

where Y^+ is related to M^+ by $M^+ = Y^+C_1$. In the absence of b_1 , only the second term in Eq. C.12 remains (as obtain by the iterative method to $q = 1$). Repeating the procedure for $q = -Q$, the relationship between R_{-1} and R_0 is

$$R_{-1} = -Y^-b_{-1} + M^-R_0, \quad (\text{C.13})$$

where

$$Y^- = -(I - C_{-1}[I - C_{-2}\{\dots C_{-Q+2}(I - C_{-Q+1}G_{-Q})^{-1}G_{-Q+1}\dots\}^{-1}G_{-3}]^{-1}G_{-2})^{-1}, \quad (\text{C.14})$$

and $M^- = Y^-G_{-1}$. For the $q = 0$ term, R_{-1} and R_1 are substituted into Eq. C.5 to obtain

$$\begin{aligned} R_0 &= (I + C_0M^- + G_0M^+)^{-1}C_0Y^-b_{-1} \\ &\quad + (I + C_0M^- + G_0M^+)^{-1}G_0Y^+b_1 \\ &\quad + (I + C_0M^- + G_0M^+)^{-1}b_0. \end{aligned} \quad (\text{C.15})$$

Once R_0 is obtained, R_1 and R_{-1} are calculated using Eq. C.12 and C.13 respectively. R_2 can then be calculated using Eq. C.10, and R_{-2} from the equivalent of Eq. C.10 for the negative harmonic. Positive higher order harmonics are subsequently calculated using $R_Q = -C_Q R_{Q-1}$, and the negative harmonics from $R_{-Q} = -G_{-Q} R_{-Q+1}$.

D Explicit Form of the Density Matrix Equations of Motion

D.1 Dark State - Electromagnetically Induced Transparency

The density matrix equations of motion for the dark state - electromagnetically induced transparency system shown in Fig. 4.15 after performing a rotating frame, and using the rotating wave approximation and the rule of population conservation are:

$$\dot{\sigma}_{aa} = -(\gamma_{ac} - \gamma_{ab})\sigma_{bb} - (\gamma_{ac} + \gamma_{ba})\sigma_{aa} + \frac{i}{2}\Omega_t^*\sigma_{ca} - \frac{i}{2}\Omega_t\sigma_{ac} + \gamma_{ac}, \quad (\text{D.1})$$

$$\dot{\sigma}_{bb} = -(\gamma_{bc} + \gamma_{ab})\sigma_{bb} - (\gamma_{bc} - \gamma_{ba})\sigma_{aa} + \frac{i}{2}\Omega_2^*\sigma_{cb} - \frac{i}{2}\Omega_2\sigma_{bc} + \gamma_{bc}, \quad (\text{D.2})$$

$$\dot{\sigma}_{cb} = i(\Delta_2 + i\Gamma_{cb})\sigma_{cb} + \frac{i}{2}\Omega_2\sigma_{aa} + i\Omega_2\sigma_{bb} + \frac{i}{2}\Omega_t\sigma_{ab} - \frac{i}{2}\Omega_2, \quad (\text{D.3})$$

$$\dot{\sigma}_{ca} = i(\Delta_t + i\Gamma_{ca})\sigma_{ca} + i\Omega_t\sigma_{aa} + \frac{i}{2}\Omega_t\sigma_{bb} + \frac{i}{2}\Omega_2\sigma_{ba} - \frac{i}{2}\Omega_t, \quad (\text{D.4})$$

$$\dot{\sigma}_{ba} = i(\Delta_t - \Delta_2 + i\Gamma_{ba})\sigma_{ba} - \frac{i}{2}\Omega_t\sigma_{bc} + \frac{i}{2}\Omega_2^*\sigma_{ca}, \quad (\text{D.5})$$

$$\dot{\sigma}_{bc} = -i(\Delta_2 - i\Gamma_{bc})\sigma_{bc} - \frac{i}{2}\Omega_2^*\sigma_{aa} - i\Omega_2^*\sigma_{bb} - \frac{i}{2}\Omega_t^*\sigma_{ba} + \frac{i}{2}\Omega_2^*, \quad (\text{D.6})$$

$$\dot{\sigma}_{ac} = -i(\Delta_t - i\Gamma_{ac})\sigma_{ac} - i\Omega_t^*\sigma_{aa} - \frac{i}{2}\Omega_t^*\sigma_{bb} - \frac{i}{2}\Omega_2^*\sigma_{ab} + \frac{i}{2}\Omega_t^*, \quad (\text{D.7})$$

$$\dot{\sigma}_{ab} = -i(\Delta_t - \Delta_2 - i\Gamma_{ab})\sigma_{ab} + \frac{i}{2}\Omega_t^*\sigma_{cb} - \frac{i}{2}\Omega_2\sigma_{ac}, \quad (\text{D.8})$$

where the detuning Δ and dephasing rate Γ are as defined in Section 4.4.4.

D.2 Thirteen Resonances of the Sodium D1 Line / Modulation Transfer using CPT

The density matrix equations of motion for the four-level double- Λ system as shown in Fig. 5.11 are explicitly written as:

$$\begin{aligned} \dot{\tilde{\rho}}_{dd} &= -\frac{i}{\hbar}(\tilde{V}_{da}\tilde{\rho}_{ad} - \tilde{\rho}_{da}\tilde{V}_{ad} + \tilde{V}_{db}\tilde{\rho}_{bd} - \tilde{\rho}_{db}\tilde{V}_{bd}) \\ &\quad -(\gamma_{ad} + \gamma_{bd} + \gamma_{cd})\tilde{\rho}_{dd} + \gamma_{dc}\tilde{\rho}_{cc}, \end{aligned} \quad (\text{D.9})$$

$$\begin{aligned} \dot{\tilde{\rho}}_{cc} &= -\frac{i}{\hbar}(\tilde{V}_{ca}\tilde{\rho}_{ac} - \tilde{\rho}_{ca}\tilde{V}_{ac} + \tilde{V}_{cb}\tilde{\rho}_{bc} - \tilde{\rho}_{cb}\tilde{V}_{bc}) \\ &\quad +\gamma_{cd}\tilde{\rho}_{dd} - (\gamma_{ac} + \gamma_{bc} + \gamma_{dc})\tilde{\rho}_{cc}, \end{aligned} \quad (\text{D.10})$$

$$\begin{aligned} \dot{\tilde{\rho}}_{bb} &= -\frac{i}{\hbar}(\tilde{V}_{bd}\tilde{\rho}_{db} - \tilde{\rho}_{bd}\tilde{V}_{db} + \tilde{V}_{bc}\tilde{\rho}_{cb} - \tilde{\rho}_{bc}\tilde{V}_{cb}) \\ &\quad +\gamma_{bd}\tilde{\rho}_{dd} + \gamma_{bc}\tilde{\rho}_{cc} - \gamma_{ab}\tilde{\rho}_{bb} + \gamma_{ba}\tilde{\rho}_{aa}, \end{aligned} \quad (\text{D.11})$$

$$\begin{aligned} \dot{\tilde{\rho}}_{aa} &= -\frac{i}{\hbar}(\tilde{V}_{ad}\tilde{\rho}_{da} - \tilde{\rho}_{ad}\tilde{V}_{da} + \tilde{V}_{ac}\tilde{\rho}_{ca} - \tilde{\rho}_{ac}\tilde{V}_{ca}) \\ &\quad +\gamma_{ad}\tilde{\rho}_{dd} + \gamma_{ac}\tilde{\rho}_{cc} + \gamma_{ab}\tilde{\rho}_{bb} - \gamma_{ba}\tilde{\rho}_{aa}, \end{aligned} \quad (\text{D.12})$$

$$\begin{aligned} \dot{\tilde{\rho}}_{da} &= -\frac{i}{\hbar}(H_{0,dd}\tilde{\rho}_{da} - \tilde{\rho}_{da}H_{0,aa}) - \frac{i}{\hbar}(-\tilde{\rho}_{dd}\tilde{V}_{da} - \tilde{\rho}_{dc}\tilde{V}_{ca} + \tilde{V}_{db}\tilde{\rho}_{ba} + \tilde{V}_{da}\tilde{\rho}_{aa}) \\ &\quad -\frac{1}{2}(\gamma_{ad} + \gamma_{bd} + \gamma_{cd} + \gamma_{ba})\tilde{\rho}_{da}, \end{aligned} \quad (\text{D.13})$$

$$\begin{aligned} \dot{\tilde{\rho}}_{db} &= -\frac{i}{\hbar}(H_{0,dd}\tilde{\rho}_{db} - \tilde{\rho}_{db}H_{0,bb}) - \frac{i}{\hbar}(-\tilde{\rho}_{dd}\tilde{V}_{db} - \tilde{\rho}_{dc}\tilde{V}_{cb} + \tilde{V}_{da}\tilde{\rho}_{ab} + \tilde{V}_{db}\tilde{\rho}_{bb}) \\ &\quad -\frac{1}{2}(\gamma_{ad} + \gamma_{bd} + \gamma_{cd} + \gamma_{ab})\tilde{\rho}_{db}, \end{aligned} \quad (\text{D.14})$$

$$\begin{aligned} \dot{\tilde{\rho}}_{ca} &= -\frac{i}{\hbar}(H_{0,cc}\tilde{\rho}_{ca} - \tilde{\rho}_{ca}H_{0,aa}) - \frac{i}{\hbar}(-\tilde{\rho}_{cd}\tilde{V}_{da} - \tilde{\rho}_{cc}\tilde{V}_{ca} + \tilde{V}_{ca}\tilde{\rho}_{aa} + \tilde{V}_{cb}\tilde{\rho}_{ba}) \\ &\quad -\frac{1}{2}(\gamma_{ac} + \gamma_{bc} + \gamma_{dc} + \gamma_{ba})\tilde{\rho}_{ca}, \end{aligned} \quad (\text{D.15})$$

$$\begin{aligned} \dot{\tilde{\rho}}_{cb} &= -\frac{i}{\hbar}(H_{0,cc}\tilde{\rho}_{cb} - \tilde{\rho}_{cb}H_{0,bb}) - \frac{i}{\hbar}(-\tilde{\rho}_{cd}\tilde{V}_{db} - \tilde{\rho}_{cc}\tilde{V}_{cb} + \tilde{V}_{ca}\tilde{\rho}_{ab} + \tilde{V}_{cb}\tilde{\rho}_{bb}) \\ &\quad -\frac{1}{2}(\gamma_{ac} + \gamma_{bc} + \gamma_{dc} + \gamma_{ab})\tilde{\rho}_{cb}, \end{aligned} \quad (\text{D.16})$$

$$\begin{aligned} \dot{\tilde{\rho}}_{dc} &= -\frac{i}{\hbar}(H_{0,dd}\tilde{\rho}_{dc} - \tilde{\rho}_{dc}H_{0,cc}) - \frac{i}{\hbar}(\tilde{V}_{da}\tilde{\rho}_{ac} - \tilde{\rho}_{ca}\tilde{V}_{ac} + \tilde{V}_{db}\tilde{\rho}_{bc} - \tilde{\rho}_{db}\tilde{V}_{bc}) \\ &\quad -\frac{1}{2}(\gamma_{ad} + \gamma_{bd} + \gamma_{cd} + \gamma_{ac} + \gamma_{bc} + \gamma_{dc})\tilde{\rho}_{dc}, \end{aligned} \quad (\text{D.17})$$

$$\begin{aligned} \dot{\tilde{\rho}}_{ab} &= -\frac{i}{\hbar}(H_{0,aa}\tilde{\rho}_{ab} - \tilde{\rho}_{ab}H_{0,bb}) - \frac{i}{\hbar}(\tilde{V}_{ad}\tilde{\rho}_{db} - \tilde{\rho}_{ad}\tilde{V}_{db} + \tilde{V}_{ac}\tilde{\rho}_{cb} - \tilde{\rho}_{ac}\tilde{V}_{cb}) \\ &\quad -\frac{1}{2}(\gamma_{ba} + \gamma_{ab})\tilde{\rho}_{ab}, \end{aligned} \quad (\text{D.18})$$

and $\dot{\tilde{\rho}}_{ij} = \tilde{\rho}_{ji}^*$. $H_{0,ij} = \hbar\omega_{ij}$, and \tilde{V}_{ij} is as defined in Eqs. 5.4.

These equations are also used for the transfer of modulation via CPT experiment in Section 5.5, with the energy level diagram as shown in Fig. 5.23, and the interaction Hamiltonian given by Eqs. 5.9. Note the change of fields that couple to the optical transitions.

D.3 Influence of Coherent Raman Scattering on CPT

The density matrix equations of motion for the six-wave Λ system (Fig. 5.19) used to study the effect of coherent Raman scattering on CPT, after performing only the rotating frame transformation and using the rotation wave approximation, are

$$\dot{\sigma}_{aa} = \frac{i}{2}(\Omega_1^* + \Omega_3^* e^{-i\zeta t})\sigma_{ca} - \frac{i}{2}(\Omega_1 + \Omega_3 e^{i\zeta t})\sigma_{ac} - \gamma_{ba}\sigma_{aa} + \gamma_{ab}\sigma_{bb} + \gamma_{ac}\sigma_{cc}, \quad (\text{D.19})$$

$$\dot{\sigma}_{bb} = \frac{i}{2}(\Omega_2^* + \Omega_4^* e^{i\zeta t})\sigma_{cb} - \frac{i}{2}(\Omega_2 + \Omega_4 e^{-i\zeta t})\sigma_{bc} + \gamma_{ba}\sigma_{aa} - \gamma_{ab}\sigma_{bb} + \gamma_{bc}\sigma_{cc}, \quad (\text{D.20})$$

$$\begin{aligned} \dot{\sigma}_{cc} = & -\frac{i}{2}(\Omega_1^* + \Omega_3^* e^{-i\zeta t})\sigma_{ca} + \frac{i}{2}(\Omega_1 + \Omega_3 e^{i\zeta t})\sigma_{ac} - \frac{i}{2}(\Omega_2^* + \Omega_4^* e^{i\zeta t})\sigma_{cb} \\ & + \frac{i}{2}(\Omega_2 + \Omega_4 e^{-i\zeta t})\sigma_{bc} - (\gamma_{ac} + \gamma_{bc})\sigma_{cc}, \end{aligned} \quad (\text{D.21})$$

$$\dot{\sigma}_{ba} = i(\Delta_{ba} + i\Gamma_{ba})\sigma_{ba} + \frac{i}{2}(\Omega_2^* + \Omega_4^* e^{i\zeta t})\sigma_{ca} - \frac{i}{2}(\Omega_1 + \Omega_3 e^{i\zeta t})\sigma_{bc}, \quad (\text{D.22})$$

$$\begin{aligned} \dot{\sigma}_{ca} = & i(\Delta_{ca} + i\Gamma_{ca})\sigma_{ca} + \frac{i}{2}(\Omega_1 + \Omega_3 e^{i\zeta t})\sigma_{aa} \\ & - \frac{i}{2}(\Omega_1 + \Omega_3 e^{i\zeta t})\sigma_{cc} + \frac{i}{2}(\Omega_2 + \Omega_4 e^{-i\zeta t})\sigma_{ba}, \end{aligned} \quad (\text{D.23})$$

$$\begin{aligned} \dot{\sigma}_{cb} = & i(\Delta_{cb} + i\Gamma_{cb})\sigma_{cb} + \frac{i}{2}(\Omega_2 + \Omega_4 e^{-i\zeta t})\sigma_{bb} \\ & - \frac{i}{2}(\Omega_2 + \Omega_4 e^{-i\zeta t})\sigma_{cc} + \frac{i}{2}(\Omega_1 + \Omega_3 e^{i\zeta t})\sigma_{ab}, \end{aligned} \quad (\text{D.24})$$

$$\dot{\sigma}_{ab} = -i(\Delta_{ab} - i\Gamma_{ab})\sigma_{ab} - \frac{i}{2}(\Omega_2 + \Omega_4 e^{-i\zeta t})\sigma_{ac} + \frac{i}{2}(\Omega_1^* + \Omega_3^* e^{-i\zeta t})\sigma_{cb}, \quad (\text{D.25})$$

$$\begin{aligned} \dot{\sigma}_{ac} = & -i(\Delta_{ac} - i\Gamma_{ac})\sigma_{ac} - \frac{i}{2}(\Omega_1^* + \Omega_3^* e^{-i\zeta t})\sigma_{aa} \\ & + \frac{i}{2}(\Omega_1^* + \Omega_3^* e^{-i\zeta t})\sigma_{cc} - \frac{i}{2}(\Omega_2^* + \Omega_4^* e^{i\zeta t})\sigma_{ab}, \end{aligned} \quad (\text{D.26})$$

$$\begin{aligned} \dot{\sigma}_{bc} = & -i(\Delta_{bc} + i\Gamma_{bc})\sigma_{bc} - \frac{i}{2}(\Omega_2^* + \Omega_4^* e^{i\zeta t})\sigma_{bb} \\ & + \frac{i}{2}(\Omega_2^* + \Omega_4^* e^{i\zeta t})\sigma_{cc} - \frac{i}{2}(\Omega_1^* + \Omega_3^* e^{-i\zeta t})\sigma_{ba}. \end{aligned} \quad (\text{D.27})$$

D.4 CPT in a Quantum Well System

The density matrix equations of motion for a Λ system in a quantum well system with the rotating frame and the rotating wave approximation are:

$$\dot{\sigma}_{aa} = \frac{i}{2}\Omega_a^*\sigma_{ca} - \frac{i}{2}\Omega_a\sigma_{ac} - \gamma_{ba}\sigma_{aa} + \gamma_{ab}\sigma_{bb} + \gamma_{ac}^{e-p}\sigma_{cc}, \quad (\text{D.28})$$

$$\dot{\sigma}_{bb} = \frac{i}{2}\Omega_b^*\sigma_{cb} - \frac{i}{2}\Omega_b\sigma_{bc} + \gamma_{ba}\sigma_{aa} - \gamma_{ab}\sigma_{bb} + \gamma_{bc}^{e-p}\sigma_{cc}, \quad (\text{D.29})$$

$$\dot{\sigma}_{cc} = \frac{i}{2}\Omega_a\sigma_{ac} - \frac{i}{2}\Omega_a^*\sigma_{ca} + \frac{i}{2}\Omega_b\sigma_{bc} - \frac{i}{2}\Omega_b^*\sigma_{cb} - (\gamma_{ac}^{e-p} + \gamma_{bc}^{e-p})\sigma_{cc}, \quad (\text{D.30})$$

$$\dot{\sigma}_{ba} = i(\Delta_{ba} + i\Gamma_{ba}^{ns} + i\Gamma_{ba}^{e-e} + i\Gamma_{ba}^{e-p})\sigma_{ba} - \frac{i}{2}\Omega_a\sigma_{bc} + \frac{i}{2}\Omega_b^*\sigma_{ca}, \quad (\text{D.31})$$

$$\dot{\sigma}_{ca} = i(\Delta_{ca} + i\Gamma_{ca}^{ns} + i\Gamma_{ca}^{e-e} + i\Gamma_{ca}^{e-p})\sigma_{ca} - \frac{i}{2}\Omega_a\sigma_{cc} + \frac{i}{2}\Omega_a\sigma_{aa} + \frac{i}{2}\Omega_b\sigma_{ba}, \quad (\text{D.32})$$

$$\dot{\sigma}_{cb} = i(\Delta_{cb} + i\Gamma_{cb}^{ns} + i\Gamma_{cb}^{e-e} + i\Gamma_{cb}^{e-p})\sigma_{cb} - \frac{i}{2}\Omega_b\sigma_{cc} + \frac{i}{2}\Omega_a\sigma_{ab} + \frac{i}{2}\Omega_b\sigma_{bb}, \quad (\text{D.33})$$

where

$$\Gamma_{ba}^{e-e} = \frac{1}{2}(\gamma_{aa}^{\text{in}} + \gamma_{aa}^{\text{out}} + \gamma_{bb}^{\text{in}} + \gamma_{bb}^{\text{out}}), \quad (\text{D.34a})$$

$$\Gamma_{ca}^{e-e} = \frac{1}{2}(\gamma_{aa}^{\text{in}} + \gamma_{aa}^{\text{out}}), \quad (\text{D.34b})$$

$$\Gamma_{cb}^{e-e} = \frac{1}{2}(\gamma_{bb}^{\text{in}} + \gamma_{bb}^{\text{out}}), \quad (\text{D.34c})$$

$$\Gamma_{ba}^{e-p} = \frac{1}{2}\left(\frac{\partial\rho_{aa}}{\partial t}\Big|_{\text{diff}} + \frac{\partial\rho_{bb}}{\partial t}\Big|_{\text{diff}}\right), \quad (\text{D.34d})$$

$$\Gamma_{ca}^{e-p} = \frac{1}{2}\left(\gamma_{ac}^{e-p} + \frac{\partial\rho_{aa}}{\partial t}\Big|_{\text{diff}}\right), \quad (\text{D.34e})$$

$$\Gamma_{cb}^{e-p} = \frac{1}{2}\left(\gamma_{bc}^{e-p} + \frac{\partial\rho_{bb}}{\partial t}\Big|_{\text{diff}}\right), \quad (\text{D.34f})$$

$$\Gamma_{ba}^{ns} = \frac{1}{2}(\gamma_{ba} + \gamma_{ab}), \quad (\text{D.34g})$$

$$\Gamma_{ca}^{ns} = 0, \quad (\text{D.34h})$$

$$\Gamma_{cb}^{ns} = 0, \quad (\text{D.34i})$$

$$\Delta_{ba} = \Delta_{ca} - \Delta_{cb}, \quad (\text{D.35a})$$

$$\Delta_{ca} = \omega_a - \omega_{ca}, \quad (\text{D.35b})$$

$$\Delta_{cb} = \omega_b - \omega_{cb}, \quad (\text{D.35c})$$

and $\dot{\sigma}_{ij} = \dot{\sigma}_{ji}^*$.

E Matlab Code for the Numerical Simulations

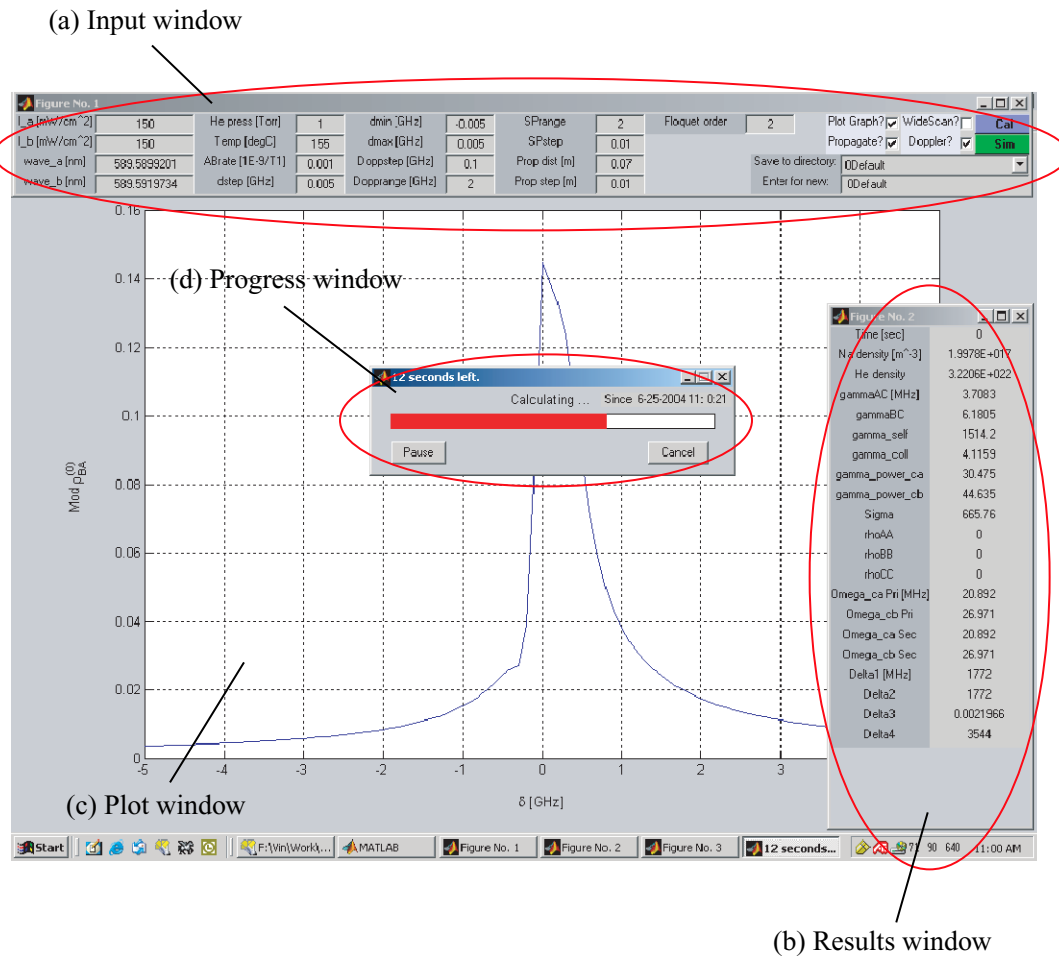


Figure E.1: Screenshot of the LP version of the Matlab code.

The density matrix equations of motion are solved numerically using Matlab version 6.1. Since the code is relatively long (as long as this thesis without the code), a flow chart is used to aid the readers in writing their own program. Each module is in its own m-file. The graphical user interface (GUI) module is a script while the rest of the m-files are functions¹. The program accepts input parameters in laboratory units as obtained from the experiments, e.g. intensity in mW/cm^2 , instead of theoretical units like the Rabi frequency.

There are two main versions of the code: the multi-system (MS) version for the DS-EIT predictions (Section 4.4.4) and the 13 resonances experiment (Section 5.3), and the propagation (LP) version using a Λ system for the CRS-CPT experiment (Section 5.4). The numerical simulation for the modulation transfer experiment is performed with a variation of the LP version: a double- Λ system with modulation sidebands as the Floquet terms. The simulation for the *Island* well structure is performed with a variation of the MS version that has options for additional dephasing processes. The flow chart describes the LP version. The MS version does not have the propagation module but includes system selection which will be described at the end of this appendix.

Fig. E.1 shows the various Matlab windows of the LP version: (a) *Input* window, (b) *Results* window, (c) *Plot* window, and (d) *Progress* window. The *Input* window is used to enter input parameters for the program. The *Results* and *Plot* windows display non-graphical and graphical results of the simulation respectively. The *Progress* window shows the computation status.

Fig. E.2 shows the flow chart describing the operations of the Matlab code used for the numerical simulations. Each module is described below:

Start The program is started by running the *GUI* m-file.

GUI The *GUI* module initializes the input boxes in the *Input* window for entering the input parameters. The *system selection* portion is only available in the MS version (see Fig. E.3). The input parameters are assigned to the variables and passed on to the *Initial Values* module.

Initial Values This module converts the input parameters in laboratory units to theoretical units used in the density matrix equations of motion.

Update Results This module updates the *Results* window.

¹Consult the Matlab help files for the difference between a script and a function.

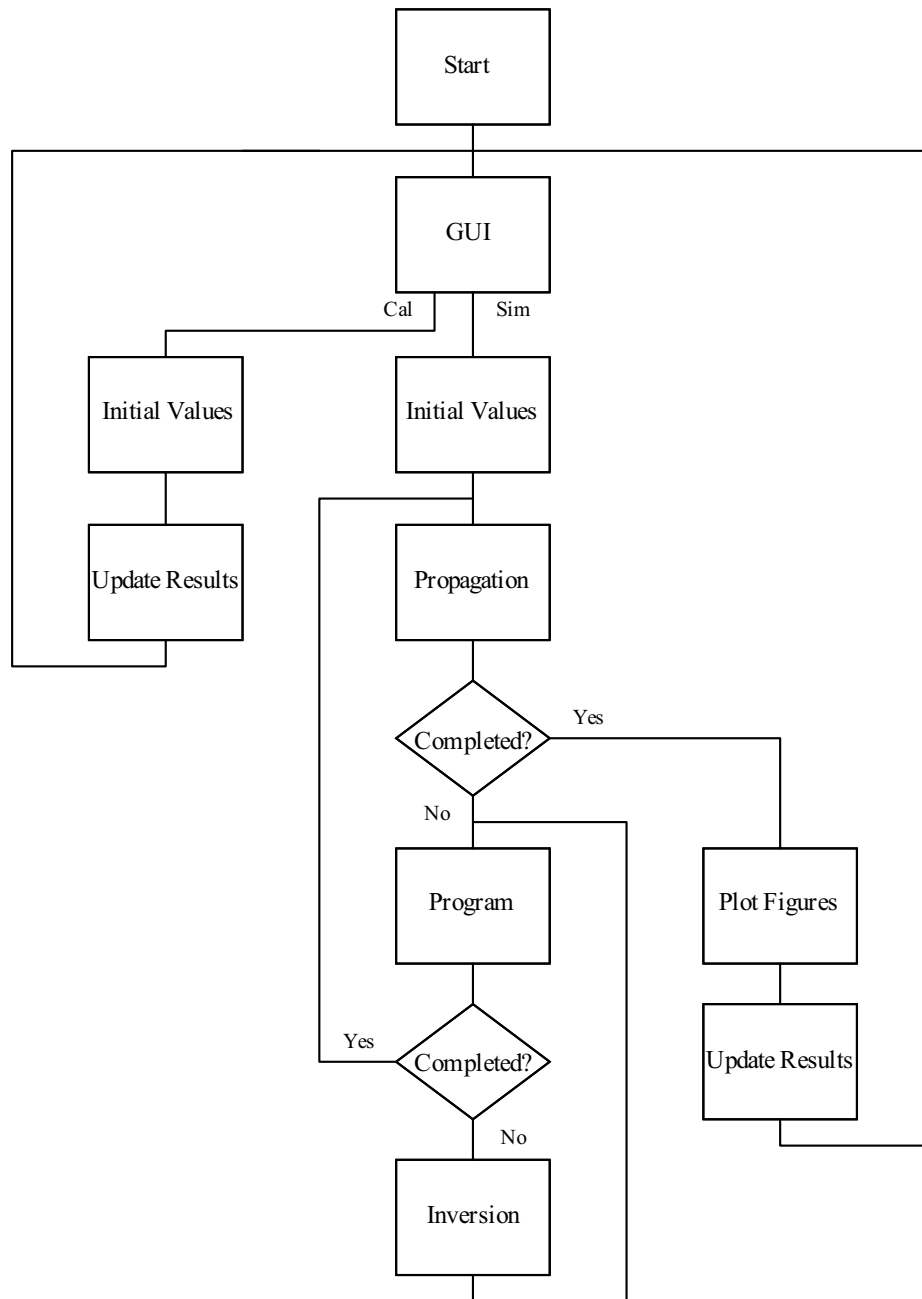


Figure E.2: Flow chart of the Matlab code for the CRS-CPT experiment.

Propagation This module consists of two m-files. The main propagation file feeds the updated electric field strength (Rabi frequency) to the ordinary differential equation (ODE) m-file. This is required as there are two atomic polarization (contributions from the pump and probe fields) that contribute at the particular pump frequency. The ODE m-file calls the *Program*

module then compute the propagation for each propagation step using the ODE45 function with the updated parameters.

Program This module houses the vectors and matrices of the density matrix equations of motion and the Doppler broadening computation routine.

Inversion This module performs the matrix inversion to compute the single atom response.

Plot Figures This module plots the desired figures.

The Doppler broadening routine shifts the field detunings by the appropriate amount and applies the corresponding weighting to the atomic response calculated with those detuning values. The Doppler broadened response of each propagation step is used in the reduced wave equation to compute the propagation at that unit propagation step. This is necessary because the field strengths at each propagation step changes with the atomic polarizations, which in turn depend on the field strengths at that point.

Fig. E.3 shows the screenshot of the MS version. Three different copies of the *Input* window is shown illustrating the various input options available. The *system selection* subroutine (in the *GUI* and *Initial Values* m-files) of the MS version comprises of a pair (pump and probe) of fields at each transition in a double- Λ system as shown earlier in Fig. 5.11. Each component of these eight fields and the decay terms between the four levels can be switch on or off by selecting the type of system required. The types of system available are: two-level, three-level V, three-level Λ , and double- Λ . The appropriate vectors and matrices are used for the equations of motion. When a three-level or two-level system is selected, matrix reduction is performed to scale the 15 by 15 matrices to 8 by 8 matrices or 3 by 3 matrices respectively, to reduce computation time.

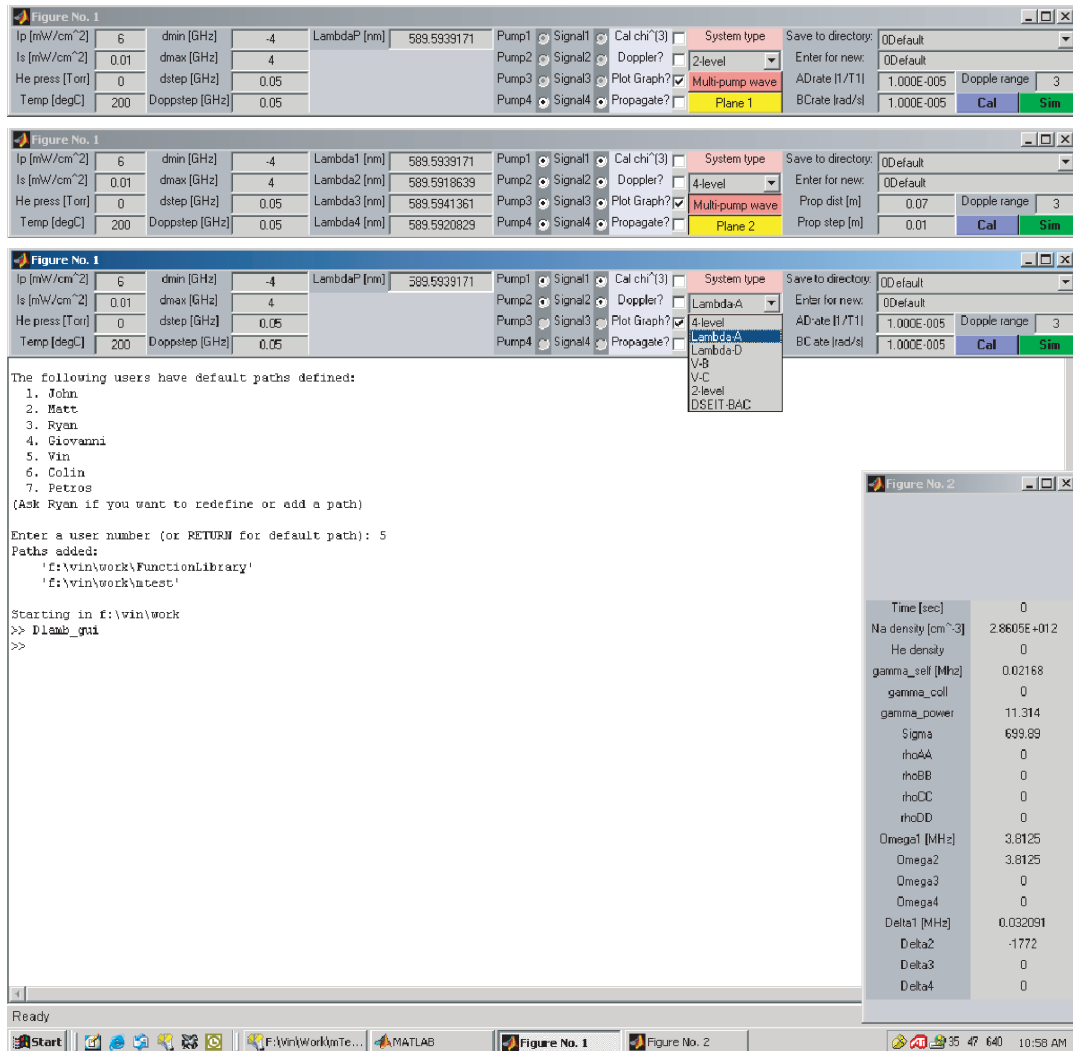


Figure E.3: Screenshot of the MS version of the Matlab code.

F FEMLAB Code for the Quantum Well Simulation

The FEMLAB code is used to calculate the dipole moments and transition wavelengths of the quantum well structures. This code is executed independently and before solving the equations of motion with the Matlab code described in the previous appendix.

The structure, mesh and equations are defined in an m-file (*structure.m* where *structure* is the name of the quantum well design studied) that FEMLAB (version 2.3) uses to compute the eigenvalues and eigenfunctions. This eigenvalue problem is described in Section 7.4.2. A different m-file is written for each structure (single well, island well, etc.) studied. FEMLAB can be invoked to run this structure m-file from a Matlab m-file.

Figure F.1 shows the flow chart describing the operations of the Matlab and FEMLAB code used for the numerical simulations of the CPT in quantum well study. The modules are described below:

Start The program is started by running the *runfem.m* Matlab file with at least the desired structure defined. Other input parameters can also be entered simultaneously or through the subsequent dialogue.

Variables from Excel file Various parameters such as the effective mass and bandgap energies are computed for the ternary and quaternary alloys (well and barrier regions) w.r.t. the composition in a Microsoft[®] Office Excel 2003 file¹. These parameters are retrieved for the desired composition.

¹The table of parameters can also be stored in or computed from an m-file

Run FEMLAB Initial execution run of FEMLAB to obtain the number of eigenvalues (confined subband energy levels). The variables are passed from `runfem.m` to `structure.m` for the computation, and the solutions are passed back.

Calculate $m(E_n)$ The energy-effective mass is calculated for each subband based on Eqs. 6.8.

$m(E_n)$ converge? The new energy dependent effective mass for subband n for both the well and barrier regions are tested for convergence. The tolerance is set at 10^{10} and the FEMLAB code is executed again until the tolerance is met or 30 runs whichever comes first.

All $m(E_n)$ converge? The energy dependent effective mass of the next subband is computed until all confined subbands are processed.

Plots The “dipole moment” or coupling strengths, and transition wavelengths between various subbands are then calculated and plotted.

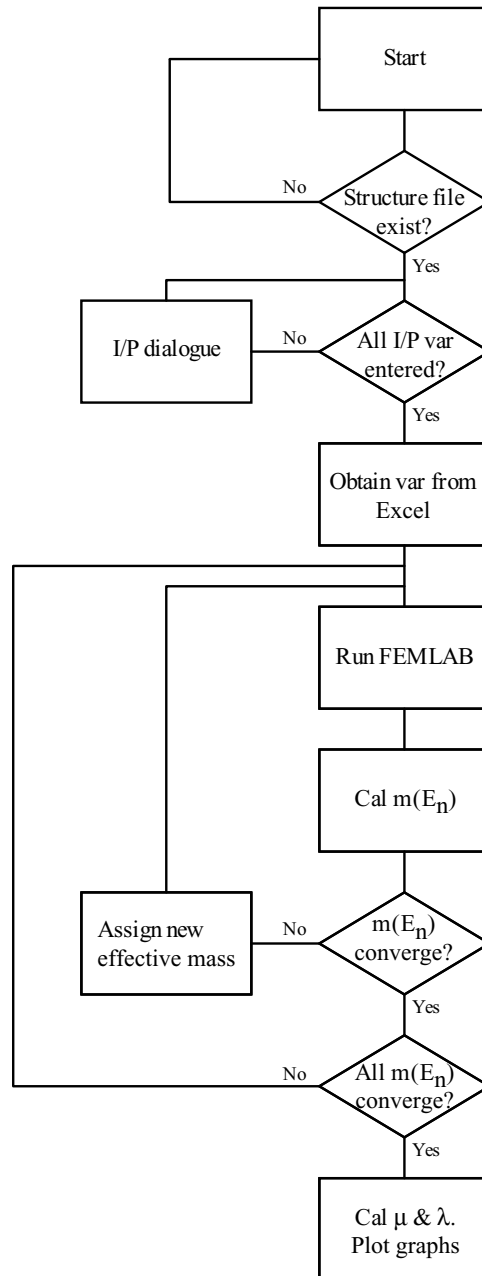


Figure F.1: Flow chart of the FEMLAB code for the CPT in quantum well simulation.

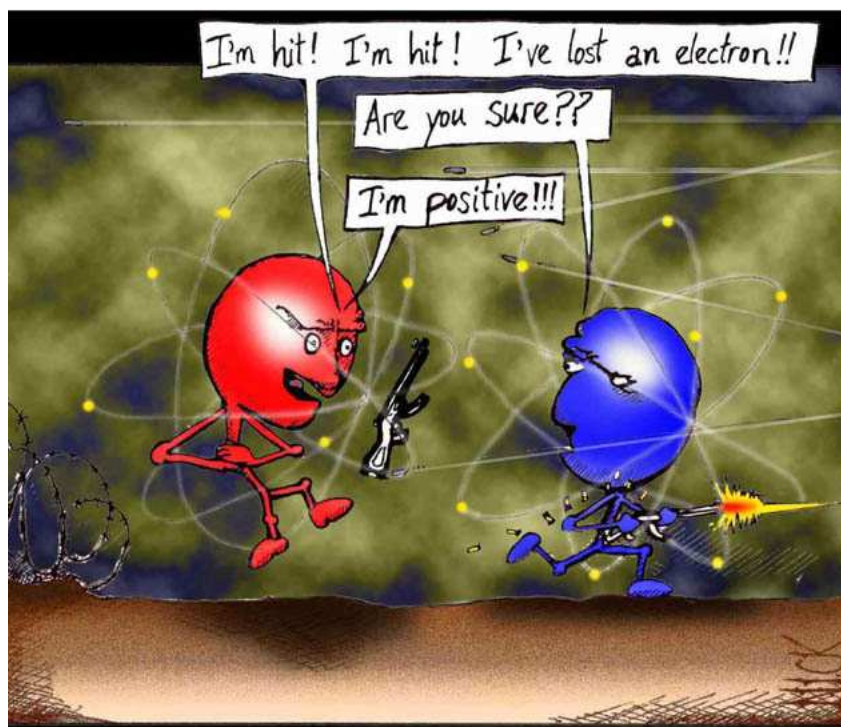
G Physical Constants

Bohr radius	a_0	$= 5.2918 \times 10^{-11} \text{ m}$
Speed of light in free space	c	$= 2.9979 \times 10^8 \text{ m/s}$
Permittivity of free space	ϵ_0	$= 8.8542 \times 10^{-12} \text{ F/m}$
Electron charge	e	$= 1.6021 \times 10^{-19} \text{ C}$ $= 1 \text{ eV}$
Reduced Planck's constant	\hbar	$= 1.055 \times 10^{-34} \text{ J-s}$
Boltzmann's constant	k_B	$= 1.381 \times 10^{-23} \text{ J/K}$
Electron rest mass	m_0	$= 9.109 \times 10^{-31} \text{ kg}$
Bohr magneton	μ_B	$= 1.165 \times 10^{-29} \text{ weber m}$
Pi	π	$= 3.1416$
Atomic mass unit	u	$= 1.6605 \times 10^{-27} \text{ kg}$
Characteristic impedance of free space	Z_0	$= 377 \text{ } \Omega$

Table G.1: Table of physical constants.

Transition wavelength	λ	$= 589.5953 \text{ nm}$
Radiative lifetime	T_1	$= 15.9 \text{ ns}$
Radiative decay rate	$\gamma/2\pi$	$= 10 \text{ MHz}$
Position matrix element	$r_{21} = \langle 3p x 3s \rangle$	$= 2.51 a_0 \text{ m}$
Atomic mass	m	$= 22.9898 \text{ u}$
Melting point	T_M	$= 97.8 \text{ }^\circ\text{C}$
Boiling point	T_B	$= 883 \text{ }^\circ\text{C}$

Table G.2: Table of constants for the $D1$ line of atomic sodium.



Another casualty in the War of the Atoms.

⁰Cartoon courtesy of <http://nearingzero.net/>